SURFACE ROUGHNESS, BAND GAP, CRYSTALLITE SIZE AND SURFACE POTENTIAL TUNING AND THEIR EFFECT ON PHOTOCATALYTIC ACTIVITY OF TITANIUM DIOXIDE THIN FILMS

BENJAMIN MBALUKA JOHN

DOCTOR OF PHILOSOPHY

(Physics)

JOMO KENYATTA UNIVERSITY

OF

AGRICULTURE AND TECHNOLOGY

2022

Surface Roughness, Band gap, Crystallite Size and Surface Potential Tuning and their Effect on Photocatalytic Activity of Titanium Dioxide Thin Films

Benjamin Mbaluka John

A Thesis Submitted in Partial Fulfillment of the Requirements for the Degree of Doctor of Philosophy in Physics of the Jomo Kenyatta University of Agriculture and Technology

2022

DECLARATION

This thesis is my original work and has not been presented for a degree in any other university.

Signature: …… Date: ……

Benjamin Mbaluka John

This thesis has been submitted for examination with our approval as the university supervisors.

Signature: …… Date: ……

Dr. Simon W. Mugo, (Ph.D)

JKUAT, Kenya

Signature: …… Date: ……

Dr. James M. Ngaruiya, (Ph.D)

JKUAT, Kenya

DEDICATION

To my dad John Mbaluka and my mum the late Annah Mbula John.

ACKNOWLEDGMENT

I would like to thank my supervisors Dr. S. W. Mugo and Dr. J. M. Ngaruiya, for giving me the opportunity to learn immensely from them. They are incredibly gifted lecturers who have taught me so much over the last couple of years. I would like to thank Jomo Kenyatta University of Agriculture and Technology (JKUAT), Dedan Kimathi University of Technology (DeKUT)-physics department, Chuka University-physics department, Karlsruhe Institute of Technology-Germany and the University of Nairobi (UON)-physics department for allowing me to use their facilities, without which, this work would not have been completed. I also thank the entire JKUAT Physics technical staff for their commitment and support towards the success of this work. Working at JKUAT Physics laboratories was one of the best learning experiences of my life. I also would like to thank Mr. Verol Nang'ani Otieno, Physics Technologist at DeKUT, Mr. Katumo Ngei at Karlsruhe Institute of Technology-Germany, Mr. Mutunga at Chuka University and Mr. Boniface Muthoka of UON for their invaluable time and support throughout my project at JKUAT. To Dr. Paul Ngumbi, Mr. John G. Mbae, Mr. Geoffrey G. Riungu, Mr. Nelson Mugambi, Miss Kipkorir J. Sheilla, Mr. Geoffrey O. Ombui and Miss Mercy Mbaja, your technical, economic and social support in my project is incredible. I would also like to thank my parents; Mr. and Mrs. John Mbaluka. You have been and still remain my strongest pillar and source of social, emotional and psychological support. I also thank my beloved children: Abigail Mbaluka, Paul Mbaluka and David Mbaluka. You give me a reason to work diligently and keep focused. Finally, I thank my beloved wife Ruth K. Mwaniki, for her love, care and support during my graduate school career. Without her, my life as a postgraduate student would have been unbearable.

TABLE OF CONTENTS

LIST OF TABLES

LIST OF FIGURES

LIST OF APPENDICES

LIST OF ABBREVIATIONS AND ACRONYMS

AM	Air Mass
CB	Conduction Band
CB	Conduction Band
CCD	Charge Coupled Device
CE	Counter Electrodes
CNTs	Carbon Nanotubes
DOS	Density of State
DSSCs	Dye-sensitized Solar Cells
DSSMs	Dye-sensitized Solar Modules
EM	Electromagnetic
FF	Fill Factor
FTO	Fluorine-doped Tin Oxide
HOMO	Highest Occupied Molecular Orbitals
I_{SC}	Short Circuit Current
ITO	Indium Tin Oxide
J_{SC}	Short-Circuit Current Density
LUMO	Lowest Unoccupied Molecular Orbitals
NIR	Near-Infrared
OSC	Organic Solar cells
P3HT	Poly (3-hexylthiophene)
PCE	Power Conversion Efficiency
PEDOT	Poly 3,4- ethylenedioxythiophene
PSS	Poly(styrenesulphonate)
PV	Photovoltaic
RMS	Root Mean Square
R_S	Series Resistance
R_{SH}	Shunt Resistance
Ru	Ruthenium

S_{EL}	Surface Energy Loss
SEM	Scanning Electron Microscopy
SKPM	Scanning Kelvin Probe Microscopy
TCOs	Transparent Conducting Oxides
TiO_2	Titanium Dioxide
UV	Ultraviolet
UV-Vis-NIR	UltraViolet-Visible-NearInfrared
VB	Valence Band
V_{CPD}	Contact Potential Difference
V_{EL}	Volume Energy Loss
V_{OC}	Open Circuit Voltage
WE	Working Electrodes
XRD	X-ray Diffraction
ZnO	Zinc Oxide

LIST OF SYMBOLS

P_m	Surface dipole moment
h	Plank's constant
A_b	Absorbance spectra
α	Absorption coefficient
ω	Angular frequency
E_g	Band gap
K_B	Boltzmann constant
θ	Bragg's angle
η_{CC}	Charge collection efficiency
N_D	Concentration of charge carriers
V_{CPD}	Contact potential difference
ε	Dielectric constant
N_A	Doping concentration
χ	Electron affinity
τ_C	Electron collection time constant
e	Electronic charge
F_ω	Electrostatic force
K_{ex}	Extinction coefficient
E_F	Fermi level
d	Film thickness
e^-	Free charge carriers
ξ	Ideality factor
ε_{im}	Imaginary dielectric constant
σ	Optical conductivity
σ_i	Imaginary optical conductivity

n_{int}	Intrinsic carrier concentration
hkl	Miller indices
ε_0	Permittivity of free space
I_L	Photocurrent
ω_p	Plasma frequency
P_o	Porosity
P_{in}	Power Input
P_{out}	Power output
ζ	Pre-exponential constant
ε_r	Real dielectric constant
σ_r	Real optical conductivity
τ_R	Recombination time constant
n	Refractive index of film
n_b	Refractive index of pore free anatase TiO_2 film
n_s	Refractive index of substrate
τ	Relaxation time
I_0	Saturation current
c	Speed of light in vacuum
γ	Transition coefficient
ϕ_t	Workfunction of gold tip
ΔG	Net change in Gibbs free energy
e'	Concentration of free charge carriers
i	Complex number
ϕ	Work function
$V_{Ö}$	Oxygen vacancies concentration
λ	Wavelength

τ_e	Electron lifetime
D_l	Diffusion length
$^{\bullet}OH$	Hydroxyl radical
$O^{\bullet}_2^-$	Superoxide radical anion

ABSTRACT

With the ever increasing demand for green energy, researchers have turned their focus on photovoltaic (PV) technology. Currently, dye-sensitized solar cells (DSSCs) have been reported as versatile and relatively less costly compared to the dominant silicon-based solar cells. In this regard, many nanostructured and nanoporous materials are now being investigated for their application in PV. Nanoporous Titanium Dioxide (TiO_2) thin films for application in DSSCs have been under intensive study for many years. The films serve as the dye-supporting electron transporting electrode in the promising DSSCs. Recent interest has been raised regarding the tuning of anatase TiO_2 films' properties by doping it with Plasmonic metals and nonmetals. This work reports on a novel method of optimizing sol-gel-derived TiO_2 thin films by their surface roughness, structural, optical, surface potential and photocatalytic activity for enhanced performance DSSCs. It also reports on the interdependence of the material's properties. The films were synthesize using Doctor-blade technique and subsequently subjected to thermal treatment. The as-deposited and annealed thin films (1-step annealing, 1 ^{o}C/Min and 2 ^{o}C/Min) were studied using various methods including Optical Microscopy, UV-Vis Spectrophotometry, Scanning Kelvin Probe Microscopy (SKPM) and X-ray diffractometry. The Optical Microscopy exhibited an increase in surface roughness with decrease in annealing rate. A remarkable correlation between annealing rate and surface roughness was established. Further analysis of the films revealed optical band gap of 3.88, 3.72, 3.33, and $3.13\ eV$ for the as-deposited, 1-Step, 2 ^{o}C/Min and 1 ^{o}C/Min annealing, respectively. The X-ray diffractometry technique revealed spectra which indicated enhancement in the films' crystallinity upon annealing of the films, with the lowest annealing rate 1 ^{o}C/Min having the largest crystallite size of $24.9633nm$. Variation in surface potential was observed and was attributed to Smoluchowski-like dipole and local dipole moment of surface atoms. Good interdependence of surface roughness, optical band gap, crystallite size, energy loss, and surface potential has been observed. The DSSCs and DSSMs fabricated from TiO_2 annealed at annealing 1 ^{o}C/Min rate exhibit the highest PCE due to high internal surface area which favour dye adsorption, and hence enhanced electron injection from the excited dye into the TiO_2. Crystallinity was also found to enhance charge transport whereas large active area of DSSCs and DSSMs enhances carrier recombination rate. This slows charge transport rate. The effect is reduced power conversion efficiency (PCE) and is believed to result from deeper density of states (DOS) in large working area films. The material's properties are tunable via annealing route and the interdependence models established are useful for rapid characterization of the thin films.

CHAPTER ONE

INTRODUCTION

1.1 Background

Solar energy is a promising alternative source of renewable energy with scientists embarking on extensive research on the most effective solar cell materials for maximum power conversion efficiency (PCE). The main solar cell technologies include silicon-based solar cells, organic solar cells (OSCs) and dye sensitized solar cells (DSSCs). According to Wan *et al.* (2011), the PCE of inorganic (Silicon-based) solar cells is about 20%. On the other hand, the best OSC based on the bulk heterojunction photoactive layer, has attained a maximum PCE of 8.0%. Ngei *et al.* (2016) reported a PCE of 3.96 % for DSCCs based on TiO_2 photoanodes and Platinum coated with graphene counter electrode has attained a maximum.

However, despite having high PCE, inorganic solar cells are disadvantageous due to their reliance on Indium Tin Oxide (ITO) which has limited transparency in the near-Infrared region (Khan, 2013). Currently, the dominant solar cell technology is highly depended on inorganic materials such as Silicon. These materials involve relatively complex lithography steps and high device fabrication costs. Furthermore, the ITO, used as a transparent electrode, limits its wide acceptance due to the scarcity of Indium. In addition, Indium diffuses into the organic semiconductor to form trapping sites for charge carriers and its sheet resistance increases with annealing (Gong, 2012; Khan, 2013). OSCs have challenges of complex chemical processing and control. For example, the chemical processing of poly (3, 4-ethylenedioxythiophene)–polystyrenesulfonic acid (PEDOT:PSS) and Poly (3-hexylthiophene)-[6,6]-phenyl-C_{61} butyric acid methyl ester (P3HT:PCBM) films has been reported as an effective methods of controlling polymer's morphology and, consequently, their optical conductivity (Sangeeth *et al.*, 2009). For example, by doping the polymers and processing them with organic solvents such as Dimethyl Sulfoxide (DMSO), their optical conductivity has been reported to vary

depending on their weight ratio of the dopants and solvent concentrations. Also, although annealing the polymers at higher temperatures enhances their optical conductivity, the polymer materials pose a challenge as they cannot withstand high temperatures (Gasiorowski *et al.*, 2013; Ouyang *et al.*, 2004).

Due to the TiO_2 semiconductor's low cost, high availability, and ease of manufacture, DSSC technology is attracting significant attention and holds promise to produce highly efficient devices (Al-Khafaji, 2013). However, to achieve reliable PCE using TiO_2 as working electrodes, there is a need to deeply elucidate on interfacial charge interaction in TiO_2 films by evaluating its surface roughness, band-gap and crystallite size, surface and volume energy losses and surface potential as the interrelation between these properties are not well reported.

Moreover, while TiO_2 is a promising photocatalysis, there is a need to optimize its surface roughness, optical, structural, and surface potential as these properties affect its performance in DSSCs. Various methods of optimizing the material's properties have been adopted, including doping with Plasmonic metals and other semiconductors (Cui et al., 2008; Kudo & Miseki, 2009). However, although doping TiO_2 with metals and non-metals has been reported to be effective methods in improving the material's photocatalytic capability, these methods are costly and complex (Dozzi & Selli, 2013). Cui et al. (2021), Muthee & Dejene (2021), and Ngei (2016) reported annealing of TiO_2 as a facile, rapid, less costly and less complex technique of modifying the material's properties.

This work aims at exploring the effect of annealing rate on TiO_2 surface roughness, the modelling of crystallite size using the films' optical band gap, surface and volume energy losses and its correlation with optical band gap, surface charge distribution through profiling of surface potential, the influence of annealing rates on the photocatalytic activity of TiO_2 films and, finally, the performance of optimized TiO_2 working electrodes on DSSCs and DSSMs.

1.2 Statement of the Problem

The growing global energy challenges have sparked the need for alternative and green energy sources. Over the years, researchers have been focusing on enhancing the PCE of DSSCs technology over silicon-based solar cells due to their reduced cost. Although DSSCs present a remarkable cost reduction, researchers have been actively working towards improving the photon harvesting efficiency of the cells. One of the methods of enhancing energy harvesting efficiency is the improvement of TiO_2 semiconductor structural designs in the dominant Platinum based DSSCs. The improvement of PCE depends on the ability to tune and optimize the TiO_2 semiconductor films' charge mobility and density of states by controlling the depth of charge trapping sites and the interaction of charges at film interface. This can be achieved through the modification of the material's surface morphology or surface roughness, optical band gap, crystallite size and surface potential. Although surface morphological, optical, microstructural properties and surface potential of TiO_2 have been widely researched, little is reported about the interdependence of these properties for rapid semiconductor characterization and the optimization of the material for PV application. This work aimed at synthesizing of TiO_2 working electrodes as an interface for FTO, its optimization, and the evaluation of its contribution towards overall performance of resulting DSSCs and DSSMs.

1.3 Justification of the Study

Currently, silicon-based inorganic solar cells technology dominate solar energy market and account for 99% of all the solar cells used globally and with practical and theoretical efficiencies of 25% and 30%, respectively (Green *et al.*, 2012). Although the inorganic solar cells offer high PCE, their manufacturing costs are relatively high compared to DSSCs. The lithography steps, high temperature and high vacuum conditions required in the manufacturing of the inorganic solar cells are also complex. In this regard, researchers are turning their attention to DSSCs, which are not only cheap to manufacture but also are simple and the properties of the materials involved in the preparation of both the working electrodes and counter electrodes are tuneable through

processing techniques. Some of the parameters which can be tuned include surface roughness, optical band gap, crystal size and surface potential via routes as annealing temperature, variation of chemical concentration (nanoparticle size), variation of pH of solvents and preparation techniques. In this work, the morphological, optical band gap, crystallite size and surface potential of TiO_2 films synthesized using Sol-gel process and thermally subjected to different annealing rates are investigated, correlated, optimized, and used to fabricate and test the performance of DSSCs and DSSMs.

1.4 Hypothesis

There is no direct relationship between annealing rate and TiO_2 films' morphological properties, optical properties, structural properties and surface potential and general photocatalytic activity of TiO_2 working electrodes in DSSCs.

1.5 Objectives

1.5.1 General Objective

To synthesis, optimize, fabricate and evaluate the performance of TiO_2-based films as working electrodes in DSSCs.

1.5.2 Specific Objectives

1. To synthesize TiO_2 films and investigate their surface morphology using optical microscopy and image processing software (*imagej*).
2. To determine the influence of annealing rate on the microstructural morphological properties of the films using XRD.
3. To determine and model the TiO_2 films' optical parameters using UV-Vis spectrophotometry and to describe the dielectric response of charge carriers and their contribution to optical conductivity.

4. To evaluate the TiO_2 films' charge distribution by profiling surface potential using SKPM.

5. To fabricate platinum-based CEs and DSSCs using optimized TiO_2 films as working electrodes and determine their I-V characteristics.

CHAPTER TWO
LITERATURE REVIEW

2.1 Solar Energy and Photovoltaic Technology

Solar energy is the radiant heat and light from the sun harnessed using various technologies such as photovoltaics, solar heating, solar thermal energy, artificial photosynthesis and molten salt power plants. The main technologies used for the harvesting of solar energy can be broadly classified into two: solar thermal energy and solar photovoltaics (Wasfi, 2011). In addition, solar energy and its technologies are broadly categorized as either active solar energy or passive solar energy depending on how they capture and convert the solar energy into solar power. Active solar photovoltaic (PV) technologies involve the use of PV systems, solar water heating and concentrated solar power. On the other hand, passive solar technology involve the orientation of a building or structure to the sun, the selection of materials with favourable light-dispensing properties or thermal mass and the design of spaces that have a natural circulation of air (Wasfi, 2011). There are different types of PV technologies and innovations, classified based on the materials used. They include: Monocrystalline silicon (Goodrich *et al.,* 2013), Polycrystalline silicon (Polverini *et al.,* 2013), Amorphous silicon (Thin-film) (Yoon *et al,* 2011), Cadmium Telluride, CdTe (thin-film) (Basol & McCandless, 2014), Copper Indium Gallium Selenide (CIGS) (Ramanujam & Singh, 2017), Polymer and organic PV (Gracia-Amillo *et al.,* 2018) and DSSCs (Carella *et al.,* 2018). Notably, the PV technologies have distinct environmental merits over conventional technologies as they are based on zero-emissions processes (Fthenakis, 2018).

Dessler (2015) reported that the intensity of solar radiation at the surface of the sun is as high as $63.3 MW/m^2$. According to Fondriest (2018), of the radiation intensity that reaches the earth's surface, infrared, visible and Ultraviolet radiations make up 49.4%, 42.3% and 8%, respectively, of the total intensity. However, owing to the earth's distance of about $149{,}597{,}890 km$ from the sun, the amount of solar radiation that

reaches the earth's surface is very low ($1.36 kW/m^2$). This is due to energy loses through space and earth's atmosphere in the form of absorption, scattering, reflection and diffusion. The spectrum of the solar radiation from the sun falls within $250-2500 nm$ spectral wavelength (Figure 2.1). According to Quaschning (2003), the spectrum is modeled by black body radiation at $5250^{o}C$.

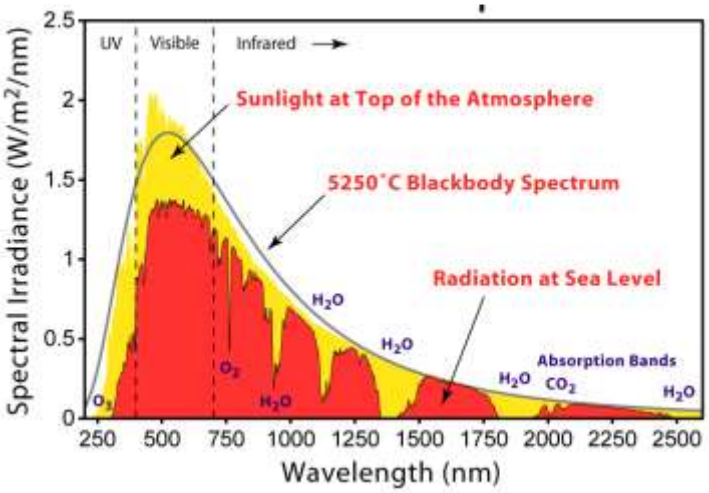

Figure 2.1: The solar spectrum indicating the spectral irradiance at the top of the atmosphere (Extraterrestrial), and spectral irradiance at the sea level (Terrestrial) spectrum of sunlight.

Solanki (2015) reported that the spectral irradiance varies throughout the day as well as with location on the earth. In this regard, a standard reference spectrum known as Air Mass (AM) has been defined for both extraterrestrial and terrestrial irradiance. Here, AM is defined as the ratio of the amount of sunlight that has to pass through the atmosphere at a given time to the amount of the sunlight that were to pass if the sun was directly overhead. The AM is taken as equal to 1 when the sun is directly overhead and is 1.5 for terrestrial applications. Air Mass zero is assumed in space. The AM 1.5 is 1 kW/m^2 and its zenith angle is 48.19^{o} (Solanki, 2015). The Solar spectrum ranges from Ultraviolet (UV) to Near-Infrared (NIR) spectral wavelengths (Figure 2.1) with energy

distribution of 2%, 47% and 51% for UV, Visible and NIR spectral ranges, respectively (Boxwell, 2012; Wolfe, 2013). Notably, there are loses which result from reflection, refraction and diffusion of solar radiation as the radiation travels through the atmosphere. It is due to these loses that the amount of solar power reaching the earth's surface is significantly reduced (Harrison *et al*., 2008).

2.1.1 Generations of Solar Cells

Solar cells are categorized into four generations based on manufacturing materials and processes, and their applications. The production of the first generation solar cells is majorly based on bulk silicon wafers which are either polycrystalline or crystalline (Avrutin *et al*., 2014). They have a typical efficiency of about 15-25% for installed modules. This type of solar cells operates under the principle of semiconductor technology (Wang *et al.,* 2014). Despite having relatively high PCE, the first generation solar cells based on pure silicon wafers, which is of limited availability. Hence, the first generation PV technology exhibit high manufacturing cost (Wang *et al.,* 2014).

The second generation consist of tandem solar cells such as copper indium diselenide and copper indium-diselenide variety (CIGS and CISX), cadmium telluride (CdTe) and microcrystalline silicon (Avrutin *et al.,* 2014). These cells exhibit reduced manufacturing cost while ensuring high PCE of 40% (Brown & Wu, 2009). Their principle of operation is akin to that of the first generation solar cells. However, the materials used in the manufacturing of these solar cells are not environmentally friendly.

The third generation PV technology employs semi-conducting organic materials which have the potential for low cost, fast and simple manufacturing process and are environmentally friendly (Jayawardena *et al.,* 2013; Brown & Wu, 2009). They include multi-junction solar cells such as DSSCs, organic polymer-based, plasmonic solar cells and tandem (Krebs, 2012). DSSCs are the most predominant devices of the third generation PV technology with a theoretical PCE of 31%. However, practically, PCEs of 15% and 20% have been achieved for organic and heterojunction based solar cells,

respectively (Ye *et al.,* 2015). Although DSSCs are known to operate under low illumination, they exhibit low performance issues as well as long term instability (Mehmood *et al.,* 2014).

The fourth generation PV technology combine the low-cost feature of the DSSCs while utilizing the stability and functionality of novel organic and inorganic nanostructures with a view to enhance the overall PCE by improving the optoelectronic properties of the materials (Jayawardena *et al.,* 2013). Currently, the prevailing fourth generation PV devices include plasmonics and quantum dots (Krebs, 2012). Notably, this generation seeks to improve charge transport within the solar cells, charge dislocation and enhancement of energy harvesting (Jayawardena *et al*., 2013). The novel materials investigated include Silicon and Silver nanowires, and carbon nanotubes (CNTs). Conibeer (2007) reported a theoretical PCE of 65%. Nevertheless, experimentally, a low PCE of 15.6% has been reported by Wang *et al.* (2014).

2.2 Dye Sensitized Solar Cells

2.2.1 Introduction

Dye sensitized solar cells (DSSCs) utilizes the advantage of substituting the environmentally unfriendly solar cells such as CdTe, CIGS and CISX (Jayawardena *et al.,* 2013; Brown and Wu, 2009). DSSCs are potential candidate for future PV power as they not only exhibit low manufacturing costs but also have relatively high PCE compared to the OSCs such as conjugated-polymer-and-fullerene derivative-based OSC with up to 5% PCE (Zhang *et al.,* 2016). DSSCs differ from the conventional solar cells in that they separate the function of the visible EM spectrum absorption from charge carrier transport (Wei, 2010). That is, in DSSCs, the dye sensitizers absorb incident light and induces vectorial electron transfer reaction. Notably, DSSCs are advantageous over Silicon-based PVs in that the former do not suffer from defects, it is easy to form semiconductor-electrolyte interface (SEI), are cost effective in production and direct energy transfer from photons to chemical energy is easily realized (Hagfeldt & Gratzel, 1995). In DSSCs, the effective electron injection into the semiconductor results from

the first layer of the adsorbed dye which consequently results to a very small current. In order to enhance electron injection process, the effective surface area of the photoanode is improved 1000-fold by utilizing nanoporous TiO_2 (Wei, 2010). DSSCs based on porous nanocrystalline TiO_2 as working electrodes with a significant PCE was first reported in 1991 by O'Regan & Gratzel (Hagfeldt & Gratzel, 2000). These findings have ever since stimulated great research interest in porous nanocrystalline semiconductor matrices permeated by dye and electrolyte solution (redox couples). According to Wurfel *et al*. (2008), nanocrystalline TiO_2 possess an interesting property in that charge transport of the photo-generated electron traversing through the material's grain boundaries and particles is highly efficient.

Ammar *et al.* (2019) reported the highest PCE of 11-12% for DSSCs using Ruthenium complex dye (N719). In this regard, researchers have indulged in various modifications of the components of the DSSCs with the aim to enhance its PCE. For example, to obtain more effective nanostructured semiconductor working electrodes, various shapes have been employed including nanorods, nanotubes, nanoparticles, nanosheets and mesoporous structure (Ammar *et al.,* 2019; Ye *et al.,* 2013; Shi *et al.,* 2013; Li *et al.,* 2013).

2.2.2 Dye Sensitized Solar Cell Terminologies

2.2.2.1 Model with a Diode

The operation of a PV module is represented using a standard model for a diode. A PV module is a set of solar cells connected in series and/or in parallel. A solar cell can be represented by equivalent circuit of a model using forward biased diode Figure 2.2 (Belarbi *et al.,* 2014).

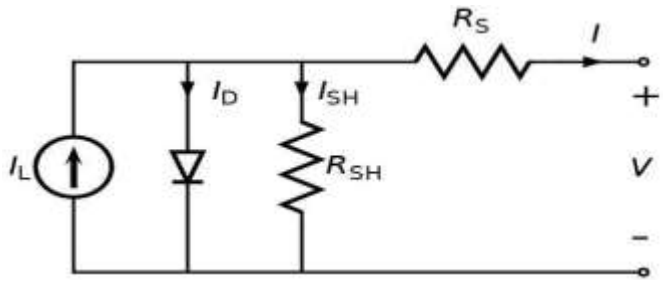

Figure 2.2: DSSC equivalent circuit (Model for a diode) showing the current path, shunt and sheet resistance.

Where I_L denotes photocurrent which is proportional to irradiance, I_D is the diode current, I_{SH} is shunt current, R_{SH} is shunt resistance and R_S is series resistance. The current I supplied by the cell is derived by applying Kirchhoff's law in Figure 2.2 as follows.

$$I_L - I_{SH} - I_D = 0 \quad \text{.....2.1}$$

$$V_d = V_{SH} = V_S + V = I_S R_S + V \quad \text{.....2.2}$$

The diode current is given by Equation 2.3.

$$I_D = I_0 \left[\exp\left(\frac{qV_D}{\xi K_B T} \right) \right] \quad \text{.....2.3}$$

Consequently, the photocurrent I supplied by the DSSC is obtained by applying Kirchhoff's law and is expressed as shown in Equation 2.4.

$$I = I_L - \frac{V - R_S I}{R_{SH}} - I_0 \left[\exp\left(\frac{e(V - R_S I}{\xi K_B T} \right) - 1 \right] \quad \text{.....2.4}$$

Where I denotes current supplied by the cell, V denotes terminal voltage of the cell, I_L is photocurrent, I_D is diode current, I_0 saturation current which is temperature

dependent, e is electronic charge, K_B is Boltzmann constant, ξ is ideality factor of the diode and T is the effective temperature (in Kelvin) of the cell (Belarbi *et al.*, 2014). The model for a diode of DSSC allows obtaining the network of cells as well as simulation of the system.

2.2.2.2 Open Circuit Voltage

Open circuit voltage (V_{OC}) is defined as the maximum voltage available from a solar cell. It occurs at zero current. That is, when a load of infinite resistance is connected to the terminals of the solar cell. V_{OC} corresponds to the amount of forward bias on the DSSC due to the bias of cell junction with the light-generated current and it may be seen as the measure of the amount of recombination in the DSSC. The Equation for V_{OC} is obtained by setting the net current to zero in the solar cell Equation 2.4 to give Equation 2.5.

$$V_{OC} = nK_BT \ln\left(\frac{I_L}{I_0} + 1\right) \quad \text{.....2.5}$$

By inspection of Equation 2.5, it may seem like V_{OC} increases linearly with temperature. However, I_0 goes up rapidly with temperature due to changes in the intrinsic carrier concentration n_{int} . For silicon solar cells, the implied V_{OC} may be determined from the carrier concentration according to Equation 2.6.

$$V_{OC} = \frac{K_BT}{e} \ln\left[\frac{(N_A + \Delta p)\Delta n}{n_{\text{int}}^2}\right] \quad \text{.....2.6}$$

Where the ratio K_BT/e represent thermal voltage, N_A denote doping concentration and Δn is the excess carrier concentration (Dissanayake *et al.*, 2022; Sinton & Cuevas, 1996). According to Vallejo *et al.* (2011), in DSSCs, V_{OC} is influenced by both the

Fermi energy level (E_F) of TiO_2 and the potential of the redox couple. In this regard, the V_{OC} corresponds to the difference in the E_F and the mobility of the electrolyte. In DSSCs, V_{OC} ranges between 0.6 - 0.8V and is given by:

$$V_{OC} = \frac{CB}{e} + \frac{k_b T}{e} \ln\left(\frac{n_c}{N_{CB}}\right) - \frac{E_{redox}}{e} \quad \text{.....2.7}$$

Where CB represents the conduction band edge of TiO_2, n_c is the number of electrons in the conduction band, N_{CB} represent the density of accessible states in the conduction band and E_{redox} is the electrolyte Fermi level. As a function of E_g , while the short-circuit current (I_{SC}) decreases with increase in E_g , the V_{OC} increases with increase in in E_g (Baruch *et al.,* 1995).

2.2.2.3 Short-Circuit Current

The I_{SC} is the current determined when the external load resistance is zero. That is, it is the maximum current from a solar cell obtained when the voltage across the terminals is zero. The I_{SC} is influenced by factors such as solar illumination/intensity or number of photons, charge transfer probability of the cell which depends mainly on the minority carrier lifetime in the base and the surface passivation and optical properties (absorption and reflection) of the electrodes (Vallejo, *et al*., 2011). Figure 2.3 shows the I-V and P-V characteristic model of PV device (Pva, 2011).

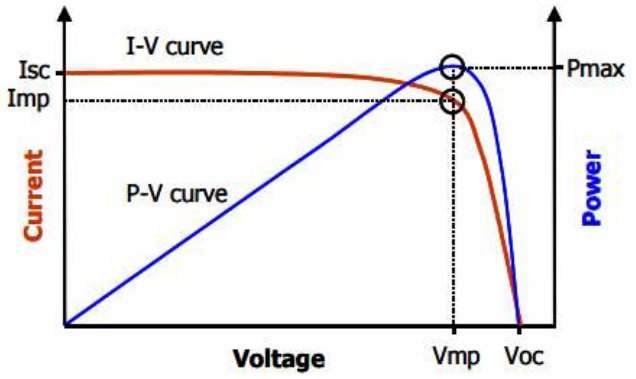

Figure 2.3: I-V and P-V curves of a PV device indicating the I_{SC}, V_{OC}, maximum current (I_{mp}) and maximum voltage (V_{mp}). The P-V curve is determined from the I-V data.

The I_{SC} is due to the electron injection efficiency from the dye to the semiconductor's conduction band. The short-circuit current density (J_{SC}) is the current per unit active area of the cell determined at zero voltage. This current arises from the generation and collection of photo-generated charge carriers and is given by:

$$J_{SC} = \frac{I_{SC}}{A}(mA/cm^2).....2.8$$

Where A denote the effective active area of the PV device. For an ideal solar cell, at moderate resistive loss mechanism, the I_{SC} equals the light-generated currents and therefore, the I_{SC} is the largest current which can be drawn from the cell.

2.2.2.4 Series and Shunt Resistances

According to Hafez *et al*., (2012), the series resistance (R_S) results from the bulk resistance of the metallic contacts, semiconductor materials, electrolyte, the contact resistance between the FTO electrode, semiconductor and the metallic contacts of the

solar cells. The R_S correlates with the Nernstian diffusion in the electrolyte, the CE and charge transfer at the FTO substrate. Thus, R_S corresponds to the sum total of the charge transfer resistance at the metal/CE/FTO interfaces (R_1), sheet resistance (R_{sheet}) of the TCO and the diffusion resistance (R_2) of the electrolyte ions. According to Yang *et al*. (2012), R_1 and R_{sheet} are constants and, therefore, the R_S of DSSCs is influenced by R_2. In the I-V characteristic curve of a DSSC, the tangent slope of vertical part near the V_{OC} is proportional to $1/R_s$, an indication that the fill factor (FF) of the DSSC increases with a decrease in R_S (Yang *et al.,* 2012).

On the other hand, the shunt resistance (R_{SH}) in DSSCs is due to the presence of impurities in the interface regions of the solar cell, the presence of crystal defects and leakage across the cell edges (Hafez *et al.,* 2012). From the I-V characteristic curve, the tangent slope of the transverse part (near I_{SC}) is proportional to the reciprocal of the R_{SH}. This indicates that FF improves when R_{SH} increases and, consequently, the PCE of the DSSC increases (Yang *et al.,* 2012).

2.2.2.5 Fill Factor

The I_{SC} and V_{OC} are the maximum current and voltage, respectively, from a solar cell. Nonetheless, at both of these operating points, the power is zero. Maximum power ($P_{\max}$) from the cell is determined at I_{mp} and V_{mp} (Figure 2.3). The fill factor (FF) is, therefore, the ratio of the maximum power output of a PV device ($P_{\max}$) to the $I_{SC} \times V_{OC}$. The FF is used to determine the maximum power produced by the solar cell or solar module. The FF is given by Equation 2.9:

$$FF = \frac{I_{mp} V_{mp}}{I_{SC} V_{OC}} \quad \text{.....2.9}$$

Fill factor indicates the "squareness" of the I-V curve and is the largest area obtained under the I-V characteristic curve.

2.2.2.6 Power Conversion Efficiency

The photocurrent efficiency or the power conversion efficiency (PCE) of a solar cell, is used to compare the photocatalytic performance of one cell to another. It is the ratio of energy output of the photovoltaic device to the input energy harvested from the sun at zenith (48.19^0). It is worth noting that at zenith, the measured irradiance is $1000W/m^2$. The PCE of the PV device is largely affected by both the temperature on the solar cell as well as the intensity of the incident EM radiation. In this regard, optimal operating conditions are necessary in order to achieve better performance of solar cells. Terrestrial solar cells are characterized at a temperature of 25^{o}C and under AM1.5. Mathematically, PCE is expressed as:

$$PCE(\%) = \frac{J_{SC} \times V_{OC} \times FF}{P_{in}} \times 100\% = \frac{P_{\max}}{P_{in}} \times 100\% \text{.....} 2.10$$

2.2.3 Structure of TiO_2 WE/Pt CE-based DSSCs

A DSSC is composed of a transparent conducting electrodes FTO (SnO2:F) or ITO, working electrodes (WE) (TiO_2, ZnO), Ruthenium dye (N719), redox couple (iodide/triiodide) and a counter electrode (Platinum).

2.2.3.1 Transparent Conducting Oxides

Transparent conducting oxides (TCOs) are thin films which act as electron collectors. For example, in the WE, TCOs function as support for the semiconducting oxide layer whereas in the CE, the TCO supports the catalyzing film, usually graphite or Platinum (Khan, 2013). Therefore, TCOs are crucial in DSSCs in that they dictate its performance as they function as electron and current collector. Therefore, TCOs must have high optical transparency to allow light to pass through without unwanted absorption and

interference. TCOs must also exhibit low electrical resistivity to facilitate electron transfer process without energy dissipation (Khan, 2013).

In order to improve the PCE of solar cells, a number of TCOs have been commonly put in place. Particularly, ITO is favoured due to its high transmittance of over 85% in the visible EM spectrum as well as a low sheet resistance of $5\Omega/cm^2$ (Sigma Aldrich, 2013; Holder, 2013). Additionally, ITO is highly regarded due to its low resistivity of about $104\Omega/cm$ at room temperature.

However, ITO has a limitation in that it is scarce and the price of Indium is high and prone to fluctuations (Holder, 2013). Due to the drawback exhibited by ITO, researchers have been prompted to seek for other TCOs as suitable electrode materials. For example, Aluminium zinc oxide (AZO) has been highly preferred as an alternative TCO. Apart from the fact that the resistivity and transparency of AZO are comparable to those of ITO, AZO is readily available and relatively cheap and thus can be widely implemented (Kim *et al.,* 2009). According to Ishibashi (1990), ITO exhibit the low resistivity due to the presence of number of free charge carriers that arise from substitution of indium atom by tin atom hence releasing an electron. Further, ITO has oxygen vacancies which act as two electron donors. However, it is worth noting that the sheet temperature of ITO increases upon annealing at temperatures above 300^{o}C. Since annealing of WEs and CEs on ITO substrates is usually above 300^{o}C, DSSCs based on ITO exhibit low PCE. According to Khan (2013), this drawback can be overcome through sputtering of a metal oxide layer such as SnO_2 and antimony doped oxide (ATO) on the ITO to form a bilayer.

Fluorine-doped tin oxide(FTO) (SnO2:F) TCOs have also found a wide application in DSSCs. FTO has been found to have high transmittance of 70-80% in the visible EM spectral range at a thickness of 750*nm*. FTO also exhibit low sheet resistance of less than $12\Omega/cm^2$, lower than that of ITO. One advantage of FTO over ITO is that its resistance remains constant even with increase in temperature unlike in ITO whose resistance increases upon annealing (Khan, 2013; Li *et al.,* 2014). Moreover, FTO glass substrate is cheaper than ITO and therefore the former is preferred over the latter.

2.2.3.2 Other Transparent Conducting Oxides

Conductive polymers have also found application as TCOs majorly due to their additional flexibility property. Some of the conductive polymers include Poly (3,4-
--ethylenedioxythiophene)- poly(styrenesulphonate) (PEDOT:PSS). The chemical structure of PEDOT:PSS used as TCO in solar cells is shown in Figure 2.4 (Singh & Nalwa, 2015).

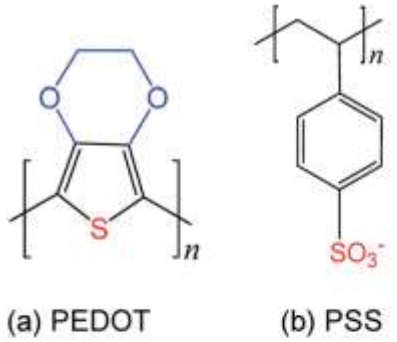

Figure 2.4: Molecular structures of organic semiconductors commonly used in Solar Cells as TCO. (a) PEDOT. (b) PSS.

The PEDOT:PSS consists of a conducting Polythiophene derivative which is electrostatically bound to a PSS Polyanion (Kirchmeyer and Reuter, 2005). Organic semiconductors such as PEDOT:PSS and Poly (3-hexylthiophene) (P3HT) have been used in PSC technology for the past decade. Organic semiconductors are comprised of hydrocarbon-based compounds that form conjugated binding pattern. These materials are characterized by alternating single and double bond between the carbon atoms making up the molecular backbone (Pingel, 2014; Clarke & Durrant, 2010).

2.2.3.3 DSSC Photoanodes

The DSSC photoanodes, also known as working electrode, is a thin film commonly TiO_2 film. The TiO_2 photoanodes are preferred over other transparent oxides such as Zinc

Oxide (ZnO), Aluminium Oxide (AL_2O_3) and Lead Oxide (PbO) due to their good electron affinity, optical transparency, nanoporous and polycrystalline nature and wide band gap of about $3.2eV$ (Kim *et al.,* 2014). In a DSSC, the photoanode is used to support the sensitizer loading (N719 dye) as well as transportation of photo-excited electrons from the excited dye's LUMO to the external circuit (Ye *et al.,* 2015). The TiO_2 is well known for its large surface area for dye loading and its fast charge transport rate (Mehmood *et al.,* 2014). TiO_2 photoanodes are processed through techniques such as doctor blading, hydrothermal techniques, dip coating, electro-spinning and spray pyrolysis.

2.2.3.4 Semiconductor Oxide Layer

The most prominent semiconductor used in DSSCs is TiO_2 film in its anatase phase. Anatase phase occurs upon crystallization of the amorphous phase at temperatures ranging between 200 ^oC and 800 ^oC (Campos *et al.,* 2012). The Phase is preferred to the other phases due to its effective area, crystallinity and wide band gap of about 3.2 eV. The wide band gap makes the anatase TiO_2 transparent to the visible EM radiation spectrum (Sayama *et al.,* 1998). Notably, the anatase phase is metastable and converts to rutile phase (band gap 3.0 eV) when heated above temperature in the range 800 – 1000 ^oC, depending on impurities and crystal size (Roberts *et al.,* 1978). Other semiconductor materials such as Zinc Oxide (ZnO) and Niobium pentoxide (Nb_2O_5) have been determined to have potential of application in DSSCs. Although DSSCs based on ZnO exhibit low PCE, ZnO exhibit similar band structure as that of TiO_2 and has high electron mobility of $1-5cm^2/Vs$ (Gong, 2012). The low PCE of the ZnO photoanodes is believed to arise from the dissolution of its surface as well as the formation of Zn^{2+}/dye aggregates in the acidic N3 dye solution (Canto-Aguilar *et al.,* 2017).

2.2.3.4.1 TiO_2 Sol-gel Deposition and Thickness Control

TiO_2 is chemically inert, biocompatible and non-toxic. It is also easy to produce in large scale due to its high surface affinity towards phosphates, carboxylates, boronates and

salicylates. TiO_2 can also be sensitized by a variety of dyes. TiO_2 mesoporous film (0D) is commonly prepared via a sol-gel method which involves hydrothermal step. The Sol-gel process involves spreading the film using a moving blade onto a stationary substrate. The film thickness depends on the surface tension and viscosity of the TiO_2 paste. It also depends on the coating speed (Chou *et al.,* 1987). The sol-gel synthesis process yields films with mesoporous morphology having nanocrystalline particles with a diameter range of 10-20 *nm* (Ngei *et al.,* 2016). According to Barbè *et al.,* (1997), the sintering process is very important as it enhances electronic conduction for light harvesting. By controlling the thickness, the effective internal surface area of the films can be significantly varied. It is worth noting that thickness control is an effective strategy for overcoming the challenge of recombination in the TiO_2 semiconductor. For example, Baglio *et al*., (2011) reported that TiO_2 nanoparticles of $15-20nm$ have effective thickness range of $8-12\mu m$. The film's porosity is affected by synthesis processes such as deposition technique, drying and sintering processes. The optimized thickness is crucial for enhanced solar cell performance and is also influenced by the pore size of the titanium oxide paste used. Ideally, the film's thickness controls photon absorption which consequently affects the current density (Kao *et al.,* 2009). It can be analyzed using step stylus profilometer (Lai *et al.,* 2011).

2.2.3.4.2 Metal Oxides as Blocking Layer for Back Reactions

The introduction of a compact layer between TiO_2 and the sensitizer or between the conductive glass and TiO_2 helps in the minimization of back recombination reaction observed in DSSCs using natural dyes as sensitizers. Burke *et al.* (2008) reported that the introduction of a compact layer increases the overall efficiency by 1-1.6%. In addition, other metal oxides such as Al_2O_3 semiconductor placed as overlayer between the TiO_2 film and the dye acts as a back reaction blocking layer. Al_2O_3 blocks the back recombination from the back contact as well as from the CB of TiO_2 (Liberatore *et al.,* 2009). Al_2O_3 functions by inducing a retardation of interfacial recombination dynamics resulting into an enhancement in the device performance.

2.2.3.4.3 Sensitization of Wide band gap Semiconductors in DSSCs

Sensitizers provide the photo-excited charge carrier at the semiconductor (Ye *et al*., 2015). They harvest EM energy to produce the photo-excited electrons at the semiconductor interface. In order to load into the semiconductor material and have desired LUMO and HOMO levels, sensitizers have chemically adsorbed group. Ye *et al*. (2015) reported that the desired LUMO and HOMO enables effective injection of electrons into the semiconductor as well as dye regeneration from the electrolyte. Additionally, sensitizers have excellent photo-stability and solubility and high molar extinction coefficient in the NIR and visible regions for light harvesting. There are five common sensitizers used for commercial production of DSSCs. They include Ruthenium (II) polypyidyl dye, quantum dot sensitizer, porphyrin dyes, metal free organic dyes and Perovskite-based sensitizer. Ru(II) polypyridyl dyes are the most commonly used as they exhibit the highest performance due to their broad-range absorption of EM radiation from UV to NIR. The Ru(II) polypyridyl dye is also known for its high molecular stability (Ye *et al*., 2015).

2.2.3.5 Inorganic Molecular Sensitizers

Dye molecules should fulfill a number of requirements to be considered a potential candidate for spectral sensitization of semiconductors. First, the dye molecules must have strong absorption across the visible spectral range characterized by large molar extinction coefficient. Secondly, it should demonstrate strong binding to the surface in that they should consist of chemical group that can attach to the semiconductor. Thirdly, its LUMO should be high enough in energy to enable efficient charge injection whereas its HOMO should be low enough in energy for efficient regeneration. Finally, the dye should have rapid electron transfer to the semiconductor, stability, low cost, reproducible synthesis and small reorganization energy for excited and ground state electron transfer in order to minimize losses. The best PCE has been achieved with polypyridyl complexes of Ru(II) bearing carboxylated ligands (Altobello *et al.,* 2004; Barbè *et al.,* 1997). These species have intense visible metal-to-ligand charge transfer

(MLCT) bands. Among the family of compounds, thiocyanate derivatives have been reported to have outstanding results. A molecular structure of N3 and N719 sensitizers is shown Figure 2.5 (Zakeeruddin *et al.*, 1998).

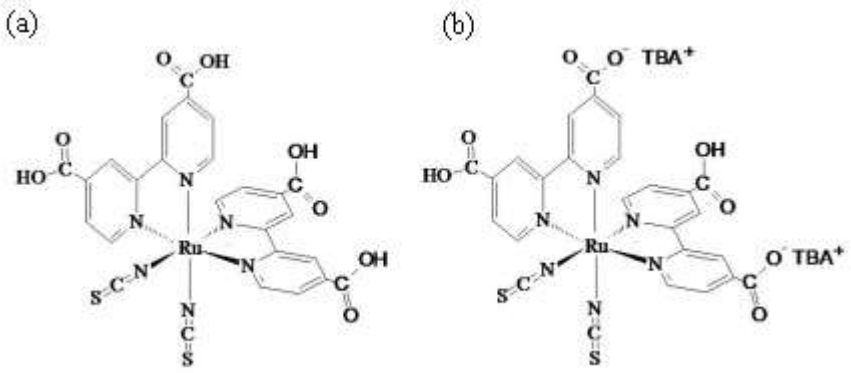

Figure 2.5: Molecular structure of inorganic sensitizers. (a) N3 and (b) N719 sensitizers.

2.2.3.6 Natural Sensitizers

In order to replace the expensive and rare Ru(II) compounds, various organic synthetic sensitizers have been extensively studied and tested as low-cost materials. They include chlorophyll derivatives, phtalocyanines, carboxylated derivatives of anthracene, porphyrins and coupled semiconductors with lower energy band gaps (Odobel *et al.*, 2003). Naturally, some flowers and fruits have various colours and have been reported to contain pigments that can be extracted and used in DSSCs as sensitizers. Unlike artificial sensitizers, the natural dyes are available, and easy to prepare. The photoactivity of natural sensitizers belongs to the anthocyanins which are water soluble flavonoids responsible for the blue and red color of many leaves and fruits. The absorption spectra of natural sensitizers exhibit favourable overlap with the solar spectrum. According to Hara *et al.* (2003), natural sensitizers have good PCE, are cheap

to test and are environmentally friendly and, therefore, are potential alternatives to artificial sensitizers.

2.2.3.7 Electron Transfer Mediators

2.2.3.7.1 Iodide/triiodide as an Ideal Electron Transfer Mediator for DSSCs

After the initial charge separation, the charges are confined in two chemical phases. That is, electrons are confined in the semiconductor while holes (oxidized species) are confined in the Iodide/triiodide (I^-/I_3^-) redox solution that permeates the solid phase (Boschloo & Hagfeldt, 2009). The redox couple regenerates the photo-oxidized dye. In its absence, interfacial recombination takes place and results into a major energy loss. So far, I^-/I_3^- electrolyte has been the most efficient redox mediator in that I^- allows fast regeneration of the oxidized dye. In fact, it intercepts it on a nanoscale time scale (Montanari *et al.*, 2002). Schlichthorl *et al.* (1997) studied the reduction of I_2 and I_3^- and reported that a first dissociation of I_3^- in I^- and I_2 followed by a subsequent reduction of I_2 to I_2^- which is further followed by rate limiting dismutation of two I_2^- into I_3^- and I^-. It is worth noting that the reduction of I_2 arises only with adsorbed I_2 molecules. Hence, the process is further slowed down by its low concentration compared to I_3^- molecules in the solution (Huang *et al.*, 1997). Moreover, the electronic recapture involving I_3^- molecules is kinetically slow on TiO_2 and SnO_2 surfaces and that under short circuit conditions, majority of the electrons transit through the mesoporous film and the SnO_2 surface to appear in the external circuit. In this regard, the I^-/I_3^- exhibit ideal kinetic properties resulting into an asymmetric behaviour in DSSCs. That is, the forward charge donation of I^- is a simple electronic process which allows an efficient dye recovery, while the reduction of I_3^- is largely inefficient and ensures minimization of the interfacial back recombination. DSSC cathodes are coated with platinum to efficiently catalyse the I_3^- reduction. However, I^-/I_3^- is corrosive to most metals

leading to a serious problem for large area production of the solar cells as it manifests as Ohmic losses. One way of solving this problem is the deposition of metallic grids on the transparent oxides to act as electron collectors (Huang *et al.*, 1997).

2.2.3.7.2 Co(II) and Cu(I) Complexes Transfer Mediators

The Co(II) and Cu(I) Complexes transfer mediators are alternatives to the I^- / I_3^- redox couple. The electrochemical properties of coordination compounds can be tuned through appropriate design of the coordination sphere and a rational choice of the metal to have features that guarantee kinetic requirements for an electron transfer in a DSSC. In order to minimize recombination, couples which are kinetically slow are favoured. Nusbaumer *et al.* (2001) reported high concentration (0.1-0.5M) of electrolytes used in photoelectrochemical cells and thus requires substantial amount of electron mediators. As a result, the design and choice of the redox couple is based on considerations such as cost, easy synthesizability of ligands and availability of metal like elements of the first transition row.

2.2.3.8 Counter Electrodes

After receiving electrons from the external circuit, the counter electrode (CE) initiates the catalyzing process of the redox couple as a means of transporting holes. For effectiveness, the CE should have high conductivity, good stability and excellent catalytic capacity (Ye *et al.*, 2015). Platinum (Pt) CEs are commonly used in DSSCs due to their excellent electrocatalytic properties. Other metals used as CEs include Gold (Au) and Silver (Ag) as they also possess high electrocatalytic property that is desired for the reduction of the redox couples in liquid electrolytes. Nevertheless, Gold and Silver metals are expensive and, therefore, find limited use in DSSCs. Ye *et al.* (2015) also reported that ultrathin film coverage of Pt CEs introduces high defect points leading to a reduction of efficiency. Hence, due to these challenges, researchers have sought CE alternatives. For example, sulfides such as $CuInS_2$, CoS_2 and carbides such as a TiC, phosphides, nitrides, metal oxides such as WO_2 and V_2O_5 and tellurides such as CoTe

and $NiTe_2$ have been investigated and tested as CEs (Ye *et al*., 2015; Mehmood *et al*., 2014). However, so far, these alternative CEs have exhibited low PCE compared to the noble Pt, Au and Ag-based CEs.

Researchers have also investigated and tested organic materials including conductive polymers as they exhibit desired properties such as chemical stability, high transparency and electrical conductivity. Some of the conductive polymers utilized as CEs in DSSCs include PEDOT, Polyaniline (PANI) and Polypyrrote (PPY) (Ye *et al*., 2015; Mehmood *et al*., 2014). Researchers are also focusing on exploring the flexibility property of PEDOT and PANI polymers in DSSCs. Among the organic materials, PEDOT is superior because it can easily be doped hence enhancing the conductivity in DSSCs.

Carbon based materials have also been tested and found to have good electrocatalytic activity, high thermal stability, corrosive resistance and high electrical conductivity. These materials are also cheap and abundant. Carbonaceous materials such as Carbon nanotubes (CNTs), and graphene have been employed either as composites or independently as CEs (Ye *et al*., 2015; Mehmood *et al*., 2014). Graphene and graphene-based composites have stimulated immense research not only for application in DSSCs but also for other applications. The fabrication of composite CEs involves combination of two or more materials depending on the materials' compatibility and merits. The most common composites involve a combination of carbonaceous with other inorganic or organic materials. Some of the composites used as CEs in DSSCs include graphene-Pt/TaON/Nis/NIS_2.TIN/PPY among others. Composites have attracted intensive research due to their desired properties, inexpensive and their capability to be utilized as alternative CEs for DSSCs (Ye *et al*., 2015).

2.2.4 Properties of TiO_2

2.2.4.1 Crystal Structure of TiO_2

TiO_2 is a transitional metal oxide which finds wide application in in DSSCs, single and multilayer coatings, photo-catalytic applications, catalytic reactions e.g in the reduction

of (NOx) to (N_2), decomposition of volatile organic compounds (VOCs) and in gas sensors (Muaz *et al.,* 2016). Due to its chemical stability, non-toxicity and low cost, TiO_2 films have received a great deal of attention in both industrial fields and research. TiO_2 is an n-type semiconductor due to the existence of oxygen vacancies in its lattice. The vacancies arise from the release of two electrons and molecular oxygen leading to the creation of positive (+2) oxide ion vacancy. N-type semiconductor results from the presence of electrons with energy lower than the conduction band (Nolan, 2010).

TiO_2 exist in Anatase, Rutile and Brookite phases. Al-Khafaji, (2013) reported rutile as thermodynamically stable. Al-Khafaji, (2013) also noted that both anatase and brookite exhibit metastable state. In their work, Watson *et al.*, (2004) highlighted tetragonal and orthorhombic structures for both anatase and rutile and brookite, respectively. It is worth noting that the three phases consist of TiO_2^{6-} octahedral. However, the octahedrals TiO_2^{6-} bond different for the three phases. According to Watson *et al.* (2004), octahedral possess a body-centered Ti^{4+} ion which is further surrounded by a six-fold coordination of oxygen ions (O^{2-}). The $Ti-Ti$ distance in anatase phase are greater while $Ti-O$ are shorter than those observed in rutile phase (Watson *et al.*, 2004); Al-Khafaji, 2013). In addition, for rutile phase, two (out of twelve) edges are shared and thus form linear chains which are then joined to each other by sharing of corner oxygen atoms, consequently, forming a tetragonal structure (Qi, 2008). In brookite phase, both corners and edges are shared to form orthorhombic structure. It is hard to produce Brookite in nano-sized particles hence there is little known about its applications (Nolan, 2010). Figure 2.6 shows the crystallite structure of the three phases of TiO_2 (Yan *et al.,* 2017; Ma *et al.,* 2014).

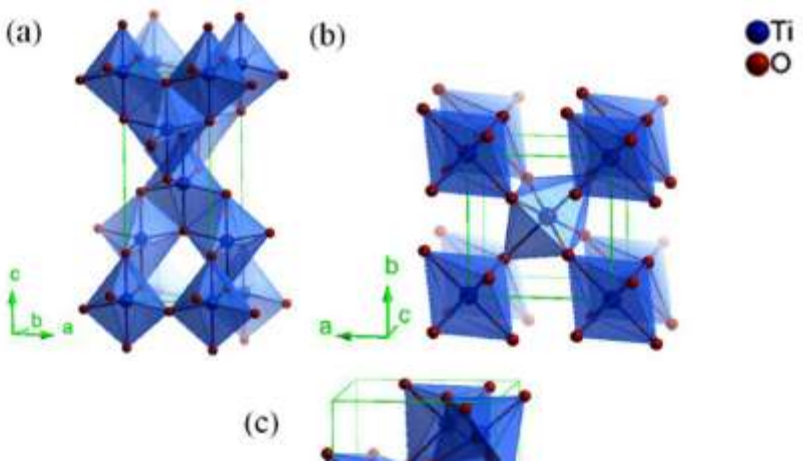

Figure 2.6: Crystallite structure of TiO_2. (a) Anatase, (b) Rutile and (c) Brookite phases.

The anatase phase possesses both photocatalysis and photo induced super hydrolysis which takes place when TiO_2-coated surfaces are subjected to ultra-violet (UV) radiation. The dual-phenomenon is quite important as it sustains the self-cleaning effect. The structural properties of TiO_2 are mainly carried out using X-ray diffraction (XRD). This method helps in the observation of the crystallinity of the semiconductor material in terms of the planes' orientations. The crystallite size can also be determined from the broadening of XRD spectrum peaks by the use of Scherer's formula.

2.2.4.2 Surface Morphology/Surface Roughness of TiO_2

While the anatase phase of TiO_2 is more suitable in the conversion of light into chemical energy due to its low recombination rate compared to rutile phase, it is crucial to note that there is synergetic effect of the mixture of the two phases in photocatalysis (Wu *et al.,* 2004). In some cases, rutile phase has been reported to be more effective than anatase as it exhibits anisotropic characteristics such as the concentration of crystallographic plan (De Mendonca & Ribeiro, 2011). It is worth noting that the TiO_2 photocatalytic properties are influenced by its surface morphology such as its topographical size, shape and area (surface roughness), phase composition, crystallite

size, concentration of lattice defects and impurities. Therefore, the effectiveness of the thin films requires crystals with well controlled physical and chemical properties especially those highlighted as being influenced by morphological aspects (Testino, 2007). Academic research findings have dwelt on synthesis of TiO_2 as well its photocatalytic activities with various shapes and sizes. However, according to Réti et al. (2017), the data has not been conclusive. Although studies point out that the materials' morphology still do not exhibit an understood role, it is important to develop a synthesis process which yields oxides with various shapes and surface topography and test their performance in various applications. This would shade light on the relationship between specific surface area, size, shape and substrate adsorption, charge transfer efficiency, hydroxyl radical ($^{\bullet}OH$) generation and photocatalytic performance of different TiO_2 films (De Mendonça *et al.,* 2014).

According to Ribeiro *et al.* (2009), based on Oxidant-peroxo method (OPM) synthesis, TiO_2 nanocrystals free from contaminants such as organic compounds and chloride ions yield into morphology which could interfere with the photocatalysis process. Therefore, through this technique, it is evident that films with different shapes, sizes and surface roughness in the anatase phase are critical to the performance of the materials. The OPM technique has been useful in the development of a model system for studying morphological parameters of TiO_2 (De Mendonca & Ribeiro, 2011).

A study of surface morphology by Atomic force Microscopy (AFM) has shown that the optical properties of oxide films depend on the surface morphology from which important information about the Oxide's microstructure can be obtained (Tian *et al.*, 2006). The AFM is mainly used to study both the atomic-scale surface structure of material as well as its surface topography. Tian *et al.,* (2006) demonstrated that surface topography of TiO_2 has a strong dependence on the thermal treatment and can be expressed in terms of Root Mean Square (RMS). In relation to optical properties of TiO_2, both absorption and scattering loss (SL) are influenced by surface roughness. That is, SL results from surface roughness and bulk defects such as microcracks and particle.

However, SL arising from surface roughness namely surface scattering loss (SSL) plays a key role in general. Assuming a RMS roughness R_a , then based on Kirchhoff diffraction integral, the reflectivity on rough interface is given by:

$$R_s = R_0 \exp\left[-\left(\frac{4\pi}{\lambda} R_a n_0\right)^2\right] \quad \text{.....2.11}$$

while the transmission SSL is expressed as:

$$SSL_t = T_0\left\{1-\exp\left[-\left(\frac{2\pi}{\lambda} R_a (n_1 - n_0)\right)^2\right]\right\} \quad \text{.....2.12}$$

Where T_0 denote the transmittance of an ideal smooth surface, n_1 and n_0 denote the refractive index of interface bilateral dielectric (Shei, 2013). Thus, Equations 2.11 and 2.12 indicate that surface morphology of TiO_2 films has great effect on the optical properties. That is, the rougher the surface is, the higher the loss by scattering. In this regard the total optical loss $R_s = I_{loss}$ of transmissivity at cutoff wavelength is the sum of absorption α_a and SSL_t .

$$I_{loss} = \alpha_a + SSL_t \quad \text{.....2.13}$$

Hence, it can be deduced that the decrease of transmissivity and the presence of red shift observed in TiO_2 films of different surface roughness result from absorption arising from the absence of oxygen as well as scattering of the rough surface (Tian *et al.*, 2006). In regard to the size and shape of TiO_2, isotropism and anisotropism have been observed in films prepared at different pH scales as shown in Figure 2.7 (Yan & Chen, 2015).

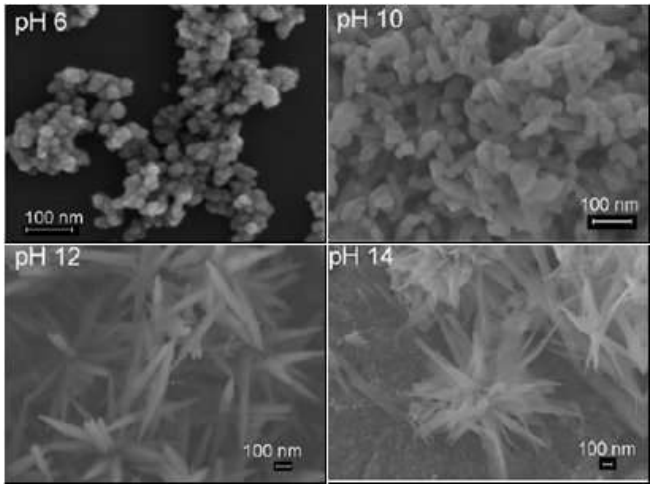

Figure 2.7: FEG-SEM images of TiO_2 samples synthesized at different pH scales, showing films with different shapes (Morphologies).

Figure 2.7 indicates that the shape of crystals varies with synthesis condition (pH). For instance, at pH 6, the sample is isotropic as it has almost spherical shape, with similar lengths determined in different directions. The sample prepared at pH 10 indicates anisotropic rod shapes with different lengths while pH 12, the sample indicates thin and elongated structures with irregular surfaces. The two samples (pH 10 and 12) exhibit anisotropic crystallographic coherence in the [004] direction parallel to [001] (Ribeiro *et al.*, 2009); Ribeiro *et al.*, 2007). Finally, at pH 14, the sample indicates irregular and shapeless morphology due to aggressive synthesis environment. Hence the crystallographic coherence is an indication of anisotropy (Ribeiro *et al.*, 2009).

The nanocrystalline mesoporous structure of TiO_2 is critical for its application in DSSCs. This structure can be achieved through chemical composition and thermal processing of the films. The mesoporous TiO_2 film in its anatase phase exhibit pores of $2-50\ nm$ in diameter. In DSSCs, the mesoporous continuous network of ordered and disordered structure of the semiconductor leads to large specific surface area. Large surface area not only facilitates mass diffusion but also increases the reaction sites, creating a favourable environment for dye adsorptions as well as heterogeneous

chemical reactions. In their work, Sedghi & Miankushki (2015) demonstrated that the mesoporous film also exhibit unique characteristics such as lack of built-in electrical field within the TiO_2 nanocrystalline particles and it has low inherent film conductivity. The mesoporous structure formation also introduces a 3D semiconductor/dye/electrolyte contact. One drawback of the mesoporous structure is that it enhances carrier charge recombination on the TiO_2/electrolyte interface. To obtain sufficient porosity and crystal structure, TiO_2 films are subjected to a slow drying up to about 175 ^oC prior sintering.

2.2.4.3 Optical Properties of TiO_2

TiO_2 has received remarkable attention due to its unique optical, photocatalytic, structural and electronic properties (Euvananont *et al.,* 2008; Bak *et al.*, 2002). The wide band gap, high refractive index, and good chemical stability, makes TiO_2 thin films find a wide application in optical coatings (Euvananont *et al.,* 2008), DSSCs (Sung & Kim, 2007) and in dielectrics (Yang & Wolden, 2006). Additionally, the high transparency of the films makes them a candidate for anti-reflection coatings as they enhance the visible transmittance in heat mirrors (Okada *et al.,* 2006). Ye *et al.,* (2007) reported refractive indices of 2.5 and 2.7 for bulk rutile and anatase titania, respectively, at $500\ nm$. Band gap values of $3.23\ eV$, $3.02\ eV$ and $3.13\ eV$ have been reported for Anatase, Rutile and Brookite films, respectively (Muaz *et al.,* 2016). The optical properties of TiO_2 are greatly dependent on the annealing temperature. Here, annealing temperature is process is heat treatment temperature at which the microstructure of TiO_2 is altered, leading to changes in its properties (Yao *et al.,* 2018). For example, the optical transmittance of TiO_2 thin films gradually decreases with increase in annealing temperature. At temperatures over 1173K, the optical loss becomes serious over the spectral range 300-800*nm* (Guang-Lei *et al.,* 2007). Other optical properties affected by temperature include, absorption coefficient, dielectric constant, optical band gap, optical conductivity, tangent loss and porosity.

Annealing increases the concentration of free charge carriers (electrons) due to TiO_2 characteristic of Anion omissions (Tian *et al.,* 2006). i.e, at low annealing rates, oxygen

vacancies occur due to the dissociation of the Oxygen atoms. This introduces stoichiometry misbalance as per the defective Equation 2.14.

$$2Ti_{Ti} + 4O_O \rightarrow 2Ti_{Ti}^{'} + V_{\ddot{O}} + 3O_O + \frac{1}{2}O_2 \uparrow \text{.....2.14}$$

Equation 2.14 can be expressed as:

$$O_O \rightarrow V_{\ddot{O}} + \frac{1}{2}O_2 \uparrow + 2e' \text{.....2.15}$$

Where $V_{\ddot{O}}$ is the concentration of oxygen vacancies and e' is the concentration of free electrons in the TiO_2 semiconductor film. Based on the mass law, for a system at equilibrium at a certain temperature, the equilibrium constant of defective Equation 2.16 becomes:

$$K_D = \frac{[V_{\ddot{O}}][P_{O_2}]^{1/2}[e']^2}{[O_O]} \text{.....2.16}$$

The constant of defective (K_D) may also be expressed in terms of Gibbs free energy as shown in Equation 2.17.

$$K_D = \exp\left(-\frac{\Delta G_O}{RT}\right) \text{.....2.17}$$

According to Tian *et al.* (2006), the concentration of oxygen vacancies can, therefore, be expressed as:

$$V_{\ddot{O}} = \left(\frac{1}{4}\right)^{-1/3} \left(P_{O_2}\right)^{-1/6} \exp\left(-\frac{\Delta G_O}{RT}\right) \text{.....2.18}$$

Where ΔG_O is Gibbs free energy, P_{O_2} is the oxygen partial pressure, T is temperature and R is the universal ideal gas constant. Equation 2.18 depicts that, at high annealing

temperatures, more oxygen molecules are released to the environment leading to the formation of oxygen vacancies while free charge carriers are also released into the bulk material. Consequently, the superfluous free electrons are trapped into the oxygen vacancy sites and hence maintain electric neutrality of the material (Tian *et al.*, 2006). Furthermore, Equation 2.18, implies that the higher the annealing temperature, the higher the concentration of the free carrier in the material (Tian *et al.*, 2006).

2.2.4.4 Photocatalytic Property of TiO_2

A chemical reaction is said to be catalyzed when its activation energy is lowered, as a result, enhancing the reaction rate (Al-Khafaji, 2013). The criterion for an efficient semiconductor photocatalyst is that the redox potential of the electron-hole pair charges couple lies within the semiconductor's band gap domain. The energy level at the bottom of the CB determines the reducing ability of photoelectrons whereas the energy level at the top of the VB determines the oxidizing ability of the photo generated holes (Mital & Tripathi, 2016). TiO_2 is renowned for its photocatalytic properties. According to Yan *et al.* (2017), the conduction band (CB) of TiO_2 is formed by the LUMO while the valence band (VB) is formed by the HOMO. The electronic band structure greatly influences the photon absorption process as well as the redox ability for photocatalysis. Only photons with energy corresponding to that of the band gap are absorbed as illustrated in Figure 2.8(a) (Kapilashrami *et al.*, 2014).

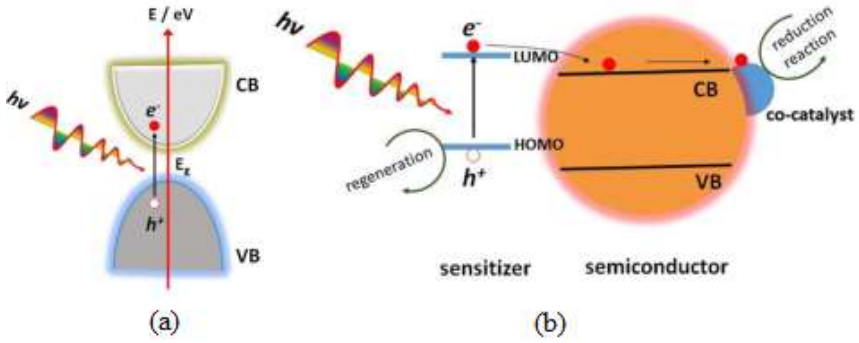

Figure 2.8: (a) Schematic illustration of the typical light-induced excitation of electrons in the VB into the unoccupied CB by absorption. (b) Mechanism of photocatalytic reaction on dye-sensitized TiO_2 semiconductor (Yan *et al.*, 2017).

Once the film is exposed to the required photon energy, electrons in the VB are excited to the CB leaving positively charged holes in the VB (Kapilashrami *et al.*, 2014). An electron-hole is, therefore, generated as expressed in Equation 2.19 (Szczepankiewicz *et al.*, 2000).

$$TiO_2 + h\upsilon \rightarrow e^- + h^+ \quad \text{.....2.19}$$

The charge carriers may be captured and trapped by defect sites on the surface or within the material, may recombine and release energy in the form of light or heat, or may migrate to the surface and generate radical species as expressed in Equations 2.20-2.22.

$$h^+ + Ti^{III}O - H \rightarrow Ti^{IV}O - H^+ \quad \text{.....2.20}$$

$$e^- + Ti^{IV}O^{\bullet} - H \rightarrow Ti^{IV}O - H^- \quad \text{.....2.21}$$

$$O_2^- + Ti^{IV}O^{\bullet} - H^+ \rightarrow Ti^{IV}O - H + O_2 \quad \text{.....2.22}$$

Studies based on electron paramagnetic resonance reported that electrons are trapped by Ti atoms to form Ti^{III} centers. On the other hand, holes are trapped as O centered radicals covalently linked to surface Ti atoms localized differently at defect sites in TiO_2 nanoparticles (Howe & Gratzel, 1987). It is worth noting that charge carriers which are captured and trapped by defect sites and those which recombine or undergo deactivation process do not play any part in photocatalysis. In this regard, the photocatalytic efficiency is determined by inhibiting the deactivation process while enhancing the migration of charge carriers to the surface to generate the radical species. In order to

improve the photocatalytic property of TiO_2, the amount of charge carriers produced upon irradiation is increased by lowering the material's band gap or by increasing the crystallinity of the film to prevent recombination of the electron-hole pairs (Yan *et al.*, 2017).

To improve light-harvesting capability on the film's surface, it is required that the film absorb photons with lower energy. That is, preferably in the visible region of the EM spectrum (Chen *et al.*, 2005). The TiO_2 band gap can be narrowed down by subjecting the film to treatments such as annealing at higher temperatures, improving the reaction time during annealing, doping with other elements and through dye sensitization. For example, Cation elements such as V^{5+}, Cr^{3+} , Ni^{2+}, Fe^{3+} and Co^{2+} can be used to replace Ti and introduce an intermediate impurity level in the energy band. The impurity level acts as electron donor or acceptor and enhances light absorption (Liu *et al,* 2015).

Self-doping, also known as dopant-free treatment, is also a band gap engineering technique that partially reduces the Ti^{4+} to Ti^{3+} and creates O vacancies throughout the material or on its surface. Self-doping not only decreases the band gap of TiO_2 but also minimizes the challenges arising from the introduction of impurities such as increased recombination sites and crystal instability (Liu *et al.,* 2013).

High temperature annealing enhances the semiconductor's crystallinity and irons out defects inside the material. The TiO_2 semiconductor may also be synthesized into one-dimensional (1D) morphologies such as nanobelts and nanotubes, nanowires, nanorods and nanofibers or into two-dimensional (2D) morphologies such as nanosheets (Tu *et al.,* 2013). The 1D and 2D morphologies have been reported to enhance charge mobility and transfer efficiency compared to their zero-dimensional (0D) counterparts. According to Wang *et al.,* (2012), the formation of junctions such as Schottky junction, phase junctions and heterojunctions within nanomaterials provide built-in assistance of electron-hole pair separation. Three-dimensional (3D) TiO_2 nanomaterial such as porous nanoflowers, shells, spheres and hierarchical super structures have also been highlighted as efficient photocatalysts. The 3D structures possess large specific area, exceptional optical, electronic and photocatalytic properties (Yu *et al.,* 2016; Liu *et al.,* 2017).

2.2.4.5 Electronic Properties of TiO_2

The electronic structure of the anatase and rutile phases of TiO_2 has been widely explored using *ab initio* methodology (Asahi *et al.,* 2000). The differences in structures between these two phases result into different densities of state (DOS) and electronic band structures, leading to different band gaps. For example, for bulk TiO_2, the band gap for anatase phase is 3.20eV while that of rutile is 3.02eV. According to Mo & Ching (1995), compared to the rutile phase, anatase exhibit similar ground-state properties except that it has large band gap while brookite phase has relatively smaller bulk modulus. The band structures along the symmetry lines of the Brillouin zone (BZ) for the three phases are shown in Figure 2.9 (Mo & Ching, 1995).

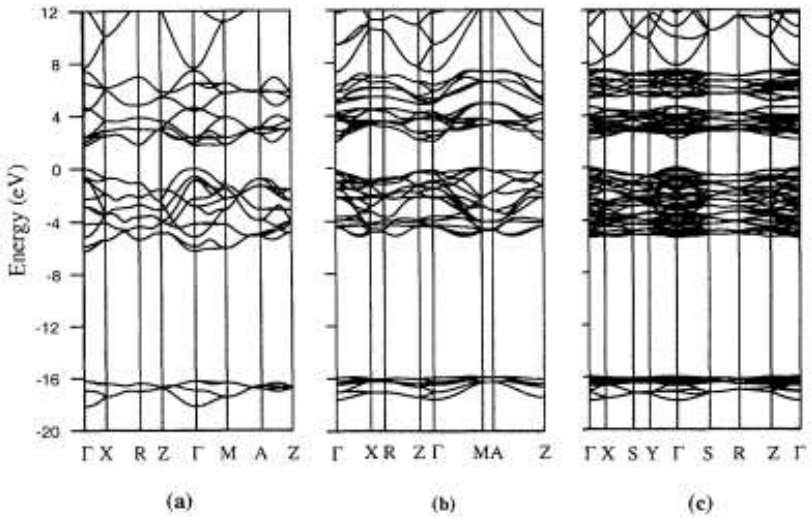

Figure 2.9: Band structures for (a) Rutile, (b) anatase and (c) Brookite TiO_2 phases.

For rutile, the calculated band gap (1.78 eV) is direct at Γ and is close to that reported by Glassford and Chelikowsky (1992). According to Mo & Ching (1995), the upper VB is composed of O_{2p} orbitals and has a width of 6.22eV while the lower O_{2s} band is 1.94 eV wide. The separation energy between the O_{2s} valence states and the minimum CB is

17.98 eV which agrees well with 17.0 eV reported by Sorantin and Schwarz (1992). The lowest CB consists of two sets of Ti_{3d} bands and exhibits a width of 5.9 eV. The two sets of bands results from the hybridized states of t_{2g} and e_g. These band structure features can be observed in a DOS diagram (Figure 2.10) (Mo & Ching, 1995).

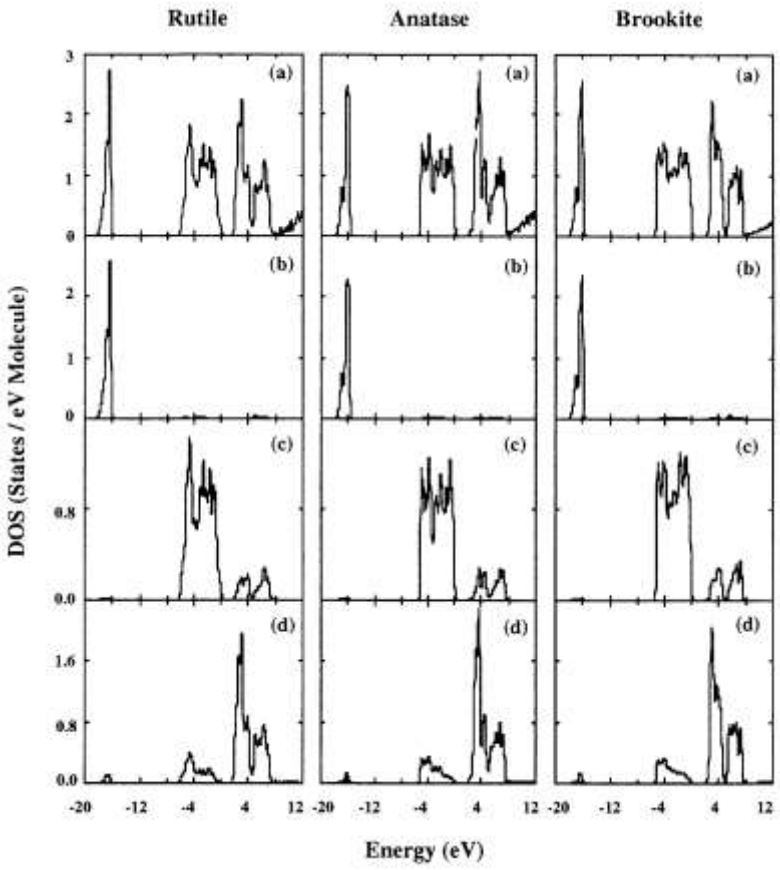

Figure 2.10: Total and partial DOSs of Rutile, anatase and Brookite TiO_2 phases: (a) Total, (b) O_{2s}, (c) O_{2p} and (d) Ti_{3d} .

An energy separation of 1.9eV between the two major features in the VB (Mulwa, 2012). A double-peak is observed in Figure 2.9 (a) for rutile and is attributed to the separation between the bonding and non-bonding O_{2p} states. A similar two-peak is also

observed in the CB. The two distinct CB features with widths 2.6 and 3.3 eV are due to crystal-field splitting of the Ti_{3d} band states. The Ti_{3d} DOS (Figure 2.10 (d)) for rutile indicates that the separation between the centroids of the two peaks in the CB is approximately 2.7 eV. The partial density of states (PDOS) for TiO_2 indicates that there is a significant hybridization between O_{2p} and Ti_{3d} in both the VB and CB regions, and hence, there exist strong interactions between Ti and O atoms in the rutile phase and that the excitation across the band gap consists of O_{2p} and Ti_{3d} states. The bottom of the CB, and the top of the VB are at the symmetrical points Γ and M, respectively. Nevertheless, it is worth noting that the energy at Γ is about 0.18 eV lower than the energy at the top of the VB. By comparison, the only notable difference in the DOS of anatase and rutile is that the double-peak feature is less distinct, particularly for the lower peak.

2.2.4.6 Surface Charge Distribution and Surface Dipole of TiO_2

Surface potential, corresponds to the work function (ϕ), is a solid state physics concept used to describe the energy needed to eject an electron from a solid and bring it to the surface in a position with negligible interaction with the solid. It is used to determine the charge distribution of a solid or thin film as it corresponds to the ionization potential studied in atomic physics. Work function also describes the minimum binding energy and relates the Fermi energy level (E_F) in a material to the vacuum potential (E_{Vac}). The E_{Vac} is the reference energy of the free electron (Borodin & Reichling, 2011). Studies have shown that the surface crossed by an electron as it is removed from the bulk has a great influence on the workfunction. For metal surfaces, this is described using surface dipole established by the electron density as the electron's wave functions extend out of the surface as well as the net positive charge in a near surface electron depleted region (Holzl & Schulte, 1979). The work function is significantly reduced by the adsorbates at the surface (Ishida & Terakura, 1987). Adsorbates such as alkali

atoms, with low ionization potential have been determined as prominent particles with adsorbate effect. For semiconductors such as TiO_2, adsorbates and surface defects introduce a higher density of band gap states thus influencing the surface dipole structure. The Alkali atoms also act as local escape channels for electrons, therefore, playing an important role in the value of workfunction (Ishii *et al.,* 1999). The adsorbate effect in changing the value of the workfunction is related to the electronegativity of the adsorbate species present as this determines their ability to induce near surface charge accumulation (Trasatti & Doubova, 1995).

TiO_2 has been extensively studied for its surface and bulk properties and it has been shown that its workfunction is influenced by concentration of oxygen vacancies generated during its preparation process (Pan *et al.,* 2013). Measurements of the workfunction of TiO_2, using Metastable Impact Electron Spectroscopy (MIES) have revealed that its specific value is reproducibly associated with each of the surface states and that it varies smoothly from one value to another with annealing for several minutes (Borodin & Reichling, 2011). Surface dipole not only determines long-range band bending but also determines the amount of energy involved in electron transfer between the semiconductor and the vacuum (kim *et al.*, 2015). Therefore, it strongly affects the overall workfunction of the semiconductor. Additionally, energy alignment influences electronic phenomena such as contact potential, Schottky barriers, photocatalysis, and the interaction between substrates and adsorbates at the heterogeneous interfaces. According to (Kim *et al.*, 2015), surface structure of materials is dependent on electric dipole. Surface dipole corresponds to the potential drop across the surface. The potential drop is given by:

$$V_{p.d} = \frac{4\pi P_m}{A} \quad \text{.....2.23}$$

Where A denotes surface area while P_m is the surface dipole moment. The potential drop changes as the surface undergoes compositional and structural deformations or

changes. The change in the microscopic electrostatic potential defined as ΔV is expressed as:

$$\Delta V = V_{Vac}^{slab} - V_{Center}^{slab} \quad \text{.....2.24}$$

Where V_{center}^{slab} is the potential at the center of the film while V_{Vac}^{slab} is the potential at the vacuum (Kim *et al.,* 2015). A more negative value of ΔV indicates the presence of a greater barrier for the electrons to escape to the vacuum. The ΔV has been found to be high due to changes in oxygen partial pressure and pH (Badwal *et al.,* 2001). In metals, adsorption results into the formation of a dipole layer (V_{dipole}) (Hayashi *et al.,* 2002). The phenomenon of a drop in negative potential across a material may be described in that, though the material may be nonpolar, deformations near its surface results into surface dipole layers expressed as (Mugo & Yuan, 2012):

$$V_{dipole} = \frac{N_{mol}}{\varepsilon}(P_m . n_v) \quad \text{.....2.25}$$

Where N_{mol} denote density of adsorbed species, ε is dielectric constant, P_m is dipole moment and n_v is a vector normal to surface (Hayashi *et al.*, 2002; Mugo & Yuan, 2012). During oxidation of the surface, oxygen-rich reconstructions are favoured inducing negative charge to the surface and making the ions near the surface more negative. This appears as an added dipole moment which points into the surface, hence, leading to a more negative potential drop across it (Kim *et al.,* 2015). In practice, the workfunction on the surface of the sample is determined by several parameters given by Equation 2.26 and as illustrated in Figure 2.10 (Kim *et al.,* 2012).

$$\phi = \left(E_C - E_F\right) - eV_S + \chi - \Delta\phi \quad \text{.....2.26}$$

Where ϕ is the work function of the sample, eV_S is surface band bending, χ is electron affinity and $\Delta\phi$ is the surface dipole energy. The variation in ϕ is, therefore, described

based on not only the doping concentration $(E_C - E_F)$but also the dipole layers and surface band bending (Kronik & Shapira, 1999).

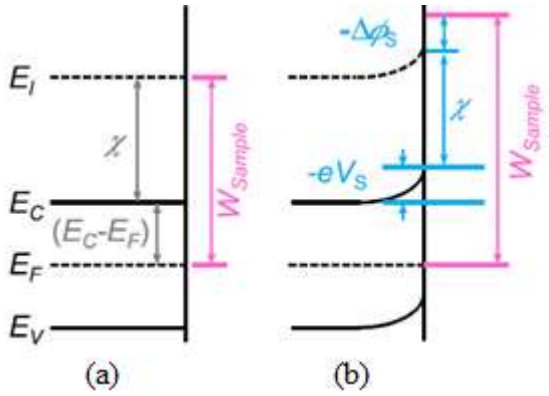

Figure 2.11: Schematic diagrams of the electronic band structures at an *n*-type semiconductor surface (a) without and (b) with surface band bending and surface dipole.

For *n*-type semiconductors (TiO_2), oxygen molecules adsorbed on its surface capture electrons from its oxide (as expressed in Equation 2.27) inducing surface depletion region. This may result into upward band bending (Figure 2.11(b)). That is, $eV_S < 0$. This consequently results into increase workfunction of TiO_2 (Rothschild *et al.*, 2003).

$$O_2(g) + e^- \rightarrow O_2^-(ad) \quad \text{.....2.27}$$

Where O_2^- is adsorbed oxygen ions. Chemisorption of polar molecules such as water, form dipole layers which also raise the ϕ of TiO_2.

2.2.5 Operating Principle of a DSSC

The conversion of photonic energy into electric energy follows a number of steps in a DSSC. The steps include excitation of the dye, charge injection of electrons into semiconductor material, and charge transport in the DSSC electrodes. The working

principles of a DSSCs mimics photosynthesis in plants (Dodoo-Arhin *et al*., 2013). Figure 2.12 represents the operating principle of a DSSC (Marinado, 2009).

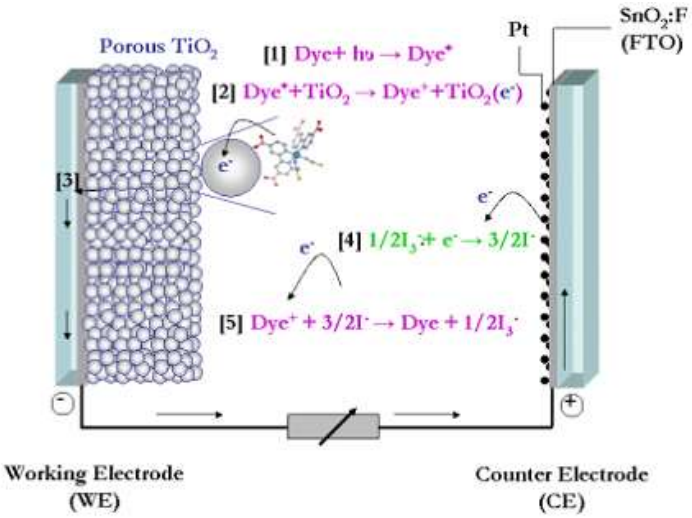

Figure 2.12: Schematic illustration of the operation of a DSSC. [1] Dye excitation, [2] electron injection from photo-excited dye into Semiconductor (TiO_2), [3] charge collection in WE, [4] triiodide reduction at the CE and [5] regeneration of the oxidized dye.

2.2.5.1 Dye Excitation

Metallorganic Ru-complex (N719) dye is commonly used in DSSCs. The dye is excited by absorption of a photon of sufficient energy upon illumination of the DSSC. The nanocrystalline mesoporous TiO_2 working electrode, into which the dye is adsorbed, provide large internal surface area for light absorption (Katoh, 2012). Upon photon absorption, the dye molecules are excited from the HOMO to the LUMO. Photon absorption in Ru (II) complex dye is more prominent in the visible range of EM spectrum. The process is represented by:

$$S_{dye} + h\upsilon \rightarrow S^{*}_{dye} \quad \text{.....2.28}$$

Here, S_{dye} and S^*_{dye} denote ruthenium dye before and after excitation, respectively.

2.2.5.2 Electron Injection into TiO_2

The excitation of the adsorbed dye is followed by injection of electrons in the CB of the semiconductor (TiO_2) leading to oxidization of the dye. The injection process is represented in Equation 2.29 (Katoh *et al*., 2007). The injection rate ranges between 100fs and 100ps.

$$S^* + TiO_2 \rightarrow S^+ + e^-_{(TiO_2)} \quad \text{.....2.29}$$

For enhanced electron injection, Katoh (2012) reported that the LUMO of the dye should be about 0.3eV above the semiconductor's CB.

2.2.5.3 Electron Diffusion in TiO_2

The mesoporous TiO_2 thin film consist of nanocrystalline spherical particles of 15-20 *nm* in diameter. The material is *n*-doped semiconductor due to oxygen vacancies in the lattice with a carrier concentration of $N_D = 10^{16}$ (Chen *et al*., 2014). Electron transfer in the film occurs mainly by diffusion via electron trapping and de-trapping mechanism. According to Chen *et al*. (2014), the optimized thickness of TiO_2 film is in the range $8-10\ \mu m$. This indicates that the diffusion length of the electrons is within this range. The electron lifetime is expresses by:

$$\tau_e = \frac{D_l^2}{D_{eff}} \quad \text{.....2.30}$$

$$e^-_{TiO_2} + Electrode \rightarrow TiO_2 + e^-_{electrode} + Energy \quad \text{.....2.31}$$

Here, τ_e is the electron lifetime, D_{eff} is the effective diffusion coefficient and D_l is the diffusion length. The electron then diffuses from the TiO_2 into the FTO and finally flows

through the outer electrical circuit to do work. The entire process is expressed in Equation 2.31 (Chen *et al.*, 2014). In DSSCs, the diffusion length D_l of the TiO_2 film must be minimized in order to enhance the charge collection efficiency (η_{CC}), a parameter related to the recombination time constant (τ_R) as shown in Equation 2.32.

$$\eta_{CC} = 1 - \frac{\tau_C}{\tau_R} \quad \text{.....2.32}$$

Here, τ_C represents electron collection time constant, have units of time and is a function of photovoltage (V_{Ph}) (Wei *et al.*, 2010). Kopidakis *et al.*, (2003) reported an exponential variation of τ_R with V_{Ph} due to the multi-trap charge recombination which occurs in DSSCs with large working areas. Furthermore, Yan *et al.* (2019) reported an exponential relationship between τ_R and open circuit voltage V_{OC} as shown in Equation 2.33.

$$\tau_R = \zeta \exp\left[\frac{eV_{OC}}{K_B}\left(\frac{1}{T_0} - \frac{1}{T}\right)\right] \quad \text{.....2.33}$$

Where ζ is a pre-exponential factor and $K_B T_0$ denote mean characteristic energy for determining trap states involved in charge recombination.

2.2.5.4 Triiodide Electrolyte Reduction

After the electron has done work in the external load, it travels to the Pt CE to reduce the triiodide. The Pt CE acts as catalyst as well as a transporter of the reactants to the electrolyte (Katoh *et al.*, 2007). Equation 2.34 represents the dark cathode reaction. It is worth noting that recombination is more likely to occur if the reduction at the excited dye region is not effective. Also, the rate at which the triiodide is reduced is usually

higher than the recombination at the TiO_2/redox couple interface. For better performance of the DSSC, dye with efficient adsorption is desired as this property inhibits the proximity of electrolyte to the TiO_2 film.

$$\frac{1}{2}I_3^- + e_{CE}^- \rightarrow \frac{3}{2}I^- \quad \text{.....2.34}$$

2.2.5.5 Dye Regeneration

During the dye regeneration process, the oxidized dye molecules receive the electron from the iodide redox mediator. The process occurs very fast at nanosecond scale. In fact, the rate at which it occurs is 100 times faster than recombination reaction and about 10^8 faster than the lifetime of the oxidized dye. This is very crucial as it inhibits any chance of recombination (Katoh *et al.,* 2007). The two Equations governing the dye regeneration process are:

$$S^* + \frac{3}{2}I^- \rightarrow S + \frac{1}{2}I_2^- \quad \text{.....2.35}$$

$$2I_2^- \rightarrow I^- + I_3^- \quad \text{.....2.36}$$

According to Katoh *et al.* (2007), the two-step electron transfer mechanism requires an electromotive force of about 600mV due to the mismatch that arises between the redox couple and the dye.

2.2.6 TiO_2 Optical Parameters

2.2.6.1 Absorption and Extinction Coefficients, Refractive Index and Porosity

The transmittance of TiO_2 thin films is crucial in the study of the effect of annealing temperature on the films. According to Shinen *et al.* (2018), the average transmittance of a TiO_2 monolayer on a glass substrate is greater than 95% in the spectral wavelength range of 300–1000 nm. The absorbance of the TiO_2 indicates the amount of photons

absorbed by the thin films and can be obtained from the transmittance and reflectance spectra as shown in Equation 2.37 (Shinen *et al.*, 2018).

$$A_b = 1-(T_r + R_f) \quad \text{.....2.37}$$

Where A_b is absorbance, T_r is transmittance and R_f is reflectance of the thin films. The absorption (α) and extinction coefficients (K_{ex}) are functions of film thickness and Transmittance as shown in Equations 2.38 and 2.39, respectively. Absorption coefficient is the ratio of decrement in electric flux of the incident EM energy to unit distance in the direction of incident wave and is depended on the incident EM energy and the semiconductor characteristics. That is, n- or p-type (Neamen, 2012).

$$\alpha = \left(\frac{1}{d}\right)\ln\left(\frac{1}{T}\right) \quad \text{.....2.38}$$

$$K_{ex} = \frac{\alpha\lambda}{4\pi} \quad \text{.....2.39}$$

Where d is film thickness, T is transmittance of the films and λ is wavelength. The absorption coefficient may, therefore, be described as the reciprocal of the depth of penetration of EM radiation into the thin film (Voss *et al.*, 1998). On the other hand, the extinction coefficient corresponds to the damping factor or decay of the amplitude of EM field. The extinction coefficient may also be seen as the measure of the absorbed EM radiation. That is, $K_{ex} > 0$ implies that there is absorption while $K_{ex} = 0$ implies zero absorption of EM radiation by the films (Voss *et al.*, 1998).

The refractive index (n) is a measure of the bending of a ray of light as it passes from one medium into another. Based on the Transmittance of TiO_2 thin films, refractive index can be obtained using Equations 2.40 and 2.41.

$$n = \left(N + \sqrt{N^2 - n_s^2}\right)^{1/2} \quad \text{.....2.40}$$

$$n_s = \frac{1}{T_s} + \left(\frac{1}{T_s} - 1\right)^{1/2} \quad \text{.....2.41}$$

Where $N = 2n_s \frac{T_M - T_m}{T_M T_m} + \frac{n_s^2 + 1}{2}$, T_M and T_m are the maximum and minimum transmissions corresponding to a certain wavelength λ, T_s and n_s denote the substrate's transmittance and the refractive index. Porosity, expressed in percentage, can be evaluated in terms of the refractive index spectra (Swanepoel, 1983). Mathematically, Porosity is expressed as:

$$P_o(\%) = \left(1 - \frac{n^2 - 1}{n_b^2 - 1}\right) \times 100 \quad \text{.....2.42}$$

Here n denote the refractive index of the porous films where as $n_b = 2.52$ denote the refractive index of pore-free anatase film obtained at $550nm$ (Mathews *et al.,* 2009; Hou *et al.,* 2003). High porosity indicates large surface area which promotes reaction sites by enhancing dye adsorptions in DSSCs (Zhou *et al.,* 2018). Optical band gap is crucial in the examination of the photocatalytic activity of TiO_2 films. Optical band gap is a measure of the concentration of free charge carriers in the CB. The band gap is affected by the film processing technique, film thickness and annealing temperature and is determined using Tauc Equation (Shinen *et al.,* 2018; Zhao *et al.,* 2011):

$$(\alpha h\upsilon)^{\gamma} = A(h\upsilon - E_g) \quad \text{.....2.43.}$$

Where $h\upsilon$ is the photon energy, γ the transition coefficient ($\gamma = 2$ and $\gamma = 1/2$ for direct and indirect interband transitions, respectively). Here, A is a constant depends on the material. The optical band gap is also a measure of the structural properties of the

material as it signifies the level of densification, and hence crystallinity (Yarmand & Sadrnezhaad, 2010; Bartic *et al.*, 2013).

2.2.6.2 Dielectric Constant and Loss Tangent

The dielectric constant (ε) can be expressed in terms of the real (ε_r) and imaginary (ε_i) dielectric constants as shown in Equation 2.44. The ε_r and ε_i dielectric constants indicate the extent to which TiO_2 films slow down the speed of incident light and the extent to which dielectric absorbs energy from the applied electric field due to dipole motion, respectively (Makhlouf *et al.*, 2014).

$$\left.\begin{aligned} \varepsilon &= \varepsilon_r - i\varepsilon_i \\ \varepsilon_r &= n^2 - K_{ex}^2 \\ \varepsilon_i &= 2nK_{ex} \end{aligned}\right\} \quad \text{.....2.44}$$

While ε_r depicts the maximum energy that can be stored in the material, ε_i (relative loss factor) indicates the measure of the absorption of electrical energy by a dielectric material subjected to EM field (El-Nahass *et al.*, 2016). On the other hand, the loss tangent ($\tan\delta$) is the ratio of ε_i to ε_r and is a measure of the extent to which TiO_2 thin films absorb EM field and is given by:

$$Tan\delta = \frac{\varepsilon_i}{\varepsilon_r} = \frac{2nK_{ex}}{n^2 - K_{ex}} \text{.....2.45}$$

Where δ (Loss angle) is the phase difference between the induced current and the applied EM field (El-Nahass *et al.*, 2012). Loss tangent also indicates the spectral window at which band transitions occur and can also be expressed as the ratio of conduction current density J_C to displacement current density J_D (Equation 2.46).

$$Tan\delta = \frac{|J_C|}{|J_D|} = \frac{|\sigma\vec{E}|}{|j\omega\xi\vec{E}|} = \frac{\sigma}{\omega\xi} \quad \text{.....2.46}$$

Where $\vec{E}$ is the electric field intensity, σ is the conductivity of the films, ξ is the permittivity of the films and ω is frequency of the EM field.

2.2.6.3 Optical Conductivity

The optical conductivity of TiO_2 is a complex term expressed in both absorption coefficient and refractive index. It is given by:

$$\sigma = \sigma_r + i\sigma_i = \frac{\alpha nc}{4\pi} \quad \text{.....2.47}$$

Where $\sigma_r = \omega\varepsilon_o\varepsilon_i$ is real conductivity and $\sigma_i = \omega\varepsilon_o\varepsilon_r$ is imaginary conductivity and $\varepsilon = \varepsilon_r - i\varepsilon_i$ is permittivity of the medium, ω is the angular frequency, ε_o is the free space dielectric constant and c is the velocity of light (Sharma & Katyal 2007; El-Nahass *et al.*, 2016). Optical conductivity is the ease at which the electromagnetic field is able to induce electric charges on the surface of the films. The determination of optical conductivity in TiO_2 is crucial as it indicates the spectral range and response within which TiO_2-based Photoanodes can be applied in DSSCs (El-Nahass *et al.*, 2016).

2.2.6.4 Energy Loss

Energy loss due to the application of electromagnetic field occurs due to electron transition within solids of thin films. Energy loss describes the energy absorbed (or energy lost by the free charge carriers) as they pass through the film. It has two components (Surface Energy Loss S_{EL} and Volume Energy Loss V_{EL}) which are expressed in terms of ε_r and ε_i as shown in Equations 2.48 and 2.49.

$$S_{EL} = \mathrm{Im}\left(\frac{-1}{\varepsilon(\omega)} + 1\right) = \frac{\varepsilon_i}{\varepsilon_i^2 + \left(1 + \varepsilon_r^2\right)^2} \quad \text{.....2.48}$$

$$V_{EL} = \mathrm{Im}\left(\frac{-1}{\varepsilon(\omega)}\right) = \frac{\varepsilon_i}{\left(\varepsilon_i^2 + \varepsilon_r^2\right)^2} \quad \text{.....2.49}$$

Here, $\varepsilon(\omega)$ is the frequency-dependent dielectric function of the bulk solid. In TiO_2 thin films, the S_{EL} and V_{EL} are used to describe the losses in terms of absorption due to inter-band electronic transitions as well as electronic scattering (El-Nahass *et al.,* 2016; Park 2012).

2.2.6.5 Band Transition Probability and Free Carrier Concentration

The V_{EL} may be explained in terms of inter-band carrier transition probability J_{VC} (Equation 1.50) (Badran *et al.,* 2012; French, 2000).

$$j_{VC} = \mathrm{Re}\, J_{VC} + \mathrm{Im}\, J_{VC} = \frac{4\pi m_o^2}{e^2 h^2} \frac{E^2}{2} \left(\varepsilon_{\mathrm{Im}} + i\varepsilon_r\right) \quad \text{.....2.50}$$

Where $\mathrm{Re}\, J_{VC}$, $\mathrm{Im}\, J_{VC}$ are the real and imaginary part of inter-band transition strength, m_o mass of the electron, E is the photon energy, e charge of the electron and h Planck's constant. J_{VC} has units $g.cm^{-3}$ and accounts for the dipole selection rules for the transitions and is proportional to the probability that a transition of an electron between the filled valence band and the empty conduction band with transition energy takes place and is related to complex dielectric constant (Badran, 2012; French, 2000). The inter-band electronic transition in thin films may be accounted in the form of optical absorption coefficient which is a function of concentration of charges (Tian *et al.,* 2006). It is given by:

$$\alpha = \frac{N_D e^2 \lambda_0^2}{\varepsilon_0 m^* 8\pi c^3 \tau'} \quad \text{.....2.51}$$

Where N_D is concentration of charge carriers, λ_0 is absorption wavelength, ε_0 is permittivity of free space, e is electronic charge, c is the speed of light, m^* is the effective mass of the free carriers and τ'. Here, high concentration of charge carriers results to high absorption coefficient (Tian *et al.,* 2006).

2.2.7 Surface Charge Distribution and Work function

The surface charge distribution is measured in terms of surface potential difference or contact potential differences. It reveals information about thin films' surface charging and is related to the sample work function (ϕ_{Sample}). According to Zerweck *et al.* (2005), the workfunction of thin films is given by:

$$\phi_{sample} = \phi_{tip} - SP \quad \text{.....2.52}$$

Where ϕ_{Tip} denote the work functions of the Gold tip, and SP is the surface potential recorded in the SKPM measurements (Lang & Kohn, 1971). The films' work function is dependent on the structural properties which may be tuned through chemical and annealing processes (Kim *et al.,* 2015).

CHAPTER THREE
MATERIALS AND METHODS

3.1 Background

This chapter entails the synthesis and characterization of WEs and CEs, fabrication and characterization techniques used on DSSCs and DSSMs. The various characterization for the electrodes include, optical microscopy, UV-Vis spectrophotometry, XRD and surface potential measurements using SKPM.

3.2 Preparation of TiO_2 Working Electrodes

The preparation process involved cleaning of FTO SnO_2:F glass substrates (sourced from *Xinyan* Technology Co. Limited, China), application of titanium nanoxide T/SP through doctor blading (Frederichi *et al.,* 2021), drying, annealing and sintering of samples.

3.2.1 Cleaning

The FTO SnO_2:F glass substrates were cut into 2 x 1.5 cm (for the DSSCs) and 4 x 0.4 cm (for the DSSMs) using a diamond glass cutter. The cut FTO glass substrates were then cleaned for 5 minutes in acetone (Analytical grade-purity 99.5%) using cotton swamps. The glass substrates were then dipped in ethanol (purity 99.5%) and cleaned for five minutes before rinsing with deionized water for five minutes. They were then dried with warm pressurized air and stored in clean sample boxes.

3.2.2 Application of Titania Nanoxide Paste

A 1 x 1 cm^2 window (for DSSCs) and 0.4 x 4 cm^2 (for DSSMs) were cut from a scotch magic tape and placed on the conductive side of the FTO glass substrates. Titanium nanoxide T/SP (18% wt, 15-20 nm, *Solaronix,* Switzerland) was stirred using a clean glass stirrer. Shaking was avoided as it introduces air bubbles which hinter good deposition. The conductive FTO film on each glass substrate was identified through continuity testing using a mutltimeter. Thin films of nanocrystalline TiO_2 were then applied by doctor blading the titanium nanoxide paste on the conductive side of the FTO glass substrates using a clean tapered glass. Doctor blade coating involved placing a tapered blade at a fixed distance from the FTO substrate, placing the titanium nanoxide paste in front of the blade and then moving it in-line with the substrate, creating a thin film (Frederichi *et al.,* 2021). The scotch tape was then carefully removed and the coated glass placed in a petri dish and covered for 20 minutes to enhance homogeneity of the

film. In order to obtain the desired film thickness, a uniform pressure was applied in the pasting region.

3.2.3 Drying and Sintering 0111487864

The TiO_2 films were then placed in a KL 420 muffle furnace and the temperature ramped from 25 ^oC at 5 ^oC per minute up to 175 ^oC (Ngei, 2016). Further, to enhance their roughness and crystallinity, sintering was allowed at 450 ^oC for 30 minutes and, subsequently, cooling of the films was attained by systematically lowering the temperature at the same 5 ^oC per minute rate. Other TiO_2 thin film samples were prepared annealed at different annealing rates of 1 ^oC per minute, 2 ^oC per minute and subsequently sintering of the films at 450 ^oC for 30 minutes. Some more films were subjected to 1-step annealing scheme from 25 ^oC room temperature to 450 ^oC. The films were further subjected to sintering at 450 ^oC for 30 minutes. The thickness was measured with an alpha step profilometer after sintering. Figure 3.1 shows schematic representation of the working electrode preparation process.

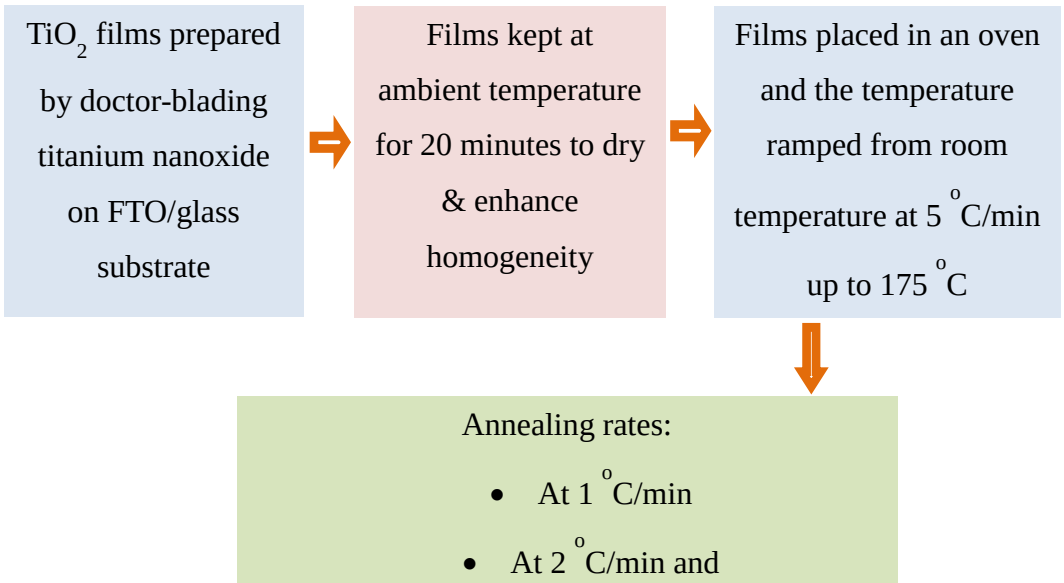

Figure 3.1: Schematic representation of the working electrode preparation procedure.

3.3 Preparation of Ru(II) dye

A 0.5mM N719 dye (cis-diisothiocyanato-bis (2,2'-bipyridyl-4,4'-dicarboxylato) ruthenium(II) bis (tetrabutylammonium) sourced from Solaronix, Switzerland, was prepared by dissolving 200 mg of the N719 dye in 100ml of ethanol (purity, 99.5%) in a conical flax. The molecular formula of N719 dye is $C_{58}H_{86}O_8N_8S_2$. The preparation of 0.5 mM solution was in accordance to Equation 3.1:

$$C = \frac{m}{V}\frac{1}{MW} \quad \text{.....3.1}$$

Where C denotes molar concentration in mol/L, m represents mass of dye in grams, V represents formula weight and $MW = 1188.6\ g/mol$ is the relative formula mass of the dye. The solution was then stirred thoroughly for the dye to dissolve. The conical flask was further sealed and shaken for ten minutes using a digital shaking rotator. The solution was stored in a dark room to prevent degradation from light exposure.

3.4 TiO_2 Dye Sensitization

The dye was poured into staining boxes and the working electrodes immersed carefully. To ensure there was no interference on the TiO_2 film through contact, each staining box contained one film. The films were placed with the TiO_2 coated side facing upwards in order to prevent contact of the films with the wall of the staining boxes. The electrodes were kept in the staining boxes for 24 hours for maximum dye loading. The dye loading in each sample was quantitatively analyzed using UV-Vis-NIR spectrophotometer.

3.5 Preparation of Platinum Counter Electrodes

Platinum counter electrodes films of different sizes (1 x 1 and 0.4 x 4 cm^2) were prepared. The films were all subjected to 2 ^{0}C/Min annealing rate and sintered at 400^{0}C for 30 minutes to activate the films. The preparation procedure entailed cleaning of FTO glass substrates, application of Platisol T/SP paste through doctor blading technique, drying and sintering of the films.

3.5.1 Cleaning

The FTO SnO_2:F glass substrates were cut into pieces (2.0 x 1.5 cm) using diamond cutter and their sheet resistance of 7 Ω/cm^2 determined using the mutltimeter. The FTO SnO_2:F glass substrates and the tapered glass were then cleaned using acetone and ethanol both of analytical grade (purity 99.5%) and finally rinsed in deionized water. The glass substrates and the tapered glass were then dried using pressurized warm air.

3.5.2 Application of Platisol T/SP Paste

Different scotch tapes were cut into 1 x 1 cm^2 and 0.4 x 4 cm^2 windows and then placed on the conductive sides of the FTO glass substrates. A thin film of Platinum was doctor bladed on the conductive side of the FTO glass substrates by applying Platisol T/SP (*Solaronix*, Switzerland) paste. The samples were kept in clean dark sample boxes for 20 minutes in order to enhance surface homogeneity. The films were then annealed at 2 -

^{0}C/Minute and sintered at 400 ^{0}C for 30 minutes. Sintering was ensured to activate the Platinum films. The films were allowed to cool in the KL 420 muffle furnace. After cooling, the films were promptly characterized using UV-Vis-NIR spectrophotometer and alpha step profilometer and consequently used to fabricate the DSSCs and DSSMs.

3.5.3 Measurement of Surface Morphology

To measure the surface topology, the surface of the films was focused using a high resolution optical microscope model: *Zeiss Axio Zoom V16*. The microscope was set under reflection mode and three sets of images obtained at magnifications 16, 100 and 260X. The microscope consists of three LEDs mounted on the sides of its stage. The LEDs emit visible light, which is subsequently reflected by the films, after passing through a 1 *mm* aperture. The light is then directed to a lens and finally detected by CCD camera (pixel size: $3.4 \times 3.4\ \mu m$), model *AxioCam Mrc5* interfaced with a PC. Optical 8-bit images were obtained using the CCD camera at 2584×1936 (5Mpixel) resolution. Subsequently, processing of the optical images in terms of contrast was achieved using image analysis software (*Imagej 1.48v*). The contrast was analysed using histogram distributions and line profiles.

3.5.4 Optical Characterization of TiO_2 Films

3.5.4.1 Absorption and Transmittance Measurements

A UV-VIS spectrophotometer (*Perkin Elmer Lambda 950*) was used to obtain the transmittance of the films within $250 - 800\ nm$ spectral wavelength (Figure 3.2).

Figure 3.2: Optical image of a UV-Vis spectrophotometer (*Perkin Elmer Lambda 950*) used in this work (Karlsruhe Institute of technology-Germany)

The measurements were obtained at a normal incidence using a reference substrate. From the transmittance data, other optical parameters including refractive index, absorption coefficient, extinction coefficient, dielectric constants, loss tangent, optical conductivity and optical band gap of the thin films was obtained. UV-Vis spectrophotometer was vital in the analysis of the optical properties which revealed the optical properties of the sample (Swanepoel, 1983).

3.5.5 Structural Measurements (XRD)

For the structure, the film crystalline phases were characterized using X-ray diffractometer (*K alpha 1504 Armstrongs*) (at Karlsruhe Institute of technology-Germany) with a Cu-K_α radiation ($K_\alpha = 0.15406\ nm$) and operating at an accelerating voltage of 40 kV and an emission current of $4\,mA$. Data was acquired over a range of $20^0 \leq 2\theta \leq 80^0$ Bragg's angle at a sampling width of 0.1^0 and a scanning speed of 1.2 ^{o}/Min. The Scherer Equation was used to determine the crystallite sizes of the TiO_2

films. *Crytalsim* software was also used to determine the possible set of Miller indices representing planes of the nanocrystalline TiO_2 thin films.

3.5.6 Surface Charge Distribution Measurements (SKPM)

A Kelvin Probe System (*KP- Technologies Kelvin Probe System*) with a gold tip of $\Phi = 5.2eV$ (5200mV) was used to obtain the contact potential differences V_{cpd} in the form of a line, point and area scans. During the SKPM measurements, a cantilever with gold coated tip was used in the noncontact mode. The applied bias to the tip had both alternating and direct current components, which were far less than the mechanical resonance frequency of the cantilever (ω_r) 170 kHz. The samples were placed on a movable stage inside the Kelvin Probe system and the gold tip allowed to scan over the surface charge distribution was observed as surface potential V_{cpd} data via a PC interfaced with the *KP- Technologies Kelvin Probe System as* shown in Figure 3.3. In this work, the *KP- Technologies Kelvin Probe System* works by extracting the frequency component ω of the gold tip deflection. The extracted frequency component is proportional to the electrostatic force, F_ω.

Further, the SKPM data obtained was independent of the specific tip surface and the applied V_{AC}. Since the a feedback loop is normally employed to minimize the F_ω between the sample and the tip by adjusting the applied bias V_{DC}, it was possible to obtain a contour map of $V_{DC} = V_{cpd}$.

Figure 3.3: Optical image of SKPM (*KP- Technologies Kelvin Probe System)* (Chuka University- Kenya)

3.6 Optical Measurement of Platinum films

3.6.1 Transmittance of Platinum films

The transmittance spectral curves of bare FTO and Platinum on FTO were obtained using UV-VIS spectrophotometer (*Perkin Elmer Lambda 950*) and the Shimadzu SolidSpec-3700DUV spectrophotometer by placing the samples on the already preset spectrophotometers. The baseline wavelength was set in the range $350-100\ nm$. To obtain the transmittance spectra, the samples were placed in the transmission chamber of the instruments and then spectra run. The procedure was repeated for all platinum samples and the data was recorded and in the interfaced PC. The data was then processed using *Origin Pro* version 8.5 software.

3.7 Determination of Electrode Film Thickness

Each of the CE and WE was placed in an Alpha Stylus Profilometer stylus chamber and their thickness determined. Each sample was run on the four sides of the sample and the average value of the thickness recorded.

3.8 Dye loading of TiO_2 Films

Dye loading is referred to as the adsorption of the dye molecules into the mesoporous thin films. The absorbance of the dye was determined by, first, obtaining the transmittance and reflectance spectra of TiO_2 films before they were dye sensitized. The films were then soaked in the 0.5 mM Ruthenium (II) dye (N719) for 24 hours for adsorption to take place. After the dye loading, reflectance and transmittance spectra of the samples were carried out using UV-Vis-NIR spectrophotometer after which dye loading was quantitatively determined from the spectra.

3.9 Fabrication of DSSCs

The dye-adsorbed TiO_2 WEs and the Platinum CEs were assembled into solar cell using sealant (DuPont surlyn- Meltonix 1170-25 *Solaronix*, Switzerland) with a micro-space at 80 ^oC. the electrolyte (iodine/triiodide), 30 mM of ionic liquid, thiocyanate on acetonitrile solvent, pyridine derivative, lithium salt, (Iodolyte HI-30, *Solaronix*, Switzerland) was injected via the micro-space after which the cells were sealed using the sealant melt. The DSSCs were kept in the dark for 24 hours. Figure 3.4 represents a schematic illustration of the fabrication process of DSSCs.

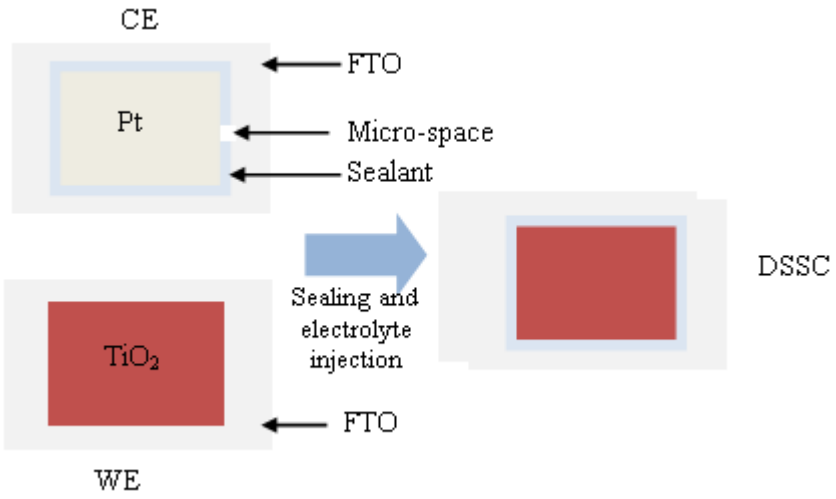

Figure 3.4: DSSC fabrication process showing the counter electrode (CE), working electrode (WE) and the sandwiched solar cell.

3.9.1 Fabrication of DSSMs

Two schemes of connections were adopted for the fabrication of the DSSMs. The schemes involved the connection of the single cells of 0.4 x 4 cm^2 in series connection and in parallel connection as reported by Hastuti *et al.* (2016) (Figure 3.5). In the series

and parallel external circuit, the DSSMs were tested from two, three, four, five and six cells. The I-V characteristics and the analysis of the PCE of each set were obtained.

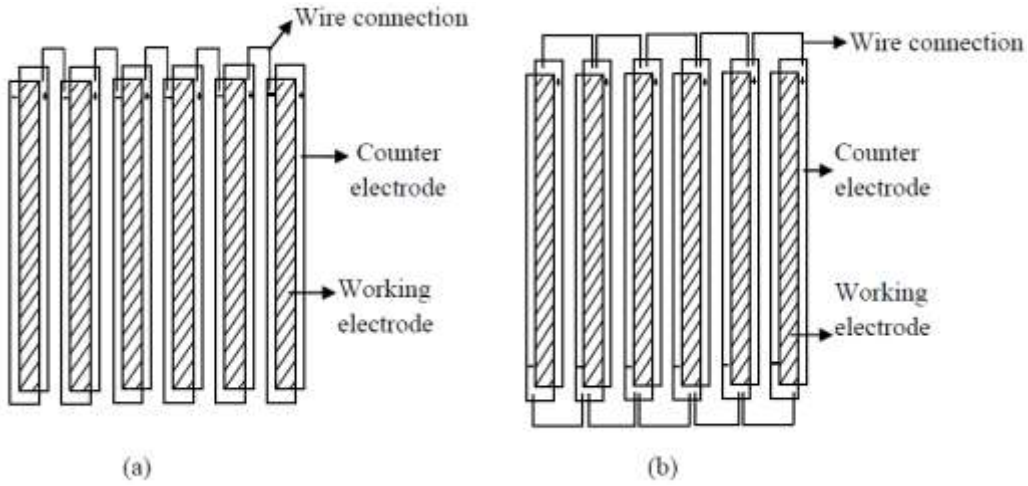

Figure 3.5: Schematic of DSSMs (a) series external circuit (b) Parallel external circuit.

The DSSMs I-V characteristics and subsequent analysis was conducted to ascertain the effect of the increasing cell surface area on the PCE.

3.10 I-V Characteristic Measurements

The DSSCs and DSSMs were characterized by plotting and analysing the I-V characteristic curve obtained through applying an external bias on the DSSCs in a dark room. A halogen lamp (450 W) adjusted to an intensity output of 100 mW/cm^2 was used as the source of solar power input. In order to maintain the irradiation on the DSSCs and DSSMs at AM1.5 (1 sun), a solar power meter TM206 (3T0-3-1, Tenmars, Taiwan) and a single crystal Si photodiode were used. The distance between the DSSC surface and the Halogen lamp was set at 30 cm (1 sun point) as shown in the Figure 3.6. Black masks were used to cover the cells by fitting them around the active area of the cells before measurements were commenced.

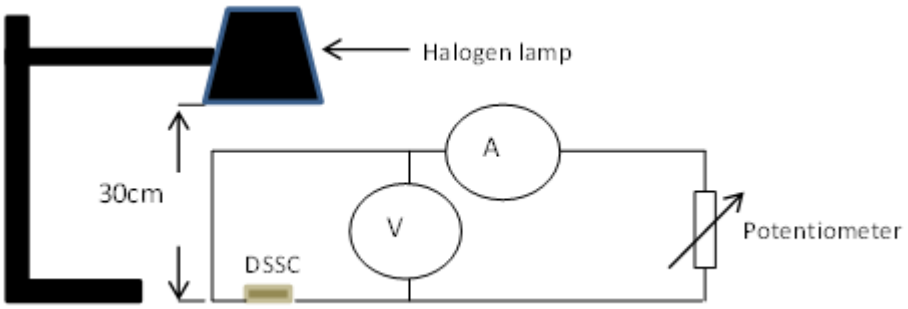

Figure 3.6: A model showing the setup of obtaining the I-V measurements of a DSSC.

The I-V characteristics were obtained by applying an external bias on the cells in a dark room to avoid stray light. The PV parameters V_{OC}, I_{SC} and FF were extracted from the I-V curve and used to determine the PCE of the DSSCs and DSSMs.

3.11 Characterization Softwares

3.11.1 Imagej 1.45v

Imagej 1.48v, java-based image processing program, was used as a tool for the analysis of optical images. Basically, the software was useful in obtaining plot profiles and histograms which are two 2D graphs of pixel intensities along selected cross-section lines on the optical images. The profiles obtained revealed the contrast variations on the optical images associated with topographical variation on the surface of the samples. The pixel intensities were interpreted in terms of heights of islands from a reference background point. The pixel intensities were converted into position in microns by obtaining them along a length or width of the optical image measured from an edge. The dimensions of the actual samples were obtained using the calibrations on the stage of the microscope (Alexander *et al.,* 2015).

For more accurate pixel intensities, rectangular selection on the optical images was carried out where the gray scale values obtained were averaged. In this work, plot

profiles and histograms were extracted from optical images of TiO_2 samples annealed at different annealing rates and at magnifications 16X, 100X and 260X. The data was then plotted using *Origin-pro version 8.0* software and analyzed in terms of surface area, particle size and number of count of the observed islands on the TiO_2 surface which depicted surface morphology of the samples. The software was also used for other functions such as deriving Root Mean Square (RMS) surface roughness and enhancing image contrast (Ying *et al.,* 2012).

3.11.2 Origin Pro Version 8.5

The data values obtained from all the characterization techniques was analyzed by plotting graphs using *Origin-pro 8.0* software.

3.11.3 Crystalsim

The *Crystalsim* (freeware software) is a X-ray diffraction *hkl* index simulation computer program used to simulate XRD $\{hkl\}$ data. It automatically generates the index $\{hkl\}$ planes for any given 2θ XRD data for any crystal system. That is, cubic, tetragonal, hexagonal, rhombohedral orthorhombic monoclinic and triclinic crystal systems. In this work, using *Crystalsim* program, the tetragonal system for anatase phase of TiO_2 was selected and the suitable crystalline lattice parameters a and c ($a = b \neq c$), interfacial angles $\alpha = \beta = \gamma = 90^0$, 2θ and the wavelength of the X-rays used. Upon running, the program was able to index Miller indices $\{hkl\}$ planes and simulate the theoretical interplanar *d*-spacing.

3.11.4 SCOUT 2.4

The approximation of the optical band gap was achieved using SCOUT 2.4 Software by simulating the optical response of the films (http://www.mtheiss.com). This was achieved by first inputting the transmittance data as the software is pre-configured with

optical constants of solid state properties of thin films. Optical model was used to generate optical data for comparison with experimental data. The simulated numerical data was used to approximate the optical band gap by applying the O'Leary-Johnson-Lim (OJL) inter-band transition model. The SCOUT's simulation band gap spectra were then compared with the Tauc's extrapolation method (Njeru, 2017).

.

CHAPTER FOUR

RESULTS AND DISCUSSIONS

4.1 Background

The chapter entails results and discussion of optical microscopy, UV-Vis, XRD and surface potential measurements, and analysis. Models relating the optical properties, surface morphology, crystallite structure and surface potential of the TiO_2 films are also developed and discussed. Finally, I-V characteristics of the DSSCs and DSSMs fabricated using the optimized TiO_2 films as working electrodes are analyzed and discussed.

4.2 Optical Microscopy

4.2.1 Surface Roughness/Morphology

In order to examine the influence of annealing on the films' surface topology, optical images of four samples prepared under same conditions and subjected to different annealing rates as described in chapter 3. Figure 4.1 indicates two-dimensional (2D) optical images of films subjected to annealing of 1 ^{o}C per minute and taken at magnifications 16, 100 and 260X. Surface topographies are revealed in terms of variation in contrast regions. Evidently, surface topographies become more vivid at 260X magnification.

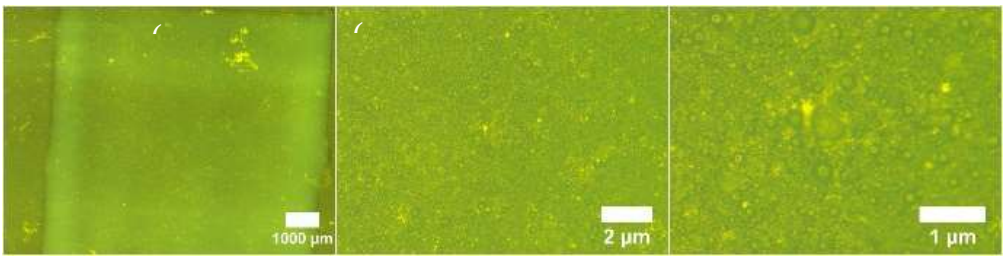

Figure 4.1: Optical contrast of a TiO_2 film annealed at 1 ºC/min observed at magnifications (a) 16, (b) 100 and (c) 260X.

Line profile technique was employed in the surface roughness analysis of the optical images. First, using *imagej* software, lines were drawn at selected positions spanning whole area of the image. Subsequently, average heights in terms of gray scale values were obtained (Figure 4.2). Average heights data was taken on four more films prepared under similar conditions.

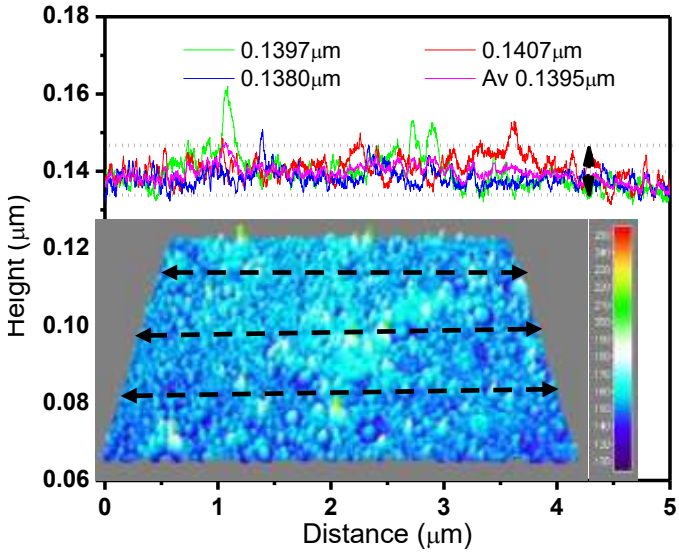

Figure 4.2: Line profiles showing topographical heights TiO_2 film annealed at 1ºC/Min. (Inset- 3D image with lines along which profiles were obtained).

Analysis of Figure 4.2 indicated average heights of $0.1395 \pm 0.0013 \mu m$. Average heights results for samples prepared and conditioned differently were tabulated in Table 4.1. Variation in surface roughness is observed. This indicates a strong dependence of surface roughness on annealing rate, with the lowest value of $\pm 0.0033\ \mu m$ recorded for the 1-step annealing scheme.

Table 4.1: Topographical values for TiO_2 films conditions differently

Annealing rate (^oC/Min)	**Observed Profile Heights (μm)**		
	Maximum	**Minimum**	**Average**
1 ^oC/Min	0.1356	0.1325	0.1337 ± 0.0015
2 ^oC/Min	0.1407	0.1380	0.1395 ± 0.0013
1-Step Annealing	0.1445	0.1421	0.1436 ± 0.0012
As-deposited	0.1259	0.1193	0.1247 ± 0.0033

To validate the line profile technique, a second method (histogram distribution) was employed. Here, line width or full width at half maximum (FWHM) values and mean heights were analysed and plotted (Figure 4.3). It is observed that the distribution models a normal Gaussian curve. The line widths are dependent on annealing conditions. The procedure was applied for all the samples analysed using line profile technique.

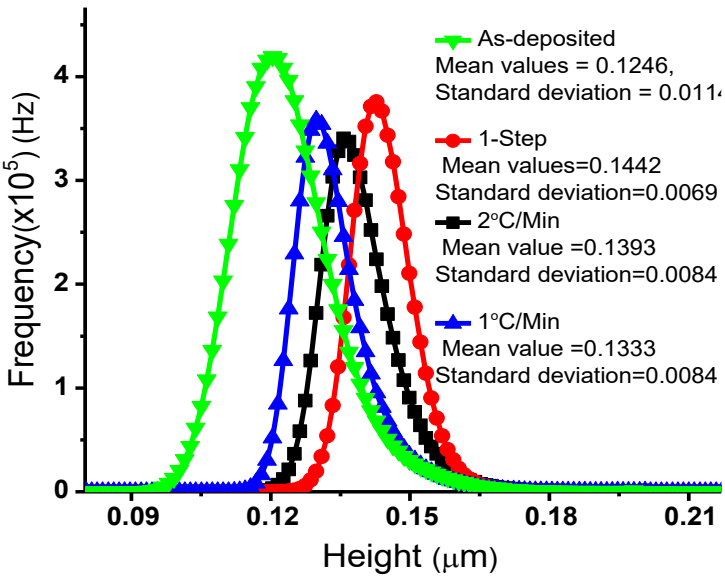

Figure 4.3: Histogram distributions of heights on the surface of TiO_2 samples conditioned differently.

From Figure 4.3, the heights were recorded as 0.1246 ± 0.0114, 0.1333 ± 0.0084, 0.1393 ± 0.0084 and $0.1442 \pm 0.0069\ \mu m$ for the *as*-deposited, 1 ^{o}C/min, 2 ^{o}C/min and 1-step annealed film, respectively. A significant difference in mean heights of the as-deposited and the annealed samples is noted and it indicates high density of contrast regions corresponding to surface roughness. A similar trend is also observed in the two analysis techniques (histogram distribution and line profile techniques) with a notable difference observed in the change in variations. Here, the line profiling technique exhibit larger variations compared to the histogram technique. The large variations in contrast are due to the few observed island along which the lines passes. For the histograms, the entire contrast region is well mapped leading to reduced error margins (standard deviations). In this regard, the measured heights in both cases indicate a changing topographical feature corresponding to surface roughness and depended on the thermal conditioning of the samples.

Comparison of island count, average size of islands and coverage (surface area of islands) on the film's surface with annealing rate was tabulated as shown in table 4.2.

Table 4.2: Comparison of count, average size and coverage with annealing rate

Annealing Rate (ºC/Min)	**Count**	**Mean Size (*um*)**	**% Area**
1 ºC/Min	7288	0.1947	9.09
2 ºC/Min	9634	0.1684	4.14
1-Step	26768	0.1262	7.77
As-deposited	29118	0.1037	12.31

The data in Table 4.2 was then plotted as shown in Figure 4.4.

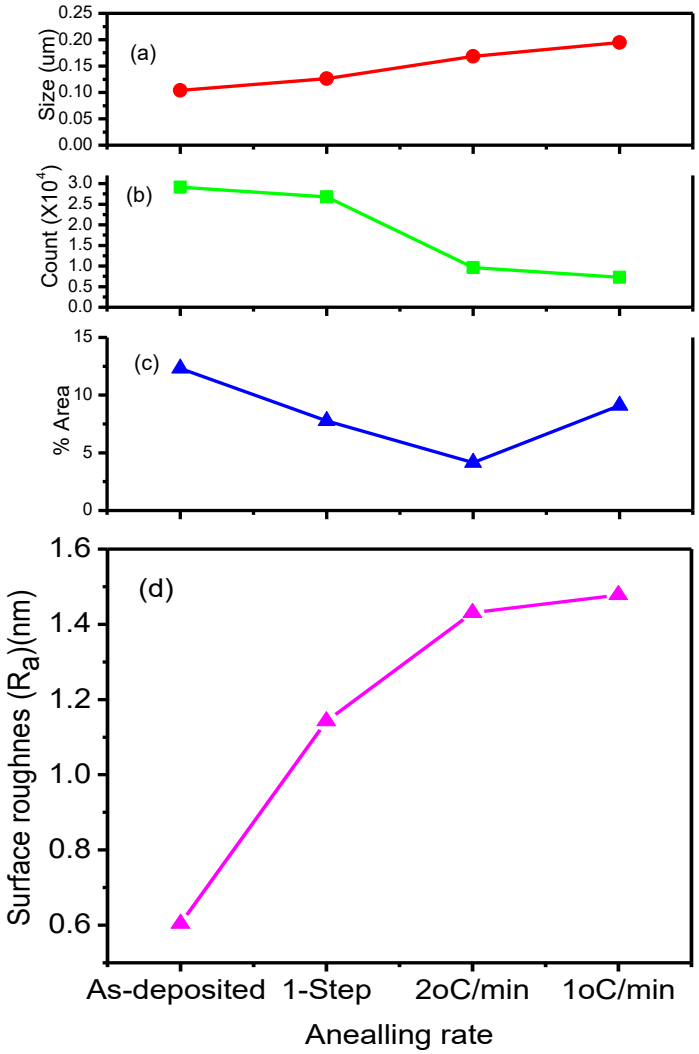

Figure 4.4: Variation of (a) Average size of topographical features (islands), (b) Count or number of islands, (c) Coverage (% area) and (d) Surface roughness of TiO_2 thin films with annealing rate

From Figure 4.4 (a), it is noted that the 1 ^oC/Min has the largest size ($0.1947\ \mu m$) whereas the as-deposited film has the lowest size ($0.1037\ \mu m$). In Figure 4.4(b), the as-deposited film has the highest count (29,118) of the high contrast regions. In Figure 4.4(c), the as-deposited film has the highest %Area (12.31%) while the 2 ^oC/min annealed film exhibit the lowest % Area of 4.14%. Therefore, it can be deduced that processing of TiO_2 thin films by 1^oC/Min provides a path to fabricating transparent films

with a good uniformity/homogeneity. Increasing the annealing rate (e.g at 2 ^{o}C/Min) lowers the homogeneity as the topographical features become less elongated. Except for the 1^{o}C/Min films, the other films indicate low uniformity (aggregates of nearly similar size). Figure 4.4 (d) represents the surface roughness (R_a) obtained using *Imagej* plugin software. The R_a values are 1.4783, 1.4301, 1.1425 and 0.6044 *um* for 1^{o}C/Min, 2 ^{o}C/Min, 1-step and as-deposited film, respectively.

Thus, TiO_2 films deposited by doctor-blade method result into surfaces with moderate roughness and can be improved by reducing the annealing rate. The average size of topographical features results analysed using *imagej* software were correlated mean height corresponding to surface roughness for samples annealed at different annealing rates and tabulated as shown in Table 4.3. Each data is an average of five measurements.

Table 4.3: Mean heights (surface roughness) and sizes of the islands on the TiO_2 films surface

Annealing Rate	Height (μm)	Size (μm)
1 ^{o}C/min	0.1333 ± 0.0084	0.1947 ± 0.0078
2 ^{o}C/min	0.1393 ± 0.0084	0.1684 ± 0.0103
1-step	0.1442 ± 0.0069	0.1262 ± 0.0053
As-deposited	0.1246 ± 0.0114	0.1037 ± 0.0054

Notably, the as-deposited sample reveals the smallest mean height while the 1-step annealed film reveals the largest mean height value. However, the as-deposited film exhibits the largest variation, an indication of the lowest homogeneity. A plot indicating mean heights and mean sizes of the films' topographical features is shown in Figure 4.5. The trend is consistent in the variations of the two parameters indicates a strong dependency of surface morphology on annealing temperature (Muaz *et al.*, 2016).

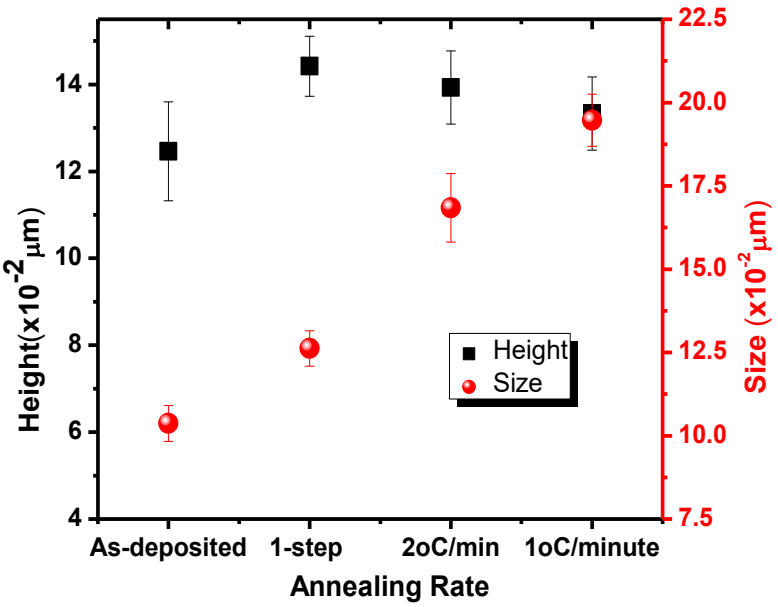

Figure 4.5: Correlation between mean heights and sizes of the topographical features with annealing rate

The lowest mean height and largest size of the topographical features is observed in the at 1 ^{o}C/min annealed sample. On the contrary, the least island size 0.1262 *um* is observed in the as-deposited sample. A low mean height of 0.1246 *um* is also observed in the sample. Here, the mean heights of the islands correspond to the surface roughness and, therefore, reducing the annealing rate leads to improved surface homogeneity. This is envisioned as elongation of the topographical features occurs. Consequently, the surface of the film becomes rougher. In other words, annealing the films at low annealing rates means providing the molecules of the film with sufficient energy for them to coalesce. According to Wibowo *et al.* (2017), more annealing time improves the quality of the film as far as photocatalytic activity is concerned. In the same light Muaz *et al.* (2016) reported that low annealing rates results into reduced charge trap sites including grain boundaries and other crystal defects. The observed relation (Figure 4.5)

indicates that grain size is proportional to surface roughness as reported by Norhafiezah *et al*. (2014). The amorphous state of the 1-step annealed film is responsible for the observed low surface roughness. The film began to crystallize into rutile phase at 400ºC. The phenomenon is consistent with results by Ogawa *et al.* (2008). Furthermore, low annealing rates improves the molecules' mobility resulting to particle crystallization (Tian *et al.*, 2006). The activated mobility leads to more roughness.

4.3 Optical Parameters of TiO_2 thin films

4.3.1 Transmittance

Figure 4.6 shows the transmittance spectra obtained using UV-Vis spectrophotometry. The films exhibit significant transparency with transmittance of up to 82.5% in the spectral range ($500-800\ nm$) and a sharp decrease in the UV region due to losses in the form of band transitions.

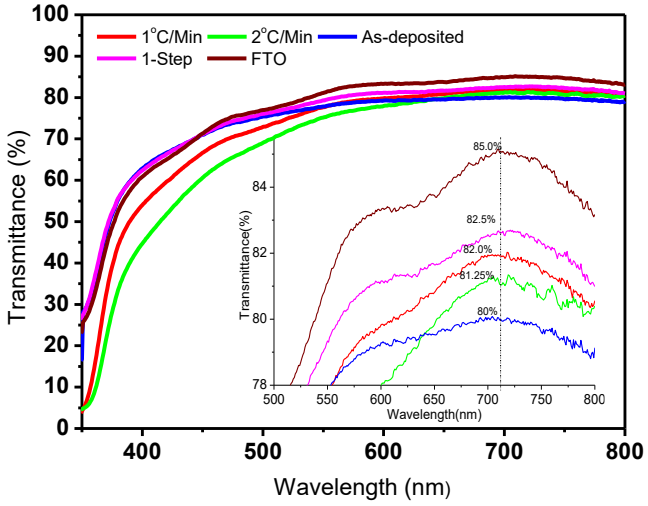

Figure 4.6: Optical transmittance spectra versus wavelength. (Inset): Zoomed transmittance curves in the spectral range (500-800*nm*).

Notably, Figure 4.6 revealed increase in transmittance maxima as well as shifting of absorption edges to a shorter wavelength as the annealing rate is lowered, say from 2^{o}C/Min to 1 ^{o}C/Min. All the TiO_2 thin films exhibit peak transparency at 712.5 *nm* wavelength. This is around the wavelength at which the optical thickness corresponds to half wave and shows maximum transmittance (Sönmezoğlu *et al.,* 2012). Similar results were observed by Sönmezoğlu *et al.* (2012) and were attributed to the absorption posed by the creation of oxygen vacancies as well as the transmittance edge shift to longer wavelength mainly due to the scattering of film surface, absorption and increase in density of the film. That is, when the films are annealed at lower rate, the oxygen of TiO_2 is released to the environment resulting into oxygen vacancies formation. Due to this, the superfluous free electrons are combined to the sites of oxygen vacancies to keep electric neutrality and hence TiO_2 films are considered to be n-type semiconductors (Tian *et al.,* 2006).

4.3.2 Absorption and Extinction Coefficients

The optical absorption coefficient (α) and the extinction coefficient (K_{ex}) for the films were obtained from the transmittance spectra as shown in Equations 2.38 and 2.39, respectively (Mathews *et al.,* 2009; Zhao *et al.,* 2011). The absorption coefficient and the extinction coefficient were plotted as shown in Figure 4.7.

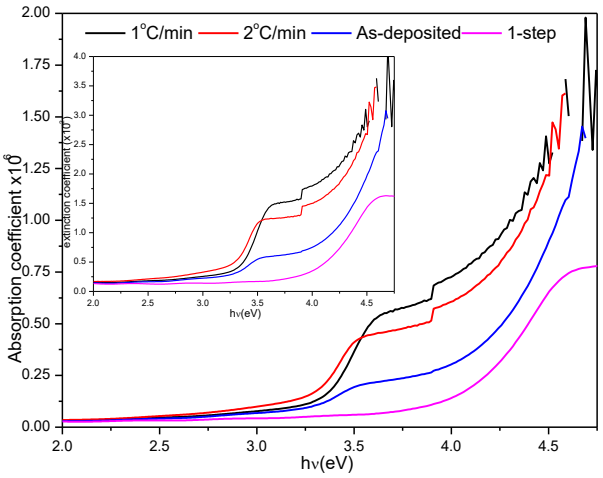

Figure 4.7: Plot of absorption coefficient against wavelength. (Inset): Extinction coefficient against photon energy.

Both the extinction coefficient and the absorption coefficient are diminished in the visible spectral region and increases sharply in the UV region ($3.5-5\ eV$). From Figure 4.7, in the UV region, it is observed that the absorption coefficient and the extinction coefficient are highest in the 1 ^{o}C/Min and lowest in the 1-step annealed films. The extinction coefficient conforms well to the absorption coefficient as it indicates the fraction of light lost due to absorption and scattering per unit distance of the film (Sharma & Katyal, 2007). The high absorption coefficient observed in the 1^{o}C/Min annealed film indicates that the lower the annealing rate, the higher the concentration of free carriers. That is, it is the free carrier transition in certain energy bands that causes absorption in the films (Sharma & Katyal, 2007; Tian *et al.*, 2006). Furthermore, both scattering and absorption loss may have increased with decrease in annealing rate due to surface roughness increase as well as the absence of oxygen in the TiO_2 films (Tian *et al.*, 2006; Beckmann & Spizzichino, 1987).

4.3.2 Refractive Index

The refractive indices were obtained from the transmittance spectra based on the Swanepoel method (Swanepoel, 1983). The refractive index (n) in the spectral region of medium and weak absorption was calculated based on Equations 2.40 and 2.41. A plot of the refractive index against wavelength, shown in Figure 4.8, reveals that the refractive index of the films is high in the UV region (region of strong absorption) and reduces with increasing wavelength (region of weak and medium absorption). This trend is noted to be consistent with Cauchy's-Model (Ali *et al.,* 2015). The *as*-deposited films had the lowest refractive index of 2.325 at 550 *nm* spectral range which improved to 2.55 upon annealing. That is, films annealed at 1°C/Min had generally the highest refractive index in the visible spectra range.

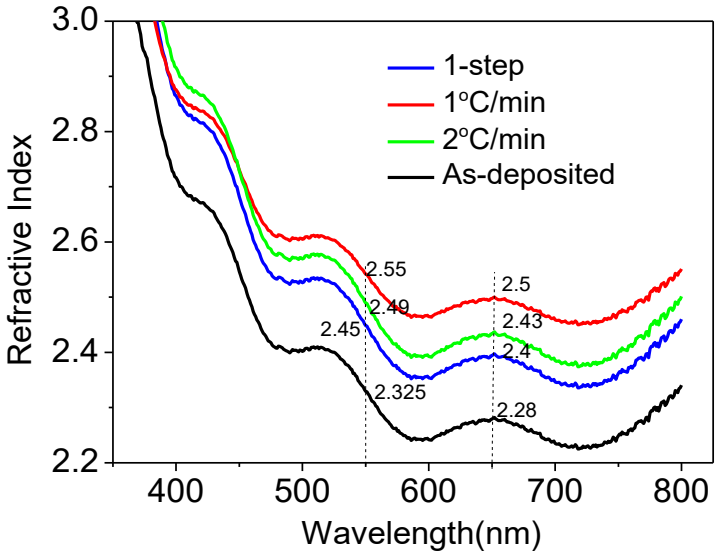

Figure 4.8: Refractive Indices spectra as function of wavelength

The increase in refractive index with decrease in annealing rate is attributed to the increase in packing density resulting in improved crystallinity of the films (Sönmezoğlu *et al.,* 2012). Similar results were observed by Sunkara & Misra (2008) and Ravindra *et*

al. (2007) and reported that annealing of the films at low annealing rate results to reduced porosity which consequently leads to densification of the films.

4.3.3 Porosity

The porosity (P_o) of the TiO_2 films was determined using Equation 2.42 (Mathews *et al.*, 2009; El-Nahass *et al.*, 2012; El-Nahass *et al.*, 2016). Figures 4.9(a), (b) and (c) shows a plot of porosity as computed from refractive index at $500\ nm$ spectral wavelength, a plot of refractive index taken at $500\ nm$ spectral wavelength and the inverse relation between the two parameters, respectively.

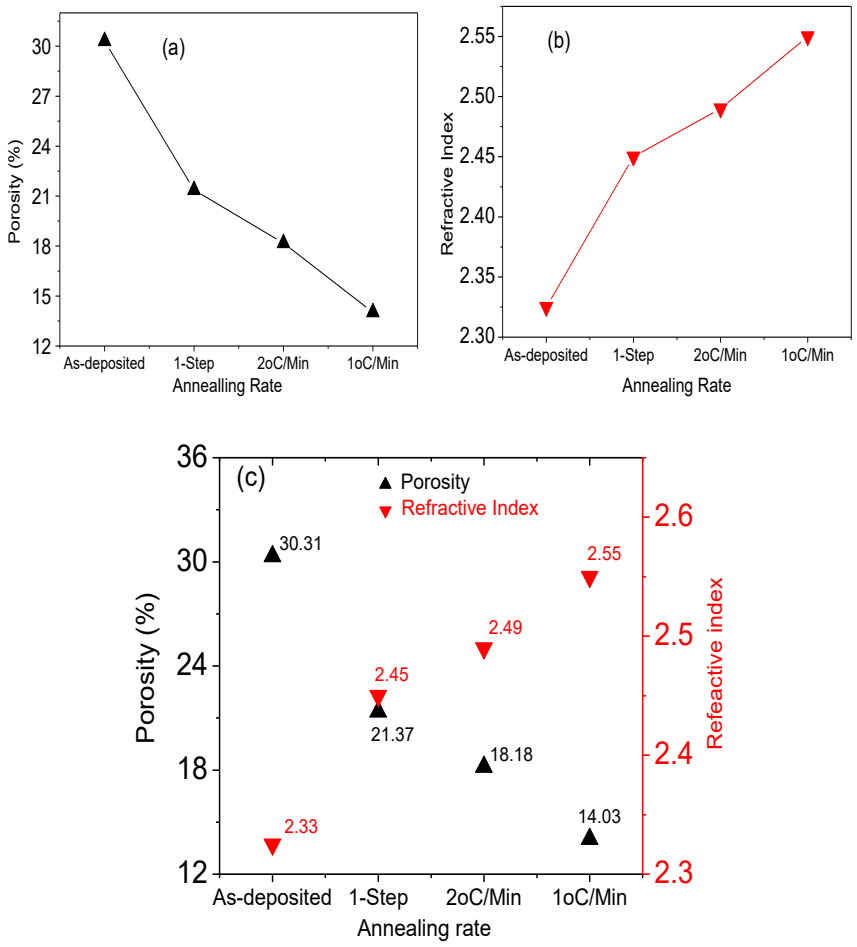

Figure 4.9: (a) A plot of Porosity (b) Refractive index and (c) Correlation between porosity and refractive index computed at $500\ nm$ **spectral wavelength versus annealing rate**

Films annealed at 1 ^{o}C/Min have the lowest porosity of 14.03% and the largest refractive index of 2.55. The contrast is observed in the *as*-deposited films as it exhibits the highest porosity of 30.31% and the lowest refractive index of 2.33. This phenomenon is associated with the fact low annealing rates promotes a reduction in pore size as grains' compaction and densification. Hence, the TiO_2 film becomes more densely packed leading to high refractive index and reduced porosity (Bartic *et al.*, 2013; Ahn, *et al.*, 2003). Annealing at 1 ^{o}C/Min leads, therefore, to an attractive state of the films for their photocatalytic application.

4.3.4 Optical Band Gap

The optical band gap (E_g) was calculated using the Tauc Equation 2.43, (Zhao *et al.*, 2011). Since indirect transition dominates in nanostructured TiO_2, $\gamma = 1/2$ have been adopted (Sönmezoğlu, *et al.*, 2012). The optical band gap was determined from the extrapolation of the linear plots of $(\alpha h\upsilon)^{1/2}$ versus $h\upsilon$ at $\alpha = 0$, as shown in Figure 4.10. The band gap was found to decrease with annealing rate, 3.88, 3.72, 3.33, and 3.13eV for the *as*-deposited, 1-step, 2 ^{o}C/Min and 1 ^{o}C/Min annealed films, respectively.

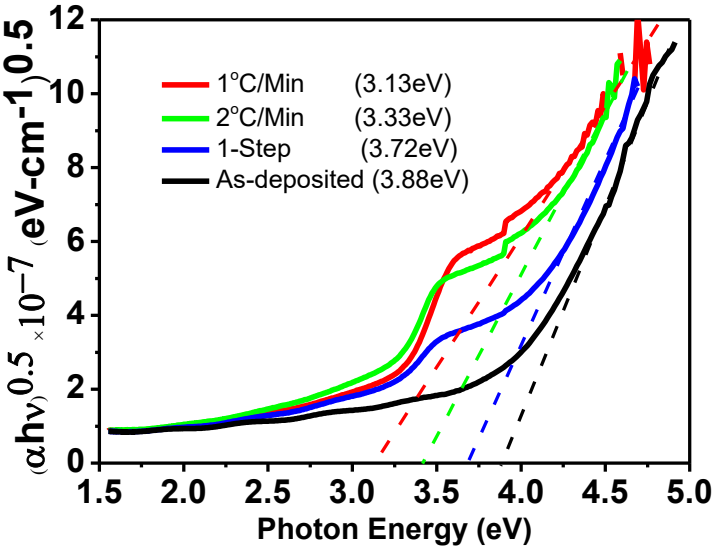

Figure 4.10: Optical energy band gap for TiO_2 films as a function of photon energy

The decrease in optical band gap with annealing rate is attributed to the lowering of interatomic spacing, which is associated with a decrease in the amplitude of atomic oscillations around their equilibrium positions (Sönmezoğlu *et al.,* 2012; Sunkara & Misra 2008). This enhanced crystallization as small crystallites agglomerate into large crystals (Salem & Selim 2001; Yarmand & Sadrnezhaad, 2010; Bartic *et al.,* 2013). Low annealing rate enhances the formation of oxygen vacancies, and as a result the electron concentration increases in the energy gap region. This leads to some of the localized electronic states approaching the conduction band to be at minimum. Thus, at lower annealing rate, anatase TiO_2 behaves as *n*-type semiconductor due to reduced optical band gap (El-Nahass *et al.,* 2016). To complement the experimental data, the band gap was simulated using SCOUT software based on OJL model. A near correlation was arrived at, with only a deviation of 0.12 eV and 0.03 eV recorded for the 1 ^oC/Min and 2 ^oC/Min annealing, respectively (Figure 4.11).

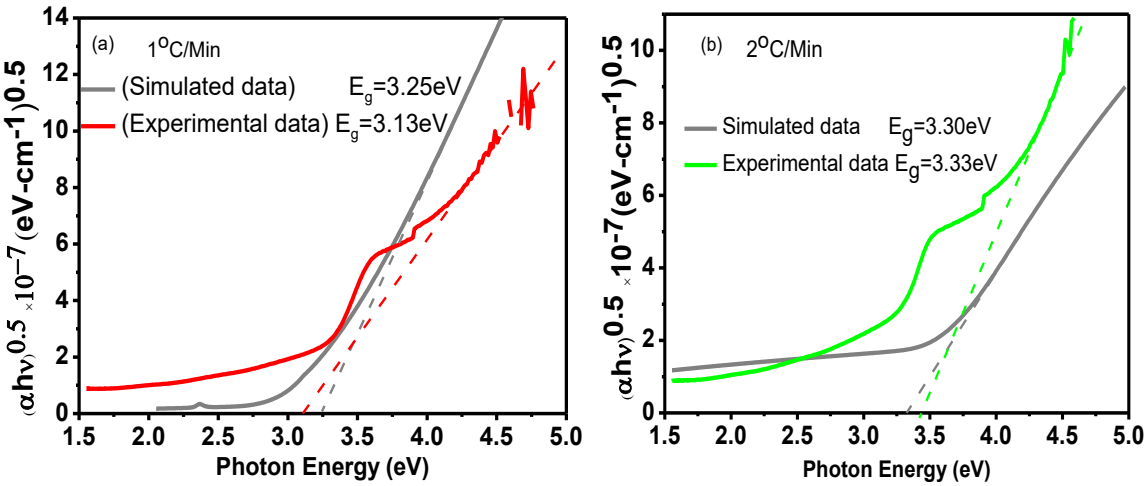

Figure 4.11: Comparison of the measured and simulated data using SCOUT for: (a) 1°C/Min and (b) 2 °C/Min TiO_2 thin films.

The experimental band gap shows a good approximation to the theoretical values.

4.3.5 Dielectric Constant

The real (ε_r) and imaginary dielectric constants (ε_i) for the films were calculated based on the complex refractive index as shown in Equations 2.44 (Goswami, 2005).

The variation of ε_r and ε_i with wavelength are shown in Figure 4.12.

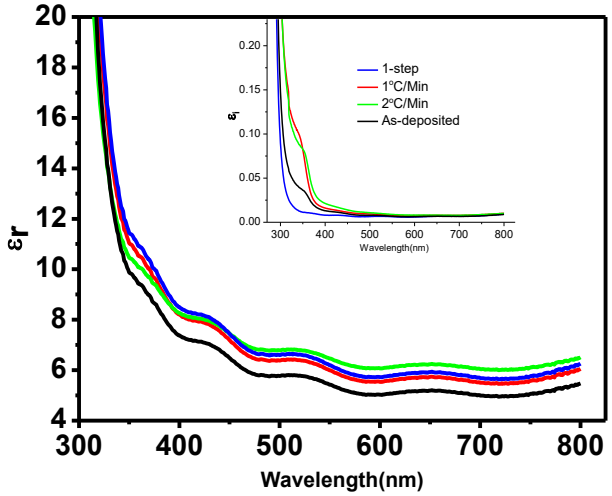

Figure 4.12: Dependence of real dielectric constant (ε_r) on wavelength. Inset: Imaginary dielectric constant (ε_i) versus wavelength.

Both ε_r and ε_i decrease sharply at the absorption edge. That is, dielectric constant is dependent on frequency, as it decreases with decrease in frequency. In the lower energy region, the ε_r is highest for the annealed films and lowest for the as-deposited film. That is, annealing improves the dielectric property of the films as high ε_r indicates the material's ability to store energy or become polarized (Wypych *et al.*, 2014). Therefore, the films' dielectric response is complex and is composed of molecular levels and space charge polarization contributions. The amorphous (as-deposited) sample shows the lowest polarization due to energy dissipations on the grain boundaries. The observed dielectric relaxation in the annealed films may have been caused by the delay in molecular polarization during the film's response to the changing electromagnetic field (Juma *et al.*, 2016). The ε_i approximates to zero at lower frequencies, indicating that the films becomes lossless at these frequencies (Wypych *et al.*, 2014; Wang *et al.*, 2006).

The loss tangent ($\tan\delta$) was determined in order to reveal the extent to which the thin films absorb the electromagnetic (EM) radiation (El-Nahass *et al.*, 2016) (Equation 2.45). The loss tangent, indicate the magnitude of the ratio of conduction current density J_C to the displacement current density J_D in a lossy medium (Equation 2.46) was used to described the optical response of the TiO_2 films. A plot of $\tan\delta$ with wavelength is shown in Figure 4.13.

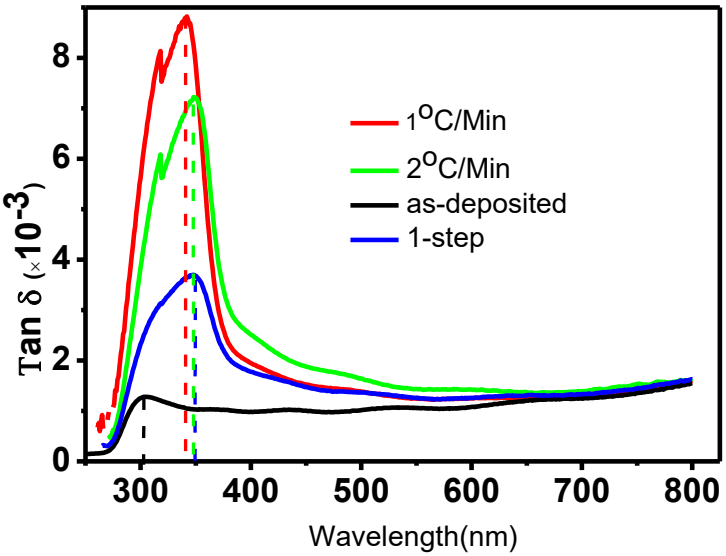

Figure 4.13: Variation of Loss Tangent with wavelength.

The imaginary dielectric constant (ε_i decays rapidly than the ε_r in the UV region as indicated by high $\tan\delta$ and diminishes sharply at the onset of the visible region. This is attributed to reduced absorption in the visible regime. The films annealed at 1°C/Min have the highest $\tan\delta$ in the UV region, an indication of the highest changes in the free carrier's transitions in certain energy band causing absorption. Hence, loss tangent was enhanced resulting to high absorption of EM field (El-Nahass *et al.*, 2016). The loss tangent is also a measure of how lossy the films (medium) became upon annealing and

depends on frequency. Figure 4.13 indicates that the as-deposited film is near-lossless medium or a perfect dielectric medium as its $\tan\delta$ vanishes in the UV regime. That is, $\sigma << \omega\xi$. Hence, by annealing the films, a surge in the loss tangent is observed in the UV regime depicting improvement in conductivity as $\sigma >> \omega\xi$.

Figure 4.13 also indicates variation in the intrinsic impedance of the TiO_2 films with annealing rate. The as-deposited films exhibit the highest intrinsic impedance, as indicated by a small peak in loss tangent observed in the UV region of EM field in figure 4.13. On the contrary, the annealed films reveal a reduction in intrinsic impedance, as indicated by the upsurge in loss tangent peaks in the Figure 4.13. That is, annealing reduces the dielectric property of the films by reducing their penetration depth or skin depth as $\sigma >> \omega\xi$. Moreover, the high loss tangent observed in the annealed films is attributed to intrinsic dielectric losses in the crystalline film, and is dependent on the crystal structure. The high loss tangent indicates the significant interaction of the phonon system with the applied electromagnetic field (Sebastian, 2010). The Electromagnetic field alters the equilibrium of the phonon system resulting to dielectric relaxation (indicated by the red-shift in loss tangent peaks in Figure 4.13), and subsequent energy dissipation (Gurevich & Tagantsev, 1991). Here, the variation in loss tangent with annealing rates indicates that the intrinsic losses depend on crystal symmetry and the applied electromagnetic field. The low loss tangent observed in the amorphous film is associated with extrinsic losses. The extrinsic losses are associated with film's defects such as microstructural defects, grain boundaries and dislocations (Gurevich & Tagantsev, 1991).

4.3.6 Optical Conductivity

Optical conductivity (σ) was determined using Equation 2.47.

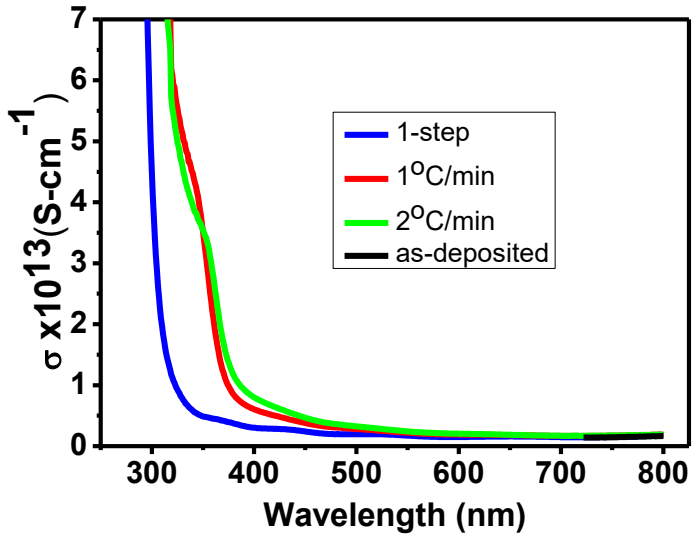

Figure 4.14: Optical conductivity spectra as a function of wavelength.

Figure 4.14 shows that the optical conductivity is high in the UV spectral region and decreases drastically in the visible region for the annealed films. The phenomenon indicates that electrons are excited by the high photon energy in the UV region. Further, the films annealed at 1 ^{o}C/Min and 2 ^{o}C/Min exhibit a wider spectral range (250-375 nm) of electron excitation as compared with the 1-step annealed film (250-325 nm), a behavior attributed to changes in band gap. It is also observed that the *as*-deposited film only exhibit optical response in the 712.5-800 nm spectral range due to the lack of delocalized carriers in its large band gap as well as its disordered state (El-Nahass *et al.*, 2016). The optical conductivity decreased corresponding to the absorption edge and band gap of the films (El-Nahass *et al.*, 2016).

4.3.7 Surface and Volume Energy Losses

Energy loss functions, results from electron transition within solids of thin films. The Energy Loss (E_L) describes the energy absorbed (or energy lost by the free charge carriers) as they pass through the film. E_L has two components: Surface energy loss

(S_{EL}) and Volume or Bulk Energy Loss (V_{EL}). The two energy components are derived from ε_r and ε_i as shown in Equations 2.48 and 2.49. The S_{EL} describes the inelastic reflection of electrons at the flat surface of a solid without accounting for spatial dispersion (Figure 4.15). Both V_{EL} and S_{EL} follow the same trend as the loss tangent.

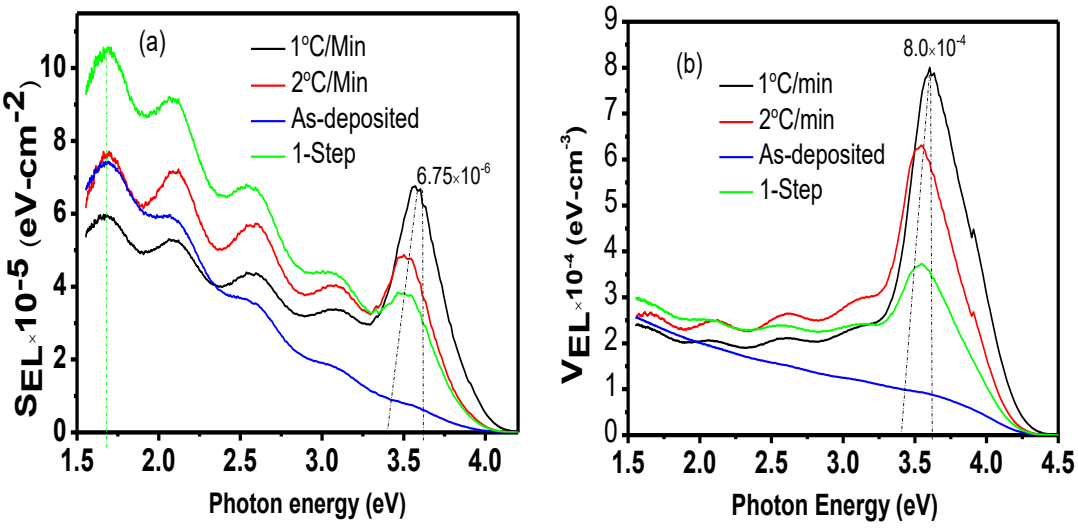

Figure 4.15: Frequency-dependency of Energy Loss Functions. (a) Surface Energy Loss Function and (b) Volume energy Loss

At the long-spectral wavelength limit, S_{EL} is insensitive to the surface structure and it does not describe the inelastic scattering with finite momentum transferred at the surface (Figure 4.15) (El-Nahass *et al.,* 2016; El-Nahass *et al.,* 2012; Park 2012). The energy loss by the free charge carriers when traversing through the bulk material is higher ($8.0\times10^{-4}\ eV-cm^{-3}$) for 1 °C/Min sample at $3.625\,eV$ Photon energy) than that traverse the surface ($6.75\times10^{-5}\ eV-cm^{-2}$) for the same sample at the same photon energy. This confirms that the energy loss occurred in the interior of the deposited films is attributed to the inter-band electronic transition (De Crescenzi & Piancastelli, 1996). That is, specific energy losses are experienced by the fast moving electrons due to the

excitation of plasma oscillations of conduction electrons, while passing through a medium (Pines & Bohm, 1952). A plot of S_{EL} and V_{EL} versus Photon Energy (Figure 4.16) shows that V_{EL} is greater than S_{EL} at all incident photon energies and both approaches zero at high photon energy.

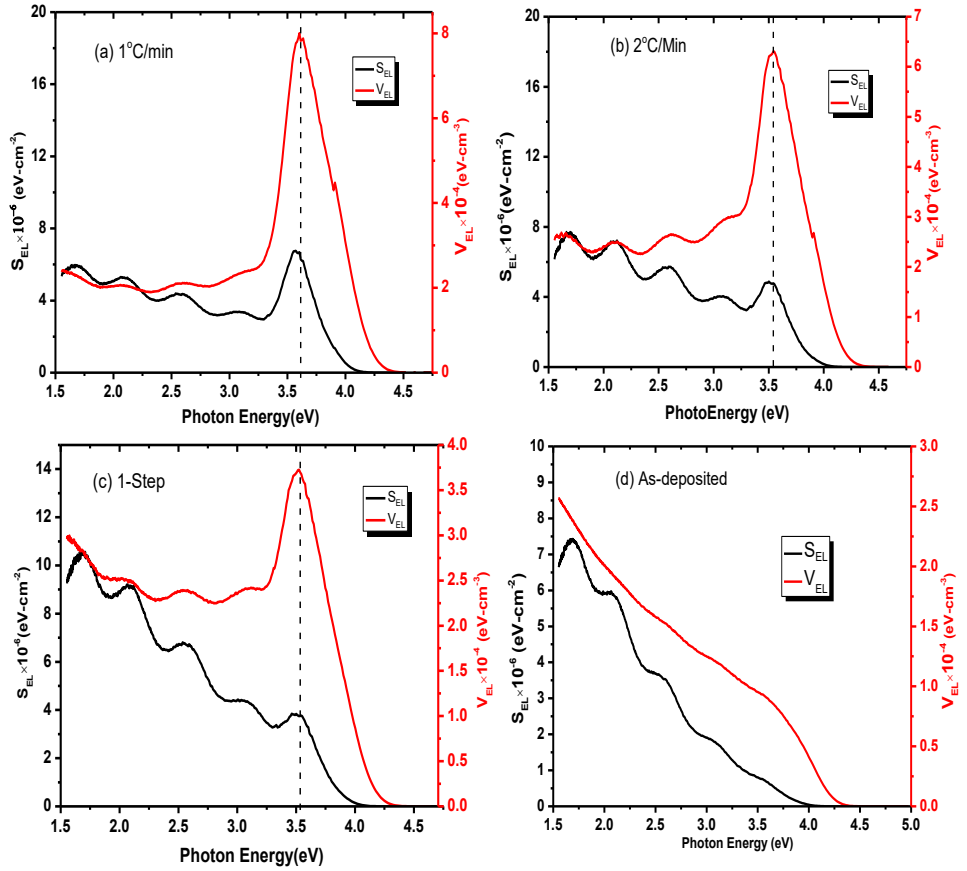

Figure 4.16: Comparison of S_{EL} and V_{EL} for TiO_2 thin films annealed at (a) 1ºC/Min, (b) 2 ºC/Min, (c) 1-Step annealing rates and (d) As-deposited

The trend in Figure 4.16 is associated with increased concentration of free charge carriers in the films. This is because Titania's compound is characteristic of anion omissions (Tian *et al.*, 2006). For example, at low annealing rates such as 1 ºC/Min and 2 ºC/Min, sufficient reaction time was available for sufficient concentration of oxygen vacancies $(V_{\ddot{O}})$ to occur (Equation 2.15). That is, stoichiometry misbalance occurs as

oxygen anions in the films dissociated into oxygen molecules (O_2) and free charge carriers (e^-) (Equations 2.14 and 2.15). The oxygen molecules are released to the environment leaving oxygen vacancies, which consequently leads to reduced film's porosity and bulk surface area (Tian *et al.* 2006). The S_{EL} occur as the superfluous free electrons undergo charge relaxation and traverse on the film surface (skin effect) while V_{EL} results from carrier transition, phenomena manifested as absorption upon the application of electric field. From the Figure 4.16, it is evident that while V_{EL} is dominant in all cases, the total energy loss is dependent on annealing rate. For example, S_{EL} is lowest at low annealing rate as much of the energy loss occurs in the form of V_{EL} which is associated with interband transitions. However, it is worth noting that the superfluous or trapped free electrons are combined to the oxygen vacancy sites to maintain electric neutrality. The dissociation process occurs as per the defective Equations 2.15 and 2.17. As the net Gibbs free energy (ΔG), which is dependent on annealing rate, approaches to zero, the oxygen vacancy concentration is maximum (Equation 2.18) (Tian *et al.* 2006). While the peaks observed in the annealed films indicate the highest energy loss, the lack of the peaks in the as-deposited films reveals the fact that free carriers are highly localized.

In addition, the V_{EL} may be explained in terms of inter-band carrier transition probability J_{VC} (Equation 2.50) which accounts for the dipole selection rules for the transitions (Badran *et al.,* 2012; French, 2000). In fact, the observation is consistent with a study conducted by Tian *et al.,* 2006 in which they reported that optical absorption coefficient of TiO_2 occurs sharply in the UV region due to inter-band transitions and is proportional to the concentration of free carriers and is given by Equation 2.51. The peaks in Figure 4.17 occurring at the near UV regime (3.5 *eV*) in the annealed samples indicate the highest energy loss, with the 1 ^oC/Min sample having the highest energy loss resulting from the highest changes in the free carrier's transitions in certain energy band that causes absorption (El-Nahass *et al.,* 2016). A plot of the inter-band transition probabilities is shown in Figure 4.17.

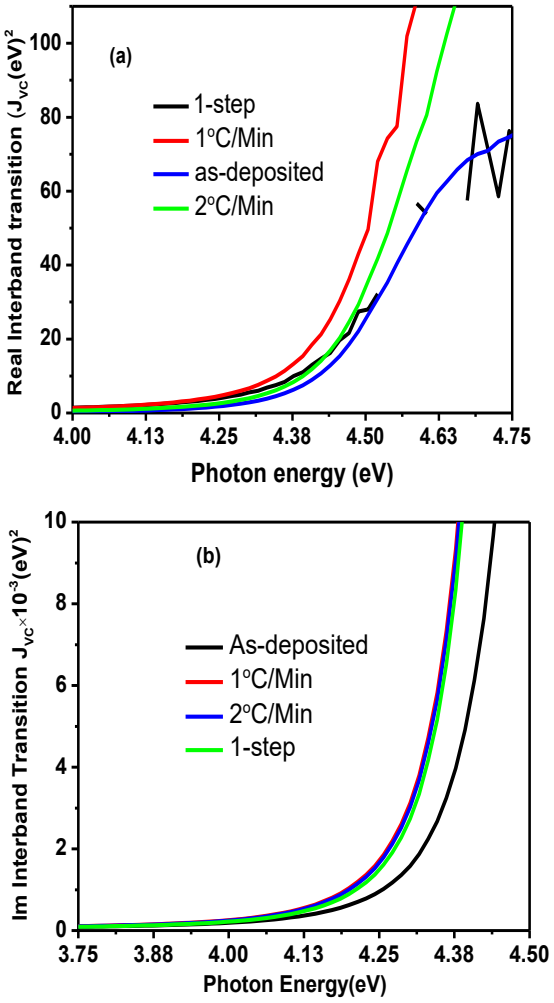

Figure 4.17: Inter-band transition (a) Real and (b) Imaginary inter-band transitions

The probability of interband transitions improves when the films are annealed at low rates (Figure 4.17 (a) and (b)). On the contrary, more energy is needed for an electron to jump from the VB to the CB in the as-deposited amorphous TiO_2 film. Figure 4.17 is consistent with the findings reported in Figure 4.10. That is, by lowering the annealing rate, the band gap reduces significantly from 3.77 to 3.13 *eV* as reconstruction of the crystal structure is favoured. This phenomenon occurs as the Fermi level (E_F) of the TiO_2 film is raised further above the intrinsic level of the semiconductor material.

In order to further understand the TiO_2 film's surface and bulk response in terms of crystallization and charge distribution, X-ray diffraction (XRD) and Scanning Kelvin probe Microscopy (SKPM) measurements techniques were employed.

4.4 Structural Measurements

4.4.1 X-ray diffraction measurements

The X-ray diffraction analysis was conducted because it is a crucial technique in the study of the phase composition and the structure of the films. The inter-planar spacing parameter (d – spacing) of the TiO_2 crystals was evaluated from the Bragg's Equation. The diffraction peaks in each diffraction pattern were observed and used to calculate the Miller indices and lattice spacing of the samples. The preferred orientations were determined using *Crystalsim* software (Howard *et al.,* 1991, Ullah *et al.,* 2013) and the data plotted as shown in Figure 4.18.

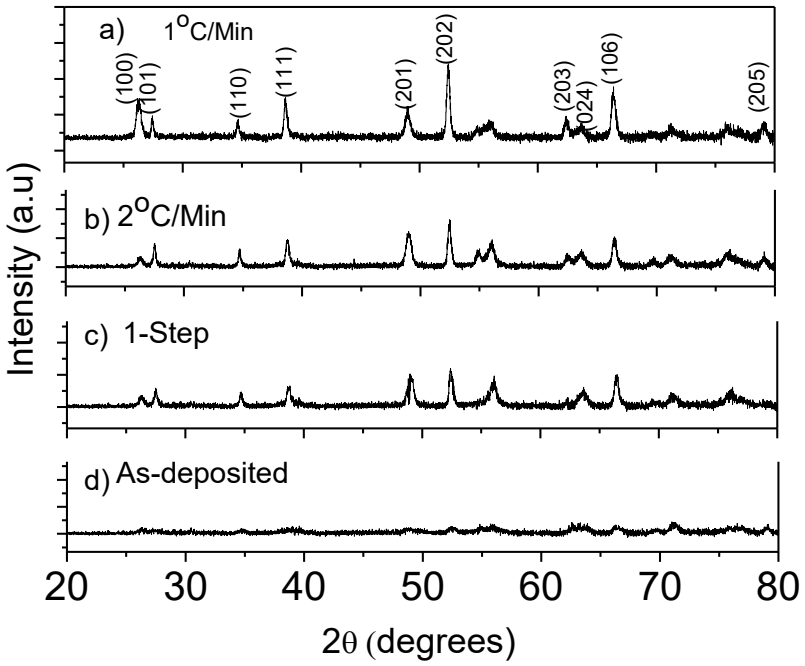

Figure 4.18: X-ray diffraction pattern of the TiO_2 films.

The observed peaks in Figure 4.18(a) correspond to {100}, {101}, {110}, {111}, {201}, {202}, {203}, {024}, {106} and {205} planes for various 2θ angles and depict the formation of well crystallized TiO_2 thin films indicated by sharp diffraction peaks (Govindasamy *et al.,* 2016). The diffraction pattern observed in the annealed films in Figure 4.18 (a), (b) and (c) indicates diffraction peaks at various Bragg's angles by planes of the anatase crystalline phase of TiO_2 annealed at different rates. In contrast, Figure 4.18 (d), exhibit rudimentary broad diffraction peaks corresponding to the as-deposited film. This is due to the film's amorphous nature (El-Nahass *et al.,* 2016). The average nanocrystalline size (L) was calculated using Scherrer formula (Deshmukh *et al.,* 2006). The FWHM of the XRD scans of TiO_2 films was obtained using *OriginPro 8.0* software and used to calculate the crystallite size. The average crystallite size was estimated at $24.9633, 24.3087$, and $21.8382\ nm$ for 1 ^oC/Min, 2 ^oC/Min and 1-step annealed films, respectively. The largest crystallite size observed in 1 ^oC/Min annealed film was attributed to the gradual agglomeration of small crystallites into large ones (Hou *et al.,* 2003; Saini *et al.,* 2007). The *as*-deposited film is characterized by short-range order and contain many defects that produce localized states (Saini *et al.,* 2007). Therefore, by reducing the annealing rate, the defects are reduced, hence the film crystallinity is improved and the crystallite size increases (El-Nahass *et al.,* 2016; El-Nahass *et al.,* 2012).

4.4.2 Correlation of Band Gap with Crystallite Size

The band gap and crystal size data was tabulated as shown in Table 4.4.

Table 4.4. A Table of Optical Band Gap and Crystal Size of the TiO_2 films annealed at different rates

Annealing	Band Gap (eV)	Band Gap (eV)	Crystallite Size

Rate	(Experimental)	(Simulated)	(*nm*)
1 ºC/Min	3.13	3.25	24.96
2 ºC/Min	3.33	3.30	24.31
1-step	3.72	3.25	21.84
***As*-deposited**	3.88	3.63	

The variation in optical band gap and crystal size shows variation with the annealing rate (Figure 4.19) and have a significant bearing on the band structure of TiO_2 thin films (Ravindra *et al.*, 2007).

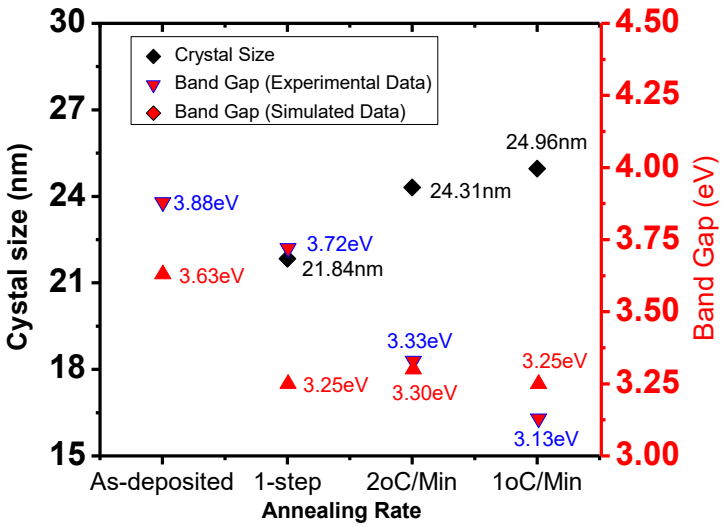

Figure 4.19: Variation of Optical Band Gap (from measurements and SCOUT simulation) and Crystal Size versus Annealing Rate.

From Figure 4.19, the crystal size increases with decrease in annealing rate (21.84, 24.3, and 24.96 *nm* for the 1-step, 2 ºC/Min and 1 ºC/Min, respectively). On the other hand, the Optical band gap decreases with decrease in Annealing rate (3.88, 3.72, 3.33 and

3.13 eV for the as-deposited, 1-step, 2 ^{o}C/Min and 1 ^{o}C/Min, respectively). The experimental and OJL model simulated data for band gap exhibits a good trend, an indication of a good approximation. The variations in both crystal size and optical band gap with annealing rate are attributed to densification which results in the observed decrease in porosity (Sönmezoğlu *et al.,* 2012; Tian *et al.,* 2006; El-Nahass *et al.,* 2016). For example, at 1 ^{o}C/Min, the pore size diminished by grain's compaction. The film became more densely packed and as a consequent, the refractive index increased and optical band gap decreased (Bartic *et al.,* 2013). This leads to a large surface area for the films, which, consequently, enhances their photocatalytic property (El-Nahass *et al.,* 2016).

4.5 Profiling of Surface Charge Distribution of TiO_2

4.5.1 Surface Potential/Workfunction

The physical principle of this technique is based on contact potentials (Mugo & Yuan, 2012; Jiang *et al.,* 2009). A Gold tip with workfunction $(-5200mV)$ was made to vibrate above each sample. The electrostatic interaction of the gold tip with the sample was minimized by the application of a bias voltage, which corresponds to contact potential difference (V_{CPD}) (Zerweck *et al.,* 2005; Nonnenmacher *et al.,* 1992). The contact potential difference revealed information about TiO_2 surface charging and was related to the sample work function (ϕ_{Sample}) by Equation 2.52 (Zerweck *et al.,* 2005). The samples were systematically scanned at ambient temperature and their color map (topographical map) constructed from area scan data as shown in Figure 3.20 a(i), b(i), c(i) and d(i). The corresponding scans were plotted as shown in Figure 4.20 a(ii), b(ii), c(ii), and d(ii) for the line scan and a(iii), b(iii), c(iii) and d(iii) for the point scan. For the Point scan, each data point consists of 8 measurements with fluctuations given as error bars (Figure 4.20).

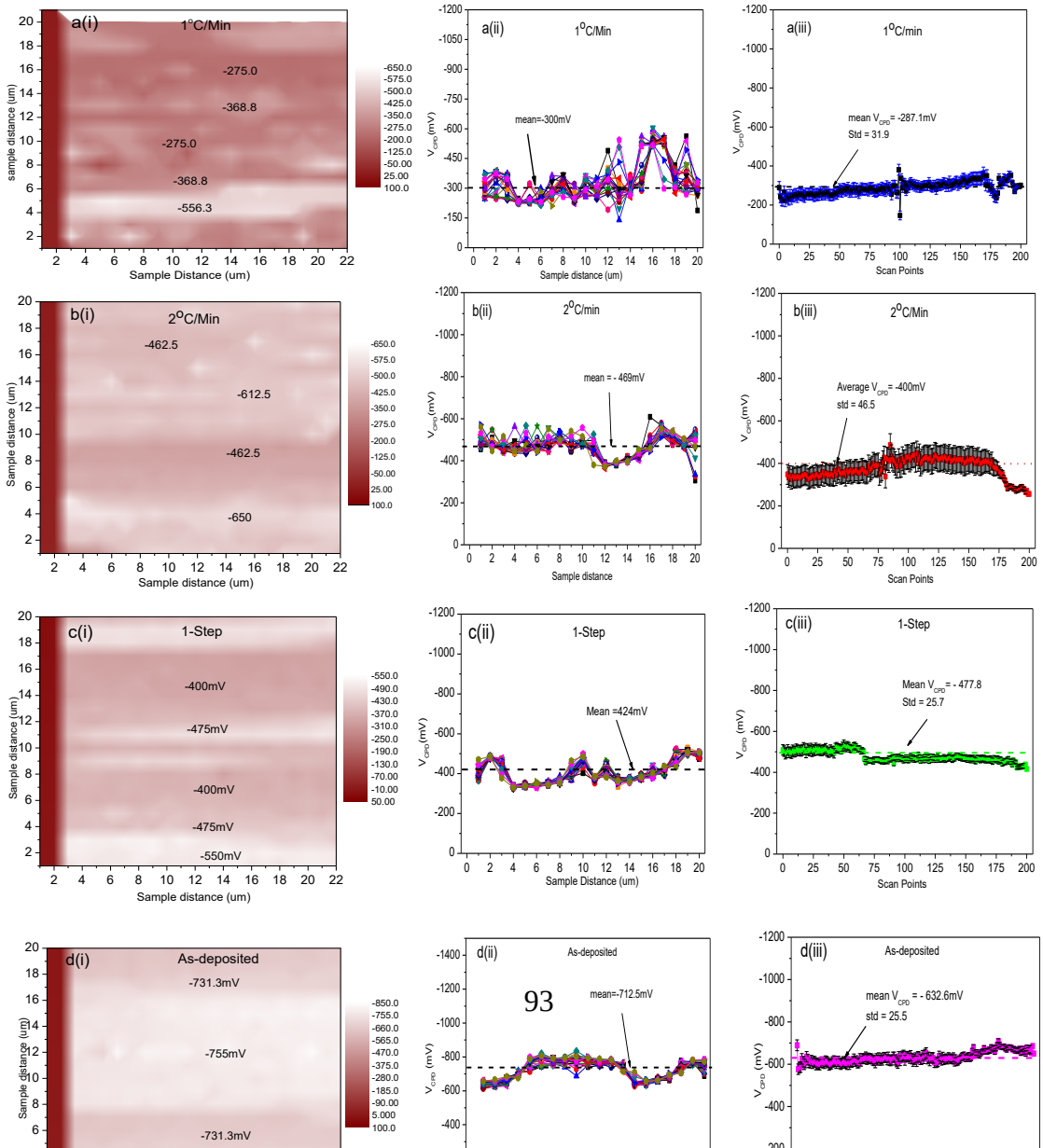
a(i)
1°C/Min
-275.0
-368.8
-275.0
-368.8
-556.3
sample distance (um)
Sample Distance (um)
a(ii)
1°C/Min
mean=-300mV
Sample distance (um)
a(iii)
1°C/min
mean V_CPD = -287.1mV
Std = 31.9
Scan Points
b(i)
2°C/Min
-462.5
-612.5
-462.5
-650
Sample distance (um)
b(ii)
2°C/min
mean = - 469mV
Sample distance
b(iii)
2°C/Min
Average V_CPD = -400mV
std = 46.5
Scan Points
c(i)
1-Step
-400mV
-475mV
-400mV
-475mV
-550mV
Sample distance (um)
c(ii)
1-Step
Mean =424mV
Sample Distance (um)
c(iii)
1-Step
Mean V_CPD = - 477.8
Std = 25.7
Scan Points
d(i)
As-deposited
-731.3mV
-755mV
-731.3mV
Sample distance (um)
d(ii)
As-deposited
93
mean=-712.5mV
d(iii)
As-deposited
mean V_CPD = - 632.6mV
std = 25.5

Figure 4.20: Contour/Topographical maps (first column), Area scan (second column) and point scan (third column) for TiO_2 thin films annealing at (a) 1 ºC/Min, (b) 2ºC/Min, (c) 1-Step annealing rates and (d) As-deposited.

A notable difference was observed as the V_{CPD} fluctuated depending on annealing conditions of the samples depicting changes in surface charge distribution. For example, the line scans indicated V_{CPD} of -300, -469,-424, and -712 mV for 1 ºC/min, 2 ºC/Min, 1-step and as-deposited samples, respectively, while the point scan indicates V_{CPD} of -287.1, -375,-477.8, and -632.9 mV for 1 ºC/min, 2 ºC/Min, 1-step and as-deposited samples, respectively. The topographical map shows that the V_{CPD} decreased significantly at low annealing rates.

It is believed that the variation in surface potential resulted from different oxidation levels of the TiO_2 surface during annealing as oxygen-rich reconstructions induced negative charges to the surface. That is, more ions on the TiO_2 surface render it negative. This appears as an added dipole moment pointing into the surface. SKPM captures the effect as more negative potential drop across the surface (Kim *et al.,* 2015). Surface dipole dictates the amount of energy involved in electron transfer between the semiconductor and the vacuum, hence, it affects the overall workfunction of the material. Surface structure of materials is dependent on electric dipole. Surface dipole corresponds to the potential drop across the surface. Therefore, the recorded variation in V_{CPD} occurred as the surface underwent structural changes or deformations due to

annealing (Kim *et al.,* 2015). The change in the microscopic electrostatic potential ($\Delta V = V_{CPD}$) is expressed in Equation 2.24. A more negative value of ΔV is an indication of a greater barrier for the electrons to escape to the vacuum (Figure 4.20(d)) hence large work function of the material.

Surface oxidations also induce V_{CPD}. Surfaces with oxygen ions far away from the bulk display more negative ΔV (Kim *et al.,* 2015). While phantom force or induced dipole moments (to the chemical bond between the tip apex and surface atoms) may have contributed to the observed variation in V_{CPD}, i.e tunneling current may have flown between the Gold tip and the TiO_2 sample, the probability of tunneling depends on the atomic site. However, tunneling effect is excluded in this work because tunneling current measurements were not obtained during V_{CPD} measurements (Lang *et al.,* 1971).

The surface potential observed in Figure 4.20 may also be explained based on the Smoluchowski effect (Mugo & Yuan 2012; Smoluchowski, 1941). The Smoluchowski effect is the theory of the charge distribution at sharp contours such as steps. In light of this effect, at low annealing rates, an upward dipole moment may have been created at the steps due to the incomplete screening of positive ion cores by conduction electrons because the electronic density cannot follow the step configuration, locally reducing the V_{CPD} at the steps. Since the Smoluchowski effect depends on the step configuration, the degree of the upward dipole moment should be different for the atomically smooth surfaces such as (001) and (100), compared to the atomically rough surfaces such as (110), which is dominated by atomic ledges (Lang & Kohn, 1971). Hence the phenomenon observed in Figure 3.19 confirms the fact that, generally, the work function depends on the crystal faces and different surfaces (Lang & Kohn, 1971). The Smoluchowski-like dipole, the local dipole moments of surface atoms also exist on the surface, creating a local atomic dipole (Lang & Kohn, 1971). The surface potential at the steps may, therefore, be interpreted as a combination of the Smoluchowski-like dipole and the local atomic dipole (Kitamura & Iwatsuki, 1998). These effects may explain why the drop in V_{CPD} at the 1 ^{o}C/Min step is larger than that at the other

samples. In addition, since the V_{CPD} decreased on both 1 ^{o}C/Min and 2 ^{o}C/Min annealed samples, the Smoluchowski-like dipole may have a larger effect than the local atomic dipole (Kitamura & Iwatsuki 1998).

4.5.2 Modeling of Surface Potential (V_{CPD}) by Topographical Image contrast

In semiconductors, the V_{CPD} may be altered by several factors including dopant concentration, surface roughness, surface charges, adsorbates and the capacitance from the tip geometry (Dixit *et al.,* 2008; Shin *et al.,* 2005). In this regard, a simple and direct method of determining surface potential based on optical imaging was developed. *Imagej 1.48v* software was used to generate optical contrast from the topographical maps of the films (Figure 4.20 (a)). The optical contrast data was then correlated with the surface potential obtained in Figure 4.20 (b and c)). The *imagej 1.48v* software was used to analyse the surface of the film by determining the contrast level of each point, assigning gray value in the range (0-255), and providing a count of the contrast levels. The data was then presented in the form of histograms as shown in Figure 4.21 (a-d) and correlated with surface potential values obtained in Figure 4.21 (e).

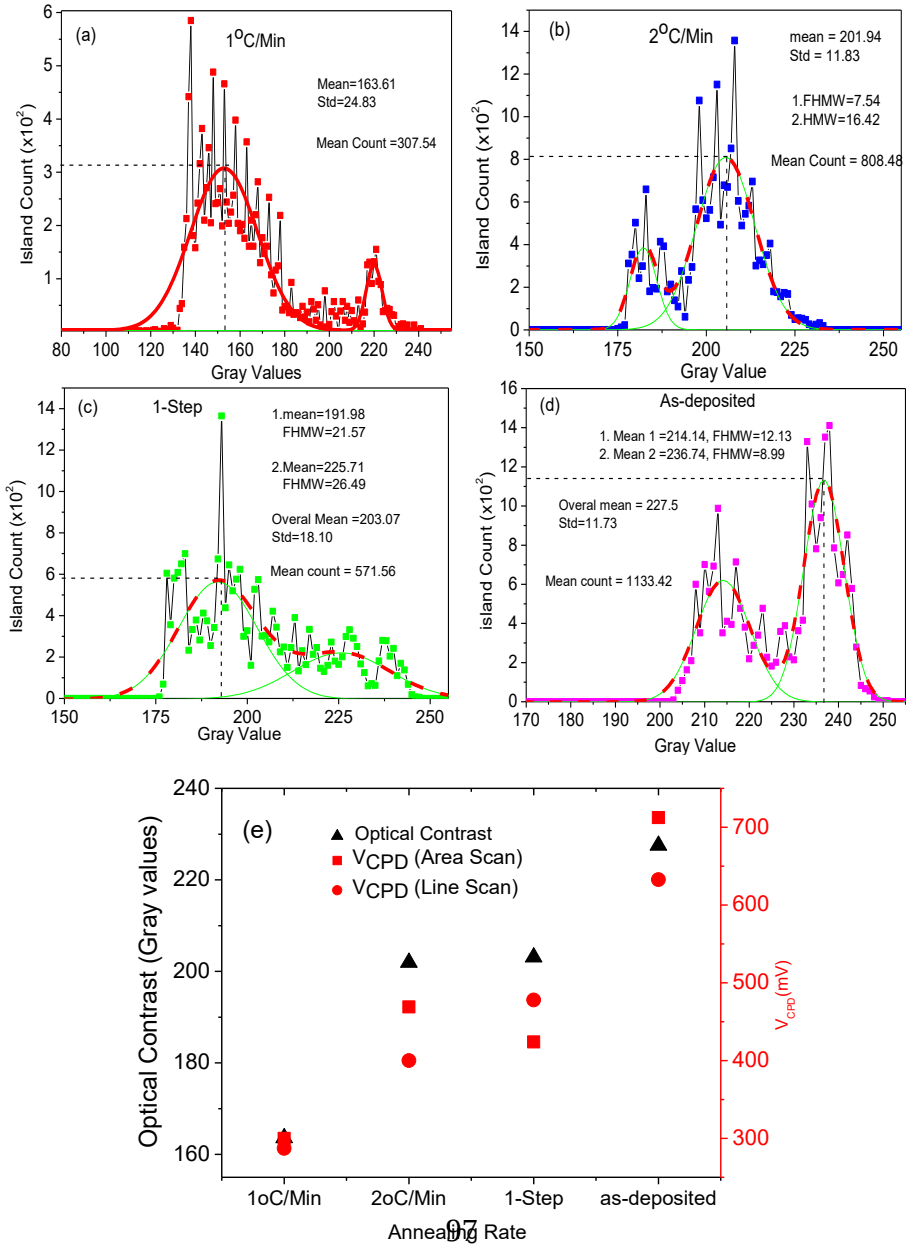
(a)
1°C/Min
Mean=163.61
Std=24.83
Mean Count =307.54
Island Count (x10²)
Gray Values
(b)
2°C/Min
mean = 201.94
Std = 11.83
1.FHMW=7.54
2.HMW=16.42
Mean Count = 808.48
Island Count (x10²)
Gray Value
(c)
1-Step
1.mean=191.98
FHMW=21.57
2.Mean=225.71
FHMW=26.49
Overal Mean =203.07
Std=18.10
Mean count = 571.56
Island Count (x10²)
Gray Value
(d)
As-deposited
1. Mean 1 =214.14, FHMW=12.13
2. Mean 2 =236.74, FHMW=8.99
Overal mean = 227.5
Std=11.73
Mean count = 1133.42
island Count (x10²)
Gray Value
(e)
Optical Contrast
VCPD (Area Scan)
VCPD (Line Scan)
Optical Contrast (Gray values)
VCPD (mV)
1oC/Min
2oC/Min
1-Step
as-deposited
Annealing Rate

Figure 4.21: Topographical Image contrast for (a) 1 ºC/Min, (b) 2 ºC/min, (c) 1-step and (d) as-deposited and (e) Comparison of Optical contrast with Surface potential

The observed trend (Figure 4.21) of the variation in contrast with annealing rate depicts changes in surface properties of the films. The trend (gray values and island count) is consistent with the optical microscopy measurements (Figure 4.3). The modal values of island count in the films recorded are 307.54, 808.48, 571.56 and 1133.42 for the 1 ^{o}C/Min, 2 ^{o}C/min, 1-step and as-deposited TiO_2 films, respectively. On the other hand, the lowest number of counts exhibited by the film annealed at 1^{o}C/Min depicts reconstruction of the crystal structure. That is, agglomeration of islands into larger ones occurred leading to better crystallinity. The variation of gray values in the films is also linked to the heights of islands as observed in the optical microscopy measurements (Figure 4.3). The gray values are obtained from the histograms and depict the heights of the majority of the islands (contrast level). The amorphous film (as-deposited) exhibit the highest gray value of 227.5 while the film annealed at 1 ^{o}C/Min exhibit the lowest gray value of 163.61. The shift in gray values with annealing rates depicts a change in surface roughness or surface morphology. As pointed out in Figure 4.3, reducing the annealing rate results into rougher surface area, a property which leads to enhanced photocatalytic activity as more active catalytic sites are created.

The correlation of optical contrast with V_{CPD} values (Figure 4.21 (e)) indicates a direct relationship between the two parameters. Thus, modeling surface potential with optical contrast provides a simple and rapid route of determining the surface charge properties of films without having to carry out SKPM measurements.

4.5.3 Modeling of Surface Potential with Energy Loss and Optical Band gap

A comparison of the optical parameters (S_{EL}, V_{EL} and band gap) and surface potential measurements (V_{CPD}) model is shown below (Figure 4.22).

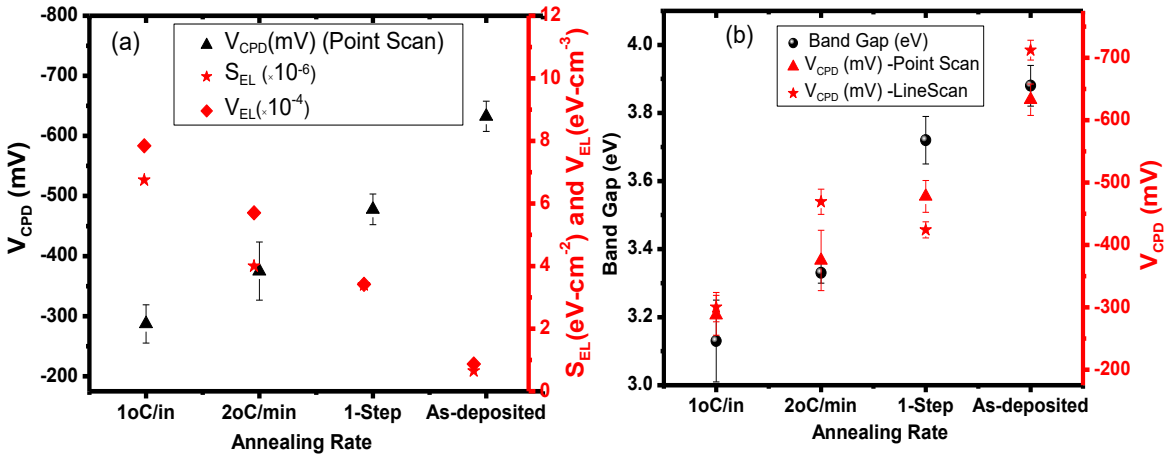

Figure 4.22: (a) Variation of Contact Potential and Energy Loss with Annealing rate (b) Variation of Band gap and Contact Potential with annealing rate

In Figure 4.22(a), the V_{CPD} increases with decrease in annealing rate. The contrary is observed in the S_{EL} and V_{EL} parameters. Further, at high annealing rates, (1 ^{o}C/Min and 2 ^{o}C/Min), the films are dominated by V_{EL} while for the 1-step annealed and the as-deposited film, both S_{EL} and V_{EL} were found to be low. This indicates that there exists incomplete screening of the positive ions cores by conduction electrons. This may have caused upward dipole moment hence the reduced work Function. Moreover, the S_{EL} is attributed to tunnelling current flowing on the surface due to the application of the

electric field while the V_{EL} largely occurred due to increased probability of inter-band transitions for low annealing rates (Miyazaki *et al.,* 2019). The reduction in both S_{EL} and V_{EL} with increase in work function Figure 4.22 (b) indicates that there exists a correlation between energy band gap and V_{CPD} with annealing rates of the TiO_2 thin films. Annealing the films introduces dipole moment which leads to alteration of the material's crystallographic orientation, a phenomenon exhibited by a reduction in V_{CPD} (Kim *et al.,* 2015). Further, the changes in crystallographic orientation is confirmed by the reduced band gap due to densification of the films as high rates of annealing irons out defect sites responsible for localized states (Ravindra *et al.,* 2007; El-Nahass *et al.,* 2016).

4.6 DSSC Performance

From the morphological, optical, structural and SKPM measurements, it is clear that the TiO_2 films subjected to low annealing rates (1^oC/min) exhibit the best features for photocatalysis and hence are potential candidates for application as working electrodes in DSSCs and DSSMs. In this regard, in order to determine the films' dye loading capabilities of the films, optical absorbance was carried out prior to the fabrication of the solar cell devices.

4.6.1 Absorbance of working electrodes

The absorbance can be obtained from the reflectance and transmission spectra on the electrodes using Equation 2.37. Figure 4.23 shows dye loading that illustrates UV-Vis absorption by the dye adsorbed in the nanocrystalline mesoporous TiO_2 film prepared at 1 ^oC/Min and 2 ^oC/Min.

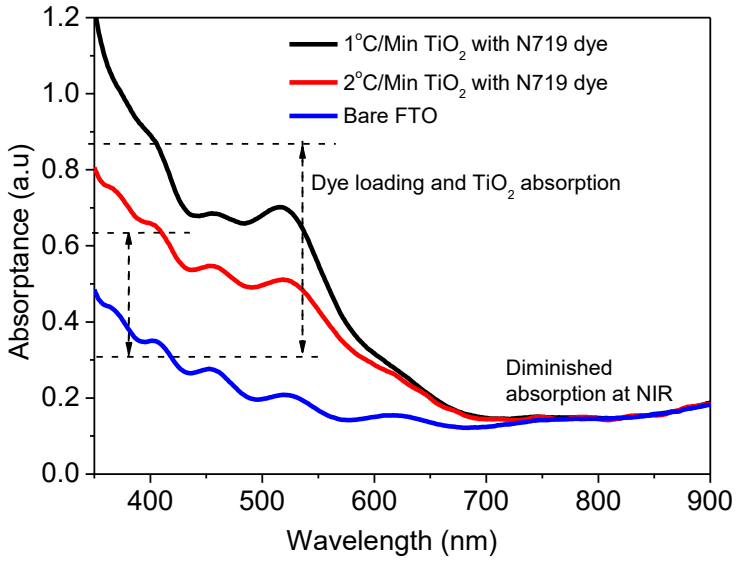

Figure 4.23: Absorption spectra of dye sensitized TiO_2 films coated on FTO and bare FTO.

Figure 4.23 indicates that dye loading is greatest in the visible region and diminishes towards NIR region. The 1 ^{o}C/Min annealed film also show superior dye loading compared to the 2 ^{o}C/Min film. The absorption of light starts to diminish at 525 *nm* spectral wavelength and is consistent with research work reported by Liu *et al*. (2012). The dye sensitized TiO_2 annealed at the 1 ^{o}C/min reveals the best light harvesting capabilities in the wavelength range of 350-650 *nm*. This result differs slightly with the findings of Wang *et al.* (2014) as the authors reported light harvesting in the range 400-700 *nm*. The discrepancy is attributed to the material's preparation methods and annealing temperatures. The high absorption observed in the 1 ^{o}C/Min annealed film may have occurred due to the optical path through multiple scattering of light in the micro-cavities of the TiO_2 films (Liu *et al*., 2012). The absorption may also have resulted from N719 dye as reported by Wang *et al.* (2014). The light scattering capability of TiO_2 films annealed at 1 ^{o}C/Min is, therefore, a fundamental property for efficient harvesting of incident light. The observed trend in Figure 4.22 is consistent

with the transmittance of the TiO_2 films with adsorbed N719 dye molecules shown in Figure 4.24.

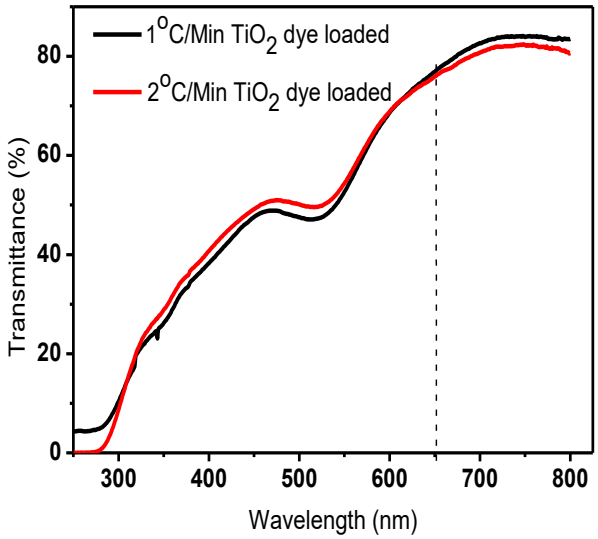

Figure 4.24: Transmittance spectra of N719 dye adsorbed TiO_2 films

The transmittance is significantly low (below 50%) in the spectral range 250-525 *nm*, an indication of high electromagnetic radiation absorption within this range. In this regard, in order to maximize scattering, the ramping rate was maintained at 1 ^oC/Min while the film thickness was maintained at 8.5-10 μm. This is because within this thickness range, the effective charge-carrier diffusion coefficients are large enough that the system is set at large diffusivity limit (Jin *et al.*, 2012). Film thickness below 8.5 μm leads to a reduction in photocurrent due to poor light absorption. On the other hand, increasing the film thickness beyond 10 μm results in decrease in effective charge carrier diffusion coefficients and consequently limited quantum yield. This occurs as more contact area is available for direct-reduction reaction between electrons in the TiO_2 film and the oxidized species in the electrolyte (Jin *et al.*, 2012). This affects the V_{OC}, short-circuit quantum yield and the general efficiency of the device (Nath *et al.*, 2013).

In order to access the morphological, optical, structural properties and surface potential features observed in the films, DSSCs were fabricated and their I-V characteristics obtained and analyzed. Six DSSCs were fabricated and labeled as Cell 1, Cell 2, Cell 3, Cell 4, Cell 5, and Cell 6. Figure 4.25 below shows the I-V characteristics of the DSSCs fabricated using TiO_2 films annealed at 1 ^oC/Min.

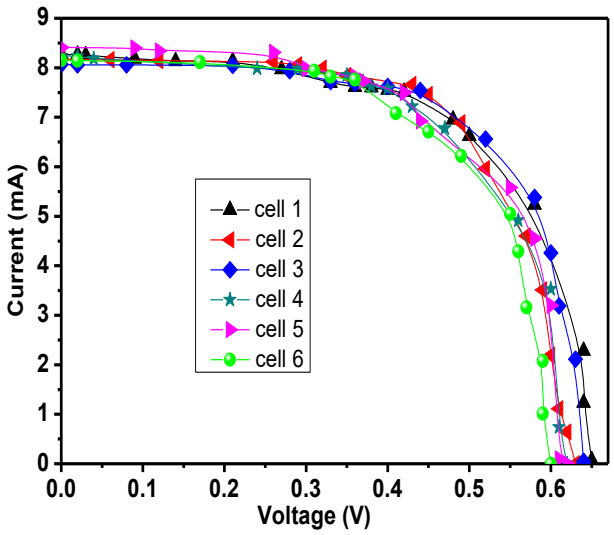

Figure 4.25: I-V Characteristics of DSSCS based on TiO_2 films annealed at 1^oC/Min each of effective area 1.6 cm^2

The DSSCs exhibit relatively high average I_{SC} of 8.23mA and V_{OC} of 0.627 V. It is worth noting that while variation in V_{OC} of DSSCs is dictated by the quasi-Fermi level of the TiO_2 and the potential of the redox couple (Allegrucci *et al*., 2009), the I_{SC} arises from the electron injection efficiency from the N719 dye to the CB of TiO_2 and the efficiency of charge collection (Allegrucci *et al*., 2009; Gong *et al*., 2012). The observed slight variation in the I_{SC} of the DSSCs may have occurred due to slight differences in dye loading of TiO_2 nanoparticles, The DSSCs' FF and PCE were calculated based on Equations 2.9 and 2.10, respectively, and tabulated as shown in Table 4.5.

Table 4.5: I-V characteristics of single DSSCs fabricated from TiO_2 WE annealed at 1 ^oC/Min and of active area 1.6 cm^2

Characteristic	Cell 1	Cell 2	Cell 3	Cell 4	Cell 5	Cell 6
V_{OC} (V)	0.65	0.63	0.64	0.62	0.62	0.6
I_{SC} (mA)	8.27	8.17	8.07	8.24	8.41	8.15
J_{SC} (mA/cm^2)	5.16	5.11	5.04	5.15	5.26	5.09
V_{max} (V)	0.48	0.49	0.52	0.47	0.42	0.49
I_{max} (mA)	6.95	6.89	6.56	6.78	7.50	6.22
J_{max} (mA/cm^2)	4.34	4.31	4.10	4.24	4.69	3.89
P_{max} (mW)	2.08	2.11	2.13	1.99	1.97	1.90
P_{in} W/cm^2	0.1	0.1	0.1	0.1	0.1	0.1
PCE(%)	2.085	2.110	2.132	1.992	1.969	1.905
FF	0.621	0.656	0.660	0.624	0.604	0.623

The PCE recorded was 2.085, 2.110, 2.132, 1.992, 1.969 and 1.905% for Cell 1, Cell 2, Cell 3, Cell 4, Cell 5, and Cell 6, respectively, yielding into an average PCE of 2.03%. The changes in I_{SC} is largely responsible for the variations in PCEs of the DSSCs. In order to assess the influence of surface morphology and optical band gap of the WEs, a comparison of the I-V characteristics of DSSCs based on TiO_2 working electrodes annealed at 1 ^oC/Min and 2 ^oC/Min was made as shown in Figure 4.26.

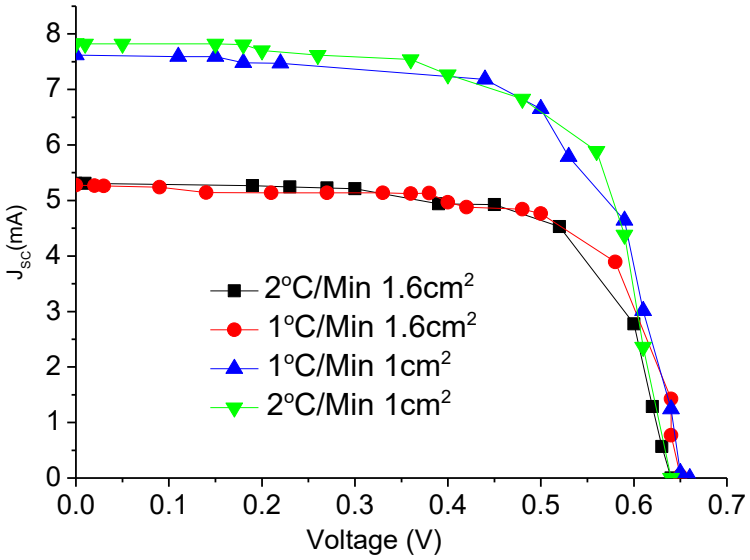

Figure 4.26: J-V characteristics of DSSCs based on TiO_2 working electrodes annealed at 1 °C/Min and 2 °C/Min and of effective areas 1 cm^2 and 1.6 cm^2

From Figure 4.26, there is a distinction in terms of the annealing rates and the effective active area of the DSSCs. The performance of DSSCs annealed at different rates and of 1 cm^2 and 1.6 cm^2 effective active areas was computed and tabulated in Table 4.6.

Table 4.6: Cell Characteristics Based on Area and Annealing Rates

Characteristic	1 °C/Min 1 cm^2	1 °C/Min 1.6 cm^2	2 °C/Min 1 cm^2	2 °C/Min 1.6 cm^2
V_{OC} (V)	0.66	0.65	0.64	0.64
I_{SC} (mA)	7.62	8.44	7.83	8.49
J_{SC} (mA/cm^2)	7.62	4.22	7.83	4.25
V_{max} (V)	0.50	0.50	0.56	0.60
I_{max} (mA)	6.65	7.62	5.89	4.44
J_{max} ($mA//cm^2$)	6.65	3.81	5.89	2.22
P_{max} (mW)	3.33	1.91	3.30	1.33
P_{in} W/cm^2	0.1	0.1	0.1	0.1
PCE(%)	3.325	1.905	3.298	1.332
FF	0.661	0.694	0.658	0.490

The DSSCs with smaller effective area have a higher J_{SC} than those with a larger effective active area and hence recorded high PV performance. This is due to the increased series resistance R_S, which has a direct impact on J_{SC}. Moreover, during the doctor-blading process of WE with large effective working area (1.6 cm^2), chances of introducing crystal defects due bubbles being trapped in the TiO_2 and Platinum films are high. The air bubbles act as charge trapping sites, which enhance scattering of electrons in the films, leading to reduced PCE. The four cells exhibit roughly equal and high V_{OC} of about 0.65 V. This is attributed to the fact that the V_{OC} is determined by the quasi-Fermi level of the TiO_2 and the potential of the redox couple, which was made constant in this work (Allegrucci *et al*., 2009). In regard to the variation in J_{SC}, first, the working electrodes annealed at low rates (1 °C/min) have better catalytic activity compared to those annealed at higher rates. This is attributed to the reduced porosity which, in turn, reduces electron diffusion length and band gap. Consequently, this leads to enhanced

electron injection efficiency from the N719 dye's LUMO to the CB of TiO_2 (Allegrucci *et al*., 2009; Gong *et al*., 2012). Additionally, the TiO_2 working electrodes annealing at low rates have been determined to be more nanostructured than those annealed at higher rates. This is due to the fact that TiO_2 films with large crystallite sizes not only have large surface area but also low defects which account for charge trapping. As a result, the surface energy is more dominant, resulting to a change in the ΔG of the film and hence its chemical activity is enhanced. The large surface area enhances the catalytic activity of nanostructured TiO_2 semiconductor by providing more active sites for the photocatalytic reaction to take place (da Silva, 2008).

4.6.2 I-V Characteristics of DSSMs

4.6.2.1 Series Connection of DSSCs

The DSSCs, each of effective area 1.6 cm^2, were connected in series as shown in Figure 3.5 (a). Five sets of DSSMs were obtained with the DSSCs connection comprising of 2, 3, 4, 5 and 6 DSSCs. The I-V curves and the DSSMs are as shown in Figure 4.27 (a) and (b, c), respectively.

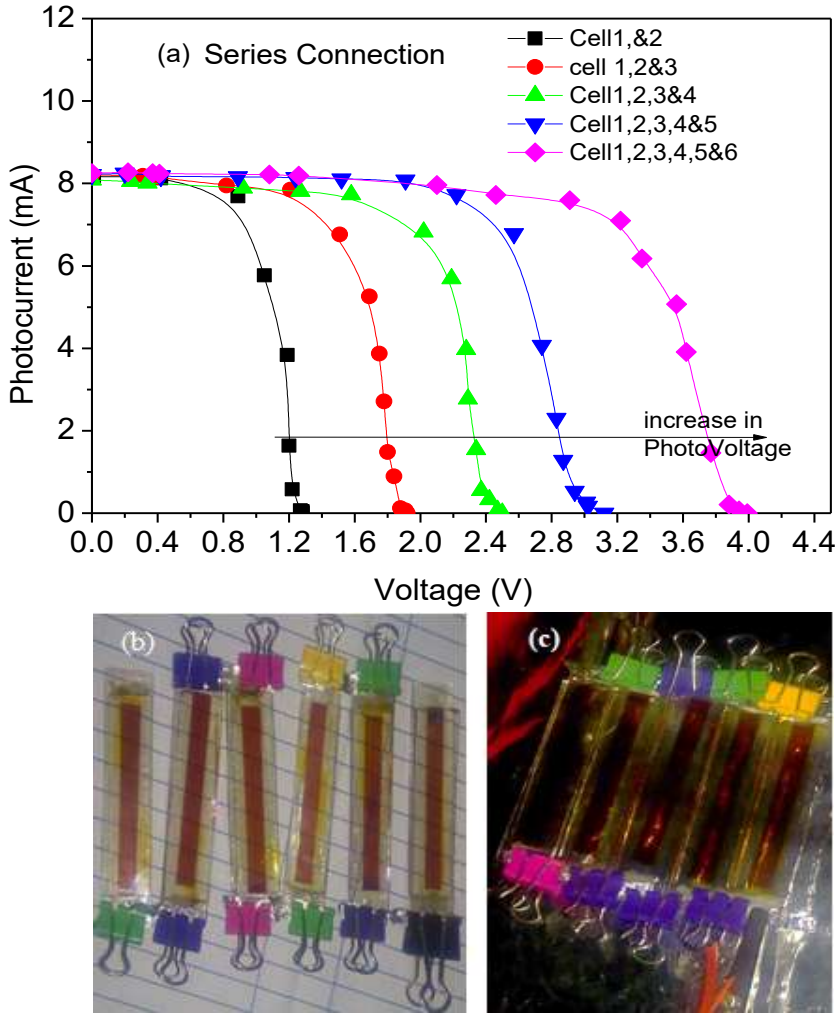

Figure 4.27: (a) I-V characteristics of DSSMs obtained from sets of DSSCs connected in Series. (b) & (c) DSSMs.

From Figure 4.27(a), the V_{OC} increased with increase in the number of DSSCs in the DSSMs while the I_{SC} remained constant (average value of 7.8mA). The V_{OC} varies from 1.28, 1.92, 2.5, 3.12 and 3.99 V for a DSSMs comprising of two, three, four, five and six DSSCs, respectively, connected in series. The I-V characteristics data of each DSSM was obtained, analyzed and tabulated as shown in Table 4.7.

Table 4.7: Current-Voltages characteristics of DSSMs external Circuit (1 ^{o}C/Min 1.6 cm^2) Series Connection

Characteristic	Cell 1 & 2	Cell 1,2&3	Cell 1,2,3&4	Cell 1,2,3,4&5	Cell 1,2,3,4,5&6
V_{OC} (V)	1.28	1.92	2.5	3.12	3.99
I_{SC} (mA)	7.69	6.76	8.08	8.22	8.25
J_{SC} (mA/cm^2)	2.40	1.41	1.26	1.03	0.86
V_{max} (V)	0.89	1.51	2.02	2.57	3.22
I_{max} (mA)	7.69	6.76	6.76	6.78	7.10
J_{max} (mA/cm^2)	2.40	1.41	1.06	0.85	0.74
P_{max} (mW)	2.14	2.13	2.13	2.18	2.38
P_{in} W/cm^2	0.1	0.1	0.1	0.1	0.1
PCE(%)	2.139	2.127	2.134	2.178	2.381
FF	0.695	0.786	0.676	0.679	0.695

The DSSMs exhibit an average PCE of 2.19% and relatively high average FF of 0.71. The DSSMs also exhibit a reduction in J_{SC} as the number of DSSCs increase.

4.6.2.2 Parallel connection of DSSCs

The DSSCs, were then connected in parallel as shown in Figure 3.5 (b), and five sets of DSSMs obtained with the DSSCs connection comprising of 2, 3, 4, 5 and 6 DSSCs. The I-V curves and the DSSMs are as shown in Figure 4.28 (a) and (b, c), respectively.

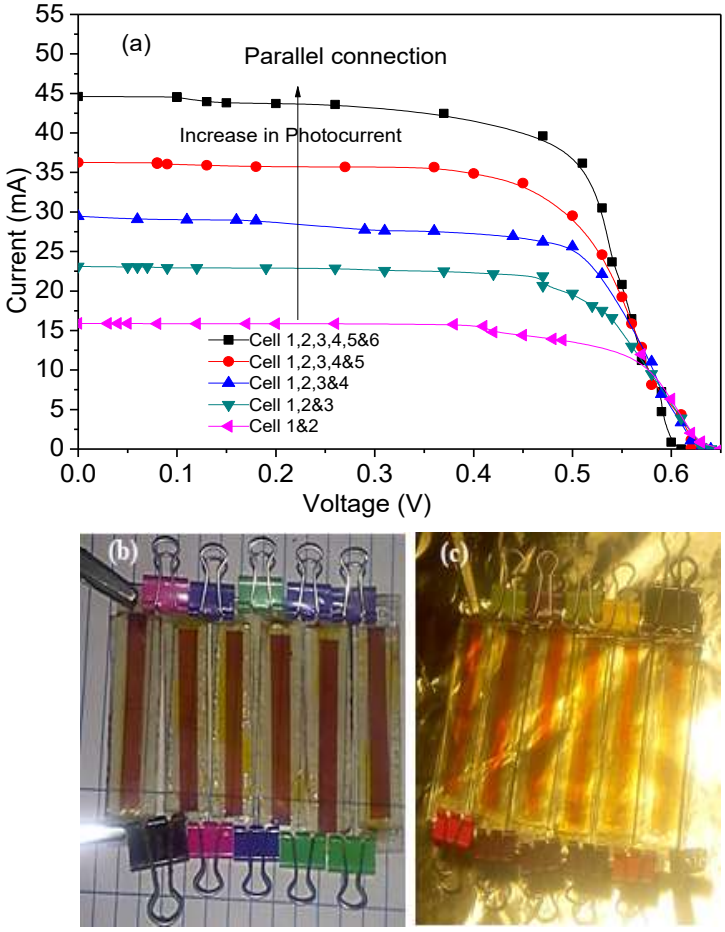

Figure 4.28: (a) I-V characteristics of DSSMs obtained from sets of DSSCs connected in Parallel. (b) & (c) DSSMs.

From Figure 4.28 (a), the DSSMs exhibit an almost constant V_{OC}, varying from 0.61 to 0.65 V for the five sets of DSSMs. However, the I_{SC} increases significantly with the number of DSSCs in the DSSMs. The I_{SC} varies from 15.89, 23.10, 29.45, 36.25 and 44.62 mA for a DSSMs consisting of two, three, four, five and six DSSCs, respectively. The I-V characteristics data of each DSSM was obtained, analyzed and tabulated as shown in Table 4.8.

Table 4.8: I-V characteristics of DSSMs external Circuit (1 ^{o}C/Min 1.6 cm^2) Parallel Connection

Characteristic	Cell 1&2	Cell 1,2&3	Cell 1,2,3&4	Cell 1,2,3,4&5	Cell 1,2,3,4,5&6
V_{OC} (V)	0.65	0.64	0.64	0.63	0.61
I_{SC} (mA)	15.89	23.1	29.45	36.25	44.62
J_{SC} (mA/cm^2)	4.97	4.81	4.60	4.53	4.65
V_{max} (V)	0.57	0.47	0.5	0.48	0.51
I_{max} (mA)	11.98	21.88	25.64	33.64	37.18
J_{max} (mA/cm^2)	3.74	4.56	4.01	4.21	3.87
P_{max} (mW)	2.13	2.14	2.00	2.02	1.98
P_{in} (W)/cm^2	0.1	0.1	0.1	0.1	0.1
PCE (%)	2.134	2.142	2.003	2.018	1.975
FF	0.661	0.696	0.680	0.707	0.697

The DSSMs exhibit an average PCE of 2.055% and relatively high average FF of 0.69. The DSSMs also exhibit a reduction in J_{SC} as the number of DSSCs increase, similar to the observation of J_{SC} for Series connection (Table 4.6). That is, the J_{SC} generated in the DSSMs reduces with increase in effective area. The J_{SC} for the DSSMs in the two modes of connection (Series and Parallel) were plotted as shown in Figure 4.29.

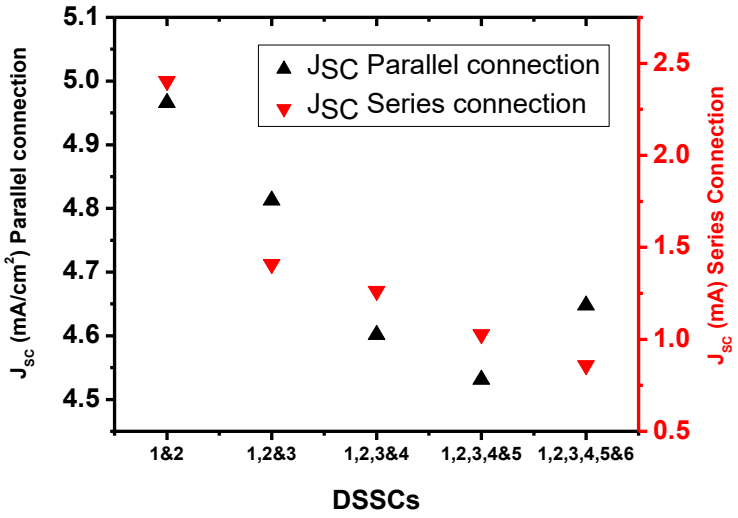

Figure 4.29: Variation of J_{SC} with Active DSSM area

The reduction in J_{SC} in the DSSMs with series connection of DSSCs is believed to have occurred due to the increase in series resistance that resulted from, the bulk resistance of TiO_2, metallic contacts, electrolyte , interconnections and additional resistance of cables introduced during the construction of DSSMs. The current flow in the circuit is dependent on the size of the load or the external resistance in the circuit (Hastuti *et al.*, 2016; Chou *et al.*, 2016). Yang *et al.* (2012) alluded to the fact that series resistance also result from sheet resistance of TCOs. An increase in series resistance leads to a reduction in the FF of the cell and hence lowers its PCE. On the other hand, connecting the DSSCs in parallel reduces the shunt resistance which results from leakages across the cell edges and crystal defects of each cell (Hafez *et al.*, 2012). When shunt resistance decrease, the FF becomes poor and hence the power conversion efficiency (Yang *et al.*, 2012).

In general, the reduction in J_{SC} with increase is DSSMs working area is attributed to a reduction in charge collection efficiency (η_{CC}). The η_{CC} is related to the recombination

time constant (τ_R) as shown in Equation 2.32. Since τ_R is related to photovoltage (V_{Ph}), its high values indicate high η_{CC} and hence high V_{Ph} (Equation 2.33). Also, from Equation 2.32, τ_C is also a function of V_{Ph} as well as DSSC's working area. In fact, based on Transient Photovoltage (TPV) and Transient Photocurrent (TPC) measurements, Wei (2010) reported that τ_C for DSSCs with small working area is an order of magnitude smaller than that for DSSCs with larger working area. This was attributed to the fact that large working area introduces deeper DOS distribution which hinders electron transport. That is, Deeper DOS distribution enhances recombination as electrons become densely localized (trapped) and it becomes difficult for them to get excited in to the CB. Hence, by increasing the working area of the WEs, the τ_R increases, indicating that recombination rate is enhanced (Yan *et al.,* 2019).

4.6.3 DSCCs/ DSSMs Efficiency

The performance of the DSSCs and DSSMs (series and parallel connection) is illustrated in Figure 4.30.

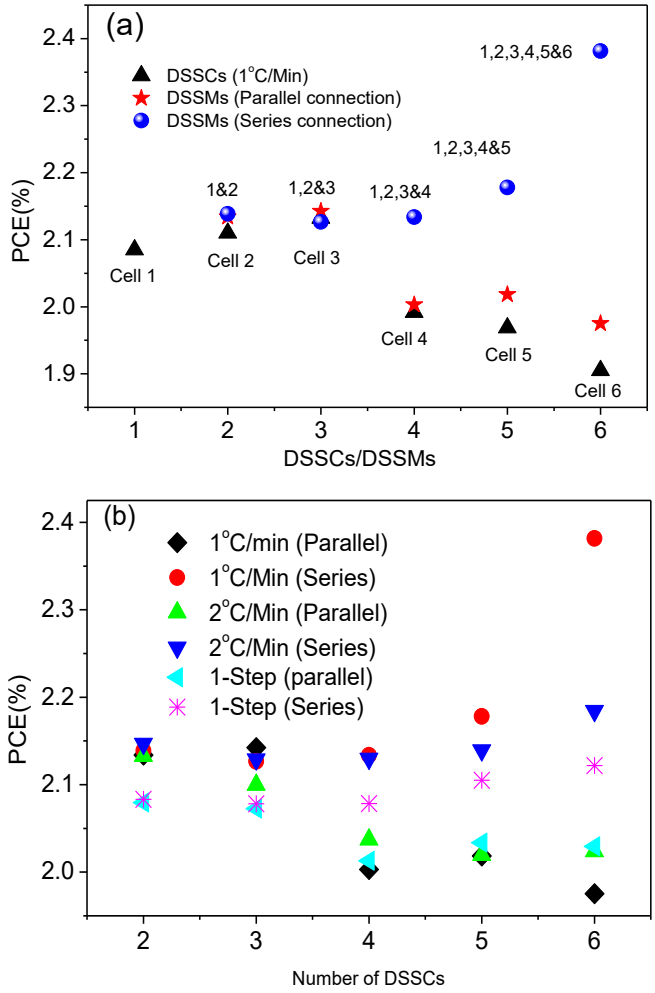

Figure 4.30: Comparison of PCE for DSSCs and DSSMs (Series and Parallel connected) based on TiO_2 WEs annealed at: (a) 1 °C/Min, (b) 1 °C/Min, 2 °C/Min and 1-Step annealed.

From Figure 4.30(a), the DSSCs exhibit varied PCEs, despite having been fabricated using WEs subjected to similar annealing condition. The discrepancy is believed to have occurred from the processing dynamics including the amount of pressure applied during the coating, the presence of defects on some WEs and varied rates of charge recombination at the film interfaces. The DSSMs (with parallel connection of DSSCs) exhibit a decrease in PCE as the active area increases (Figure 4.30 (a)). On the contrary,

the DSSMs (with series connection of DSSCs) exhibit an improvement in PCE as the active area increases. For the series connection, the current flowing in the circuit was low (about 8 mA) and hence copper losses due to the added cable resistance were low. Therefore, the PCE increased with increase in active area. On the other hand, for the parallel connection of the DSSCs, the increase in external circuit current may have led to increase in copper losses, hence reducing the PCE. In Figure 4.30(b), the DSSMs fabricated based on TiO_2 annealed at low rates indicates the highest overall PCE. It is believed that high PCE results from the general outstanding properties of the films subjected to other thermal conditions. For example, they have shown to exhibit high surface roughness which enhances dye adsorption, low band gap (3.13 eV), low surface potential for ease of electron transfer into the TCO and high dye loading capability. All these properties favour the semiconductor's photocatalysis activity.

Moreover, the observations in Figure 4.30 can be explained based on DOS and the depth of charge trap states. The Figure 4.30 shows that charge recombination and collection is affected by the working area of the DSSMs. That is, the working area has a significant effect on trap state DOS and spatial distribution. TPV and TPC measurements have shown that for photovoltage (V_{Ph}) <400 mV, the electronic recombination time (τ_R), which is large for large working areas compared to small working areas of DSCCs, is hardly affected by the V_{Ph}. The phenomenon is associated with the dominance of surface-trap isoenergetic charge recombination (Yan *et al.*, 2019; Wang *et al.*, 2015). However, for $V_{Ph} > 400\ mV$, τ_R is reported to vary with V_{Ph} exponentially due to the multi-trap charge recombination (Kopidakis *et al.*, 2003). Hence, in the region 400-600 mV, the τ_R for large working cell area is shorter than that of small working area. This is due to rapid regeneration of the oxidized Ruthenium N719 dye by the electrolyte. Yan *et al.* (2019) reported a relationship between τ_R and V_{OC} as shown in Equation 2.33. Equation 2.33 indicates that an increase in V_{Ph} leads to an increase in the electronic recombination rate for large working area relative to that of smaller working areas of DSSCs. The effect is believed to arise from deeper DOS distribution exhibited in the

form of larger characteristic energy $K_B T_0$ (Wang *et al.*, 2015). The PCE of DSSCs and DSSMs reduces significantly for large working areas as this results into lower values of V_{OC} due to shorter value of τ_R.

The observed decrease in PCE with increase in the working area of DSSMs is, therefore, attributed to the fact that electrons in the WEs populated deeper trap states and hence excitation into the CB of TiO_2 became difficult. Consequently, electrons hop among the trap state, making this as the only dominant pathway of transport. It is worth noting that the surface traps are localized electronic states and in the band gap and are physically found either at the TiO_2 surface or within a tunneling distance from the surface. Since electrons trapped by the surface states are localized, the charge transfer from the TiO_2 to the electrolyte is slowed down. This accelerates the recombination channel (Bisquert *et al.*, 2004). A deeper DOS distribution is an indication that more electrons are in deep trap states. Therefore, for the DSSMs with large working area, electronic recombination rate is faster than in those with smaller working area.

The phenomena observed in Figure 4.30(b), in which the photoanode films annealed at low rates exhibit the best performance, may be explained in terms of the density of traps. That is, by subjecting the film to the annealing condition, its amorphous nature is ironed out and hence it exhibited a higher density of shallow traps that received more electrons generated from the excited Ruthenium N719 dye, consequently increasing the J_{SC} (Al-Attafi *et al.*, 2018). In addition, large TiO_2 crystallite size or particle size, which is characteristic of films annealed at low rate, leads to energetically shallower trap states which increase the value of J_{SC} in PV devices. It is worth noting that larger TiO_2 particle surface reduces the number of deep trap states due to smaller internal area. However, shrinking the internal surface area of the WE also depress the overall excited dye-to-TiO_2 electron injecting due to the diminished number of adsorbed dye molecules, consequently reducing the J_{SC} (Wang *et al.*, 2015; Yan *et al.*, 2019). Therefore, optimization of TiO_2 is a competitive process and requires careful consideration of the effect on various parameters.

CHAPTER FIVE
CONCLUSION AND RECOMMENDATIONS

5.1 Conclusion

This work has shown that surface roughness of TiO_2 thin films increases with decrease in annealing rate. The surfaces of the films prepared at low annealing rates (1 ^oC/min) exhibit rough surfaces with shallow charge trapping sites due to enhanced mobility of molecules. Annealing directly from room temperature to the sintering led to a reduced surface roughness, a phenomenon attributed to decreased coalescence and agglomeration of the islands. The dependence of crystallite size on optical band gap in TiO_2 films annealed at different rates was also investigated. The refractive index was found to obey the Cauchy's -Model. Low annealing rates resulted into the highest refractive index. On the contrary, the porosity and optical band gap decrease with increase in annealing rate due to films' densification and improved crystallinity. The as-deposited film exhibited optical response only at low electric fields ($712.5-800\ nm$ spectral range), a phenomenon attributed to lack of delocalized charge carriers. Upon annealing, the structural investigation indicated improvement in the crystallite size from $21.8382\ nm$ to $24.3087\ nm$ for 1-step annealed and 1 ^oC/Min, respectively. The as-deposited broadening of the XRD peaks indicated a disordered structure due to defects that are responsible for localized states. Surface potential has been shown to be highest for low annealing rates. The variation in surface potential of the films with annealing rates has also been reported. The changes in surface dipole moment of the surface molecules and the Smoluchowski effect are associated the reported changes in workfunction. The dipole moment has been considered to lower the potential barrier for charge carriers helping to suppress electron-hole recombination, increasing the quantum yield for the chemical reaction, and enhancing the catalytic reactivity of TiO_2 films. In this regard, it has been shown that subjecting the films to low annealing rate makes it attain high surface roughness characteristic of large internal area which favours dye*-to-TiO_2 electron injection hence improved J_{SC}. Low annealing rate of the films also leads to

large crystallite size indicating high density of shallow charge traps. Large working area increases recombination rate and hence slows the transport rate. The effect has been attributed to deeper DOS distribution in large working area films. The correlation between the distributions of DOS, the dynamics of charge recombination and transport and the PCE of PV devices of different working areas have revealed that large working cell areas require careful control of the DOS distribution as well as charge collection efficiency by optimizing the working electrode films.

5.2 Recommendations

The optimization of TiO_2 films as working electrodes for DSSCs and DSSMs is crucial for its photocatalytic activity. This work has utilized optimization by annealing the films at different annealing rate. Further optimization methods including UV exposure, treatment of the films using HCL and the use of nanostructured TiO_2 such as nanoparticles are recommended. Further, this work recommends thermal characterization of TiO_2 films at extremely lower annealing rates such as 0.5 ^oC/Min and 0.25 ^oC/Min and the investigation of the materials surface roughness, crystallite size, band gap and surface potential, and their interdependence. The work also recommends doping technique of TiO_2, including the use of Plasmonic metals and metal oxides geared towards enhancing the material's photocatalytic activity.

REFERENCES

Ahn, Y. U., Kim, E. J., Kim, H. T., & Hahn, S. H. (2003). Variation of structural and optical properties of sol-gel TiO2 thin films with catalyst concentration and calcination temperature. *Materials Letters*, *57*(30), 4660-4666.

Al-Attafi, K., Nattestad, A., Wu, Q., Ide, Y., Yamauchi, Y., Dou, S. X., & Kim, J. H. (2018). The effect of amorphous TiO 2 in P25 on dye-sensitized solar cell performance. *Chemical Communications*, *54*(4), 381-384.

Alexander E. M., Choong-Kwang L., Sang-Min K., Jae-Hyun K. & Chung-Seog O. (2015). Rapid determination of number of graphene layers by relative luminance. *Carbon*, *94*, 646-649.

Ali, R., Saleem, M., Pääkkönen, P., & Honkanen, S. (2015). Thermo-optical properties of thin-film TiO2–Al2O3 bilayers fabricated by atomic layer deposition. *Nanomaterials*, *5*(2), 792-803.

Al-Khafaji, A. A. K. (2013). *Photocatalysis of Sol-Gel Derived (TiO_2) For Anti-Dust Properties* (Doctoral dissertation, University of Baghdad).

Allegrucci, A., Lewcenko, N. A., Mozer, A. J., Dennany, L., Wagner, P., Officer, D. L., ... & Spiccia, L. (2009). Improved performance of porphyrin-based dye sensitised solar cells by phosphinic acid surface treatment. *Energy & Environmental Science*, *2*(10), 1069-1073.

Altobello, S., Bignozzi, C. A., Caramori, S., Larramona, G., Quici, S., Marzanni, G., & Lakhmiri, R. (2004). Sensitization of TiO2 with ruthenium complexes containing boronic acid functions. *Journal of Photochemistry and Photobiology A: Chemistry*, *166*(1-3), 91-98.

Ammar, A. M., Mohamed, H. S., Yousef, M. M., Abdel-Hafez, G. M., Hassanien, A. S., & Khalil, A. S. (2019). Dye-sensitized solar cells (DSSCs) based on extracted natural dyes. *Journal of Nanomaterials*, *2019*.

Asahi, R., Taga, Y., Mannstadt, W., & Freeman, A. J. (2000). Electronic and optical properties of anatase TiO 2. *Physical Review B*, *61*(11), 7459.

Avrutin, V., Izyumskaya, N., & Morkoç, H. (2014). Amorphous and micromorph Si solar cells: current status and outlook. *Turkish Journal of Physics*, *38*(3), 526-542.

Badran, H. A., Al-Mudhaffer, M. F., Hassan, Q. M., & Al-Ahmad, A. Y. (2012). Study of the linear optical properties and surface energy loss of 5′, 5 ″-dibromo-o-cresolsulfophthalein thin films. *Chalcogenide Letters*, *9*(12), 483-493.

Badwal, S. P. S., Bak, T., Jiang, S. P., Love, J., Nowotny, J., Rekas, M., ... & Vance, E. R. (2001). Application of work function measurements for surface monitoring of oxide electrode materials (La, Sr)(Co, Mn, Fe) O3. *Journal of Physics and Chemistry of Solids*, *62*(4), 723-729.

Baglio V., Girolamo M. and Arico A. A. S. (2011). Influence of TiO_2 film thickness on the electrochemical behavior of dye sensitized solar cells. *International Journal of Electrochemical Science,* **6**: 3375-3384.

Bak, T., Nowotny, J., Rekas, M., & Sorrell, C. C. (2002). Photo-electrochemical hydrogen generation from water using solar energy. Materials-related aspects. *International journal of hydrogen energy*, *27*(10), 991-1022

Balfour, J. R., & Shaw, M. (2011). *Introduction to photovoltaic system design*. Burlington: Jones & Bartlett Publishers.

Barbe, C. J., Arendse, F., Comte, P., Jirousek, M., Lenzmann, F., Shklover, V., & Grätzel, M. (1997). Nanocrystalline titanium oxide electrodes for photovoltaic applications. *Journal of the American Ceramic Society*, *80*(12), 3157-3171.

Bartic, M., Sacarescu, L., & Harabagiu, V. (2013). Optical and electrical properties of TiO2 thin films deposited by sol-gel method. *Revue Roumaine de Chimie*, *58*(2-3), 105-111.

Baruch, P., De Vos, A., Landsberg, P. T., & Parrott, J. E. (1995). On some thermodynamic aspects of photovoltaic solar energy conversion. *Solar Energy Materials and Solar Cells*, *36*(2), 201-222.

Başol, B. M., & McCandless, B. (2014). Brief review of cadmium telluride-based photovoltaic technologies. *Journal of photonics for Energy*, *4*(1), 040996.

Beckmann, P., & Spizzichino, A. (1987). The scattering of electromagnetic waves from rough surfaces. *Norwood, MA, Artech House, Inc., 1987, 511 p.*

Belarbi, M., Benyoucef, A., & Benyoucef, B. (2014). Study of the equivalent circuit of adye-sensitized solar cells. *Advanced Energy: An International Journal (AEIJ)*, *1*(2), 1-8.

Bisquert, J., Zaban, A., Greenshtein, M., & Mora-Seró, I. (2004). Determination of rate constants for charge transfer and the distribution of semiconductor and electrolyte electronic energy levels in dye-sensitized solar cells by open-circuit photovoltage decay method. *Journal of the American Chemical Society*, *126*(41), 13550-13559.

Borodin, A., & Reichling, M. (2011). Characterizing TiO 2 (110) surface states by their work function. *Physical Chemistry Chemical Physics*, *13*(34), 15442-15447.

Boschloo, G., & Hagfeldt, A. (2009). Characteristics of the iodide/triiodide redox mediator in dye-sensitized solar cells. *Accounts of chemical research*, *42*(11), 1819-1826.

Boxwell, M. (2012). *Solar electricity handbook: A simple practical guide to solar energy: how to design and install photovoltaic solar electric systems*. Ryton on Dunsmore, Warwickshire, U.K: Greenstream Publishing.

Brown, G. F., & Wu, J. (2009). Third generation photovoltaics. *Laser & Photonics Reviews*, *3*(4), 394-405.

Burke, A., Ito, S., Snaith, H., Bach, U., Kwiatkowski, J., & Grätzel, M. (2008). The function of a TiO2 compact layer in dye-sensitized solar cells incorporating "planar" organic dyes. *Nano letters*, *8*(4), 977-981.

Campos, C. S., Spada, E. R., De Paula, F. R., Reis, F. T., Faria, R. M., & Sartorelli, M. L. (2012). Raman and XRD study on brookite–anatase coexistence in cathodic electrosynthesized titania. *Journal of Raman Spectroscopy*, *43*(3), 433-438.

Canto-Aguilar, E. J., Rodríguez-Pérez, M., García-Rodríguez, R., Lizama-Tzec, F. I., De Denko, A. T., Osterloh, F. E., & Oskam, G. (2017). ZnO-based dye-sensitized

solar cells: Effects of redox couple and dye aggregation. *Electrochimica Acta*, *258*, 396-404.

Carella, A., Borbone, F., & Centore, R. (2018). Research progress on photosensitizers for DSSC. *Frontiers in chemistry*, *6*, 481.

Chen L., Hsu C., Chan P., Zhang X. & Huang C. (2014). Improving the performance of dye-sensitized solar cells with TiO2/graphene/ TiO2 sandwich structure. *Nanoscale Research Letters,* **9**:380 -389.

Chen, X., Lou, Y. B., Samia, A. C., Burda, C., & Gole, J. L. (2005). Formation of oxynitride as the photocatalytic enhancing site in nitrogen-doped titania nanocatalysts: comparison to a commercial nanopowder. *Advanced functional materials*, *15*(1), 41-49.

Chou, J. C., Huang, C. H., Liao, Y. H., Lin, Y. J., Chu, C. M., & Nien, Y. H. (2016). Analysis of different series-parallel connection modules for dye-sensitized solar cell by electrochemical impedance spectroscopy. *International Journal of Photoenergy*, *2016*.

Chou, Y. T., Ko, Y. T., & Yan, M. F. (1987). Fluid flow model for ceramic tape casting. *Journal of the American Ceramic Society*, *70*(10), C-280.

Clarke, T. M., & Durrant, J. R. (2010). Charge photogeneration in organic solar cells. *Chemical reviews*, *110*(11), 6736-6767.

Conibeer, G. (2007). Third-generation photovoltaics. *Materials today*, *10*(11), 42-50.

Cui, Y., Du, H., & Wen, L. S. (2008). Doped-TiO2 photocatalysts and synthesis methods to prepare TiO2 films. *Journal of Materials Science & Technology*, 24(5), 675-689.

Cui, Z., Zhao, M., Que, X., Wang, J., Xu, Y., Ghazzal, M. N., ... & Wu, W. (2021). Facile Vacuum Annealing-Induced Modification of TiO2 with an Enhanced Photocatalytic Performance. *ACS omega*, *6*(41), 27121-27128.

De Crescenzi, M., & Piancastelli, M. N. (1996). *Electron scattering and related spectroscopies*. New Jersey: World Scientific.

De Mendonca, V. R., & Ribeiro, C. (2011). Influence of TiO2 morphological parameters in dye photodegradation: a comparative study in peroxo-based synthesis. *Applied Catalysis B: Environmental*, *105*(3-4), 298-305.

De Mendonça, V. R., Lopes, O. F., Fregonesi, R. P., Giraldi, T. R., & Ribeiro, C. (2014). TiO2-SnO2 heterostructures applied to dye photodegradation: The relationship between variables of synthesis and photocatalytic performance. *Applied surface science*, *298*, 182-191.

Pva A. N., (2011). Guide To Interpreting IV Curve Measurements of PV Arrays. *Solmetric Application Note*.

Deshmukh, H. P., Shinde, P. S., & Patil, P. S. (2006). Structural, optical and electrical characterization of spray-deposited TiO2 thin films. *Materials Science and Engineering: B*, *130*(1-3), 220-227.

Dessler, A. (2015). *Introduction to modern climate change*. Cambridge: Cambridge University Press.

Dissanayake, M. A. K. L., Umair, K., Senadeera, G. K. R., Jaseetharan, T., Weerasinghe, A. M. J. S., & Wijayasinghe, H. W. M. A. C. (2022). Plasmonic gold nanoparticle incorporated MgO-coated SnO2 photoanode for efficiency enhancement in dye-sensitized solar cells. *Solar Energy*, *233*, 363-377.

Dixit, S., Srivastava, A., Shukla, R. K., & Srivastava, A. (2008). Pulsed laser deposited ZnO films and their humidity sensing behavior. *Journal of Materials Science: Materials in Electronics*, *19*(8-9), 788-792.

Dodoo-Arhin D., Fabiane M., Bello A. & Manyala N. (2013). Graphene: Synthesis, transfer, and characterization for dye sensitized solar cells applications. *Industrial and Engineering Chemistry Research.* **52:** 14160-14168.

Dozzi, M. V., & Selli, E. (2013). Doping TiO2 with p-block elements: Effects on photocatalytic activity. *Journal of Photochemistry and Photobiology C: Photochemistry Reviews*, *14*, 13-28.

El-Nahass, M. M., Ali, M. H., & El-Denglawey, A. (2012). Structural and optical properties of nano-spin coated sol–gel porous TiO2 films. *Transactions of Nonferrous Metals Society of China*, *22*(12), 3003-3011.

El-Nahass, M. M., Soliman, H. S., & El-Denglawey, A. (2016). Absorption edge shift, optical conductivity, and energy loss function of nano thermal-evaporated N-type anatase TiO_2 films. *Applied Physics A*, *122*(8), 775.

Euvananont, C., Junin, C., Inpor, K., Limthongkul, P., & Thanachayanont, C. (2008). TiO2 optical coating layers for self-cleaning applications. *Ceramics International*, *34*(4), 1067-1071.

Fondriest. (2018). *Solar Radiation & Photosynthetically Active Radiation.* Retrieved from: https://www.fondriest.com/environmentalmeasurements/parameters/weather/photosynthetically-active-radiation/

Frederichi, D., Scaliante, M. H. N. O., & Bergamasco, R. (2021). Structured photocatalytic systems: photocatalytic coatings on low-cost structures for treatment of water contaminated with micropollutants—a short review. *Environmental Science and Pollution Research*, *28*(19), 23610-23633.

French, R. H. (2000). Origins and applications of London dispersion forces and Hamaker constants in ceramics. *Journal of the American Ceramic Society*, *83*(9), 2117-2146.

Fthenakis, V. M. (2018). *Overview of potential hazards*. In *McEvoy's Handbook of Photovoltaics* (pp. 1195-1212). Academic Press.

Gao, D. L., Wang, Y., Zhang, P., Fu, L. M., Ai, X. C., & Zhang, J. P. (2015). New insights into electrolyte-component biased and transfer-and transport-limited charge recombination in dye-sensitized solar cells. *RSC advances*, *5*(103), 84959-84966.

Gasiorowski, J., Menon, R., Hingerl, K., Dachev, M., & Sariciftci, N. S. (2013). Surface morphology, optical properties and conductivity changes of poly (3, 4-

ethylenedioxythiophene): poly (styrenesulfonate) by using additives. *Thin Solid Films*, *536*, 211-215.

Glassford, K. M., & Chelikowsky, J. R. (1992). Structural and electronic properties of titanium dioxide. *Physical Review B*, *46*(3), 1284.

Gong, J., Liang, J., & Sumathy, K. (2012). Review on dye-sensitized solar cells (DSSCs): fundamental concepts and novel materials. *Renewable and Sustainable Energy Reviews*, *16*(8), 5848-5860.

Goodrich, A., Hacke, P., Wang, Q., Sopori, B., Margolis, R., James, T. L., & Woodhouse, M. (2013). A wafer-based monocrystalline silicon photovoltaics road map: Utilizing known technology improvement opportunities for further reductions in manufacturing costs. *Solar Energy Materials and Solar Cells*, *114*, 110-135.

Goswami, A. (1996). *Thin film fundamentals*. New Delhi: Age International.

Govindasamy, G., Murugasen, P., & Sagadevan, S. (2016). Investigations on the synthesis, optical and electrical properties of TiO2 thin films by chemical bath deposition (CBD) method. *Materials Research*, *19*(2), 413-419.

Gracia-Amillo, A. M., Bardizza, G., Salis, E., Huld, T., & Dunlop, E. D. (2018). Energy-based metric for analysis of organic PV devices in comparison with conventional industrial technologies. *Renewable and Sustainable Energy Reviews*, *93*, 76-89.

Green, M. A., Emery, K., Hishikawa, Y., Warta, W., & Dunlop, E. D. (2012). Solar cell efficiency tables (version 39). *Progress in Photovoltaics: Research and Applications*, ***20***(1), 12-20.

Guang-Lei, T., Shi-Gang, W., Lu-Yun, Y., Kang-Ying, S., Lai-Shun, Q., & Jian-Da, S. (2007). Influence of annealing temperature on structure, optical loss and laser-induced damage threshold of TiO2 thin films. *Chinese Physics Letters*, *24*(10), 2967.

Gurevich, V. L., & Tagantsev, A. K. (1991). Intrinsic dielectric loss in crystals. *Advances in Physics*, *40*(6), 719-767.

Hafez, H. S., Yahia, I. S., Sakr, G. B., Abdel-Mottaleb, M. S. A., & Yakuphanoglu, F. (2012). Extraction of the DSSC parameters based TiO2 under dark and illumination conditions. *Adv. Mater. Corros*, *1*, 8-13.

Hagfeldt, A., & Graetzel, M. (1995). Light-induced redox reactions in nanocrystalline systems. *Chemical reviews*, *95*(1), 49-68.

Hagfeldt, A., & Grätzel, M. (2000). Molecular photovoltaics. *Accounts of Chemical Research*, *33*(5), 269-277.

Hara, K., Kurashige, M., Dan-oh, Y., Kasada, C., Shinpo, A., Suga, S., ... & Arakawa, H. (2003). Design of new coumarin dyes having thiophene moieties for highly efficient organic-dye-sensitized solar cells. *New Journal of Chemistry*, *27*(5), 783-785.

Harrison, K., Levene, J. I., Rajeshwar, K., McConnell, R., & Licht, S. (2008). Solar Hydrogen Generation–Toward a Renewable Energy Future. *Electrolysis of water. New York: Springer Inc*, 41-64.

Hastuti, S. D., Nurosyid, F., Supriyanto, A., & Suryana, R. (2016, November). Modification of circuit module of dye-sensitized solar cells (DSSC) for solar windows applications. In *Journal of Physics: Conference Series* (Vol. 776, No. 1, p. 012003). IOP Publishing.

Hayashi, N., Ishii, H., Ouchi, Y., & Seki, K. (2002). Examination of band bending at buckminsterfullerene (C 60)/metal interfaces by the Kelvin probe method. *Journal of applied physics*, *92*(7), 3784-3793.

Holder, J. K. L. (2013). *Quantum structures in photovoltaic devices* (Doctoral dissertation, University of Oxford).

Hölzl, J., & Schulte, F. K. (1979). *Work function of metals. In Solid surface.* Berlin, Heidelberg: Springer-Verlag.

Hou, Y. Q., Zhuang, D. M., Zhang, G., Zhao, M., & Wu, M. S. (2003). Influence of annealing temperature on the properties of titanium oxide thin film. *Applied Surface Science*, *218*(1-4), 98-106.

Howard, C. J., Sabine, T. M., & Dickson, F. (1991). Structural and thermal parameters for rutile and anatase. *Acta Crystallographica Section B: Structural Science*, *47*(4), 462-468.

Howe, R. F., & Gratzel, M. (1987). EPR study of hydrated anatase under UV irradiation. *Journal of Physical Chemistry*, *91*(14), 3906-3909.

Theiss (2022). *OJL model.* Retrived from:

http://www.mtheiss.com/docs/scout2/index.html?ojl_model.htm/

Huang, S. Y., Schlichthörl, G., Nozik, A. J., Grätzel, M., & Frank, A. J. (1997). Charge recombination in dye-sensitized nanocrystalline TiO2 solar cells. *The Journal of Physical Chemistry B*, *101*(14), 2576-2582.

Ishibashi, S., Higuchi, Y., Ota, Y., & Nakamura, K. (1990). Low resistivity indium–tin oxide transparent conductive films. II. Effect of sputtering voltage on electrical property of films. *Journal of Vacuum Science & Technology A: Vacuum, Surfaces, and Films*, *8*(3), 1403-1406.

Ishida, H., & Terakura, K. (1987). Coverage dependence of the work function and charge transfer on the alkali-metal-jellium surface. *Physical Review B*, *36*(8), 4510.

Ishii, H., Sugiyama, K., Ito, E., & Seki, K. (1999). Energy level alignment and interfacial electronic structures at organic/metal and organic/organic interfaces (vol 11, pg 605, 1999). *Advanced Materials*, *11*(12), 972-972.

Jayawardena, K. I., Rozanski, L. J., Mills, C. A., Beliatis, M. J., Nismy, N. A., & Silva, S. R. P. (2013). 'Inorganics-in-Organics': recent developments and outlook for 4G polymer solar cells. *Nanoscale*, *5*(18), 8411-8427.

Jiang, C. S., Ptak, A., Yan, B., Moutinho, H. R., Li, J. V., & Al-Jassim, M. M. (2009). Microelectrical characterizations of junctions in solar cell devices by scanning Kelvin probe force microscopy. *Ultramicroscopy*, *109*(8), 952-957.

Jin M., Kim S.S., Yoon M., Liz Z., Lee Y. Y. and Kim J. M. (2012). Mesoporous inverse opal TiO2 film as light scattering layer for dye-sensitized solar cell. *Journal of Nanoscience and Nanotechnology*, **12**(1): 815-821

Juma, A., Acik, I. O., Mere, A., & Krunks, M. (2016). Dielectric relaxation and conduction mechanisms in sprayed TiO2 thin films as a function of the annealing temperature. *Applied Physics A*, *122*(4), 1-6.

Kao, M. C., Chen, H. Z., Young, S. L., Kung, C. Y., & Lin, D. C. (2009). The effects of the thickness of TiO2 films on the performance of dye-sensitized solar cells. *Thin Solid Films*, *517*(17), 5096-5099.

Kapilashrami, M., Zhang, Y., Liu, Y. S., Hagfeldt, A., & Guo, J. (2014). Probing the optical property and electronic structure of TiO2 nanomaterials for renewable energy applications. *Chemical reviews*, *114*(19), 9662-9707.

Katoh R., Huijser A., Hara K., Savenije T. M. and Siebbeles D.A. (2007). Effect of the particle size on the electron injection efficiency in dye-sensitized nanocrystalline TiO2 films studied by time-resolved microwave conductivity (TRMC) measurements. *Journal of Physical Chemistry. C.* **111:** 10741-10746.

Katoh, R. (2012). Quantitative evaluation of electron injection efficiency in dye-sensitized TiO_2 films. *Ambio*, *41*(2), 143-148.

Khan, M. I. (2013). *A Study on the Optimization of Dye-Sensitized Solar Cells*. University of South Florida.

Kim, H., & Kim, D. W. (2011). Transport characteristics and surface potential distribution of electrically stressed TiO_2 single crystals. *Applied Physics A*, *102*(4), 949-953.

Kim, H., Hong, S., & Kim, D. W. (2012). Ambient effects on electric-field-induced local charge modification of TiO2. *Applied Physics Letters*, *100*(2), 022901.

Kim, S. K., Raj, C. J., & Kim, H. J. (2014). CdS/CdSe quantum dot-sensitized solar cells based on ZnO nanoparticle/nanorod composite electrodes. *Electronic Materials Letters*, *10*(6), 1137-1142.

Kim, S. M., Rim, Y. S., Keum, M. J., & Kim, K. H. (2009). Study on the electrical and optical properties of ITO and AZO thin film by oxygen gas flow rate. *Journal of electroceramics*, *23*(2-4), 341.

Kim, S., Sinai, O., Lee, C. W., & Rappe, A. M. (2015). Controlling oxide surface dipole and reactivity with intrinsic nonstoichiometric epitaxial reconstructions. *Physical Review B*, *92*(23), 235431.

Kirchmeyer, S., & Reuter, K. (2005). Scientific importance, properties and growing applications of poly (3, 4-ethylenedioxythiophene). *Journal of Materials Chemistry*, ***15***(21), 2077-2088.

Kitamura, S. I., & Iwatsuki, M. (1998). High-resolution imaging of contact potential difference with ultrahigh vacuum noncontact atomic force microscope. *Applied Physics Letters*, *72*(24), 3154-3156.

Kopidakis, N., Benkstein, K. D., Van De Lagemaat, J., & Frank, A. J. (2003). Transport-limited recombination of photocarriers in dye-sensitized nanocrystalline TiO2 solar cells. *The Journal of Physical Chemistry B*, *107*(41), 11307-11315.

Krebs, F. C. (Ed.). (2012). *Stability and degradation of organic and polymer solar cells*. West Sussex: John Wiley & Sons.

Kronik, L., & Shapira, Y. (1999). Surface photovoltage phenomena: theory, experiment, and applications. *Surface science reports*, *37*(1-5), 1-206.

Kudo, A., & Miseki, Y. (2009). Heterogeneous photocatalyst materials for water splitting. *Chemical Society Reviews*, *38*(1), 253-278.

Lai, Y. W., Krause, M., Savan, A., Thienhaus, S., Koukourakis, N., Hofmann, M. R., & Ludwig, A. (2011). High-throughput characterization of film thickness in thin film materials libraries by digital holographic microscopy. *Science and Technology of Advanced Materials*.

Lang, N. D., & Kohn, W. (1971). Theory of metal surfaces: work function. *Physical Review B*, *3*(4), 1215.

Lee, J. J., Coia, G. M., & Lewis, N. S. (2004). Current density versus potential characteristics of dye-sensitized nanostructured semiconductor photoelectrodes. 2. Simulations. *The Journal of Physical Chemistry B*, *108*(17), 5282-5293.

Li, F., Chen, C., Tan, F., Li, C., Yue, G., Shen, L., & Zhang, W. (2014). Semitransparent inverted polymer solar cells employing a sol-gel-derived TiO 2 electron-

selective layer on FTO and MoO 3/Ag/MoO 3 transparent electrode. *Nanoscale research letters*, *9*(1), 1-5.

Li, K. N., Wang, Y. F., Xu, Y. F., Chen, H. Y., Su, C. Y., & Kuang, D. B. (2013). Macroporous SnO_2 synthesized via a template-assisted reflux process for efficient dye-sensitized solar cells. *ACS Applied Materials & Interfaces*, *5*(11), 5105-5111.

Liberatore, M., Burtone, L., Brown, T. M., Reale, A., Di Carlo, A., Decker, F., ... & Bignozzi, C. A. (2009). On the effect of Al 2 O 3 blocking layer on the performance of dye solar cells with cobalt based electrolytes. *Applied Physics Letters*, *94*(17), 173113.

Lin, S. H., Su, Y. H., Cho, H. W., Kung, P. Y., Liao, W. P., & Wu, J. J. (2016). Nanophotonic perovskite solar cell architecture with a three-dimensional TiO 2 nanodendrite scaffold for light trapping and electron collection. *Journal of Materials Chemistry A*, *4*(3), 1119-1125.

Liu, D. W., Cheng, I. C., Chen, J. Z., Chen, H. W., Ho, K. C., & Chiang, C. C. (2012). Enhanced optical absorption of dye-sensitized solar cells with microcavity-embedded TiO 2 photoanodes. *Optics express*, *20*(102), A168-A176.

Liu, J., Liu, Y., Liu, N., Han, Y., Zhang, X., Huang, H., ... & Kang, Z. (2015). Metal-free efficient photocatalyst for stable visible water splitting via a two-electron pathway. *Science*, *347*(6225), 970-974.

Liu, X., Gao, S., Xu, H., Lou, Z., Wang, W., Huang, B., & Dai, Y. (2013). Green synthetic approach for Ti 3+ self-doped TiO_{2-x} nanoparticles with efficient visible light photocatalytic activity. *Nanoscale*, *5*(5), 1870-1875.

Liu, Y., Lan, K., Li, S., Liu, Y., Kong, B., Wang, G., ... & Al-Enizi, A. M. (2017). Constructing three-dimensional mesoporous bouquet-posy-like TiO2 superstructures with radially oriented mesochannels and single-crystal walls. *Journal of the American Chemical Society*, *139*(1), 517-526.

Ma, Y., Wang, X., Jia, Y., Chen, X., Han, H., & Li, C. (2014). Titanium dioxide-based nanomaterials for photocatalytic fuel generations. *Chemical reviews*, *114*(19), 9987-10043.

Makhlouf, M. M., El-Denglawey, A., Zeyada, H. M., & El-Nahass, M. M. (2014). The structural and optical characterizations of tetraphenylporphyrin thin films. *Journal of Luminescence*, *147*, 202-208.

Marinado, T. (2009). *Photoelectrochemical studies of dye-sensitized solar cells using organic dyes*. Unpublished PhD dissertation, Stockholm: KTH Royal Institute of Technology. Retrieved from http://urn.kb.se/resolve?urn=urn:nbn:se:kth:diva-11248.

Mathews, N. R., Morales, E. R., Cortés-Jacome, M. A., & Antonio, J. T. (2009). TiO2 thin films–Influence of annealing temperature on structural, optical and photocatalytic properties. *Solar Energy*, *83*(9), 1499-1508.

Mehmood, U., Rahman, S. U., Harrabi, K., Hussein, I. A., & Reddy, B. V. S. (2014). Recent advances in dye sensitized solar cells. *Advances in Materials Science and Engineering*, *2014*.

Mital, G. S. & Tripathi M. (2016). *A review of TiO_2 nanoparticles Chinese Science Bulletin*, *56*(16), 1639-1657.

Miyazaki, M., Wen, H. F., Zhang, Q., Adachi, Y., Brndiar, J., Štich, I., ... & Sugawara, Y. (2019). Imaging the surface potential at the steps on the rutile TiO2 (110) surface by Kelvin probe force microscopy. *Beilstein journal of nanotechnology*, *10*(1), 1228-1236.

Mo, S. D., & Ching, W. Y. (1995). Electronic and optical properties of three phases of titanium dioxide: Rutile, anatase, and brookite. *Physical Review B*, *51*(19), 13023.

Montanari, I., Nelson, J., & Durrant, J. R. (2002). Iodide electron transfer kinetics in dye-sensitized nanocrystalline TiO2 films. *The Journal of Physical Chemistry B*, *106*(47), 12203-12210.

Muaz, A. K. M., Hashim, U., Arshad, M. M., Ruslinda, A. R., Ayub, R. M., Gopinath, S. C., ... & Foo, K. L. (2016, July). Effect of annealing temperature on structural, morphological and electrical properties of nanoparticles TiO_2 thin films by sol-gel method. In *AIP Conference Proceedings* 1733(1) 020087).

Mugo, S., & Yuan, J. (2012). Influence of surface adsorption on work function measurements on gold-platinum interface using scanning kelvin probe microscopy. In *Journal of Physics: Conference Series*, 371(1) 012030).

Mulwa, W. M. (2012). *Structural and electronic studies of Tio 2, Cr: Tio 2 And Nb: Tio 2 using Density Functional Theory*. Unpublished Doctoral dissertation, Eldoret: Moi University.

Muthee, D. K., & Dejene, B. F. (2021). Effect of annealing temperature on structural, optical, and photocatalytic properties of titanium dioxide nanoparticles. *Heliyon, 7*(6), e07269.

Nath, N. C. D., Lee, H. J., Choi, W. Y., & Lee, J. J. (2013). Electrochemical approach to enhance the open-circuit voltage (Voc) of dye-sensitized solar cells (DSSCs). *Electrochimica Acta*, *109*, 39-45.

Neamen, D. A. (2012). *Semiconductor physics and devices: basic principles*. New York, NY: McGraw-Hill.

Ngei Katumo (2016). *Characterization And Performance Evaluation Of Graphene Films As Counter Electrodes For Dye Sensitized Solar Cells*. Unpublished Thesis, Juja: JKUAT.

Njeru, E. N. (2017). *Characterization Of CdxSe1-xS/PbS thin films deposited by chemical bath deposition for pn junction solar cell application*. Unpublished Doctoral dissertation, Nairobi: Kenyatta University.

Nolan N. T., (2010). *Sol-Gel Synthesis and Characterization of Novel Metal Oxide Nano-materials for Photocatalytic Applications*. Unpublished Ph.D. thesis, Dublin: Dublin Institute of Technology, Ireland.

Nonnenmacher, M., O'boyle, M., & Wickramasinghe, H. K. (1992). Surface investigations with a Kelvin probe force microscope. *Ultramicroscopy*, *42*, 268-273.

Norhafiezah, S., Ayub, R. M., Arshad, M. M., Azman, A. H., Fatin, M. F., Farehanim, M. A., & Hashim, U. (2014, August). The RF power effect on the surface morphology of titanium dioxide (TiO 2) film. In *2014 IEEE International Conference on Semiconductor Electronics (ICSE2014)* (pp. 48-51). IEEE.

Nusbaumer, H., Moser, J. E., Zakeeruddin, S. M., Nazeeruddin, M. K., & Grätzel, M. (2001). CoII (dbbip) 22+ complex rivals tri-iodide/iodide redox mediator in dye-sensitized photovoltaic cells. *The Journal of Physical Chemistry B*, *105*(43), 10461-10464.

Odobel, F., Blart, E., Lagrée, M., Villieras, M., Boujtita, H., El Murr, N., ... & Bignozzi, C. A. (2003). Porphyrin dyes for TiO_2 sensitization. *Journal of Materials Chemistry*, *13*(3), 502-510.

Ogawa, H., Higuchi, T., Nakamura, A., Tokita, S., Miyazaki, D., Hattori, T., & Tsukamoto, T. (2008). Growth of TiO2 thin film by reactive RF magnetron sputtering using oxygen radical. *Journal of Alloys and Compounds*, *449*(1-2), 375-378.

Okada, M., Tazawa, M., Jin, P., Yamada, Y., & Yoshimura, K. (2006). Fabrication of photocatalytic heat-mirror with TiO2/TiN/TiO_2 stacked layers. *Vacuum*, *80*(7), 732-735.

Ouyang, J., Xu, Q., Chu, C. W., Yang, Y., Li, G., & Shinar, J. (2004). On the mechanism of conductivity enhancement in poly (3, 4-ethylenedioxythiophene): poly (styrene sulfonate) film through solvent treatment. *Polymer*, *45*(25), 8443-8450.

Pan, X., Yang, M. Q., Fu, X., Zhang, N., & Xu, Y. J. (2013). Defective TiO 2 with oxygen vacancies: synthesis, properties and photocatalytic applications. *Nanoscale*, *5*(9), 3601-3614.

Park, W. D. (2012). Optical constants and dispersion parameters of CdS thin film prepared by chemical bath deposition. *Transactions on Electrical and Electronic Materials*, *13*(4), 196-199.

Pines, D., & Bohm, D. (1952). A collective description of electron interactions: II. Collective vs individual particle aspects of the interactions. *Physical Review*, *85*(2), 338.

Pingel, P. (2014). *Morphology, charge transport properties, and molecular doping of thiophene-based organic semiconducting thin films*. Unpublished Doctoral dissertation, Potsdam: Universitätsbibliothek der Universität Potsdam.

Polverini, D., Field, M., Dunlop, E., & Zaaiman, W. (2013). Polycrystalline silicon PV modules performance and degradation over 20 years. *Progress in Photovoltaics: Research and Applications*, *21*(5), 1004-1015.

Qi. K., (2008). *Study Photocatalytic Activities of Nano-scaled Metal Oxides on Textiles*, Ph.D. thesis, Hong Kong: The Hong Kong Polytechnic Universit.

Quaschning, V. (2003). The sun as an energy resource. *Renewable Energy World*, *6*(5), 90-93.

Ramanujam, J., & Singh, U. P. (2017). Copper indium gallium selenide based solar cells–a review. *Energy & Environmental Science*, *10*(6), 1306-1319.

Ravindra, N. M., Ganapathy, P., & Choi, J. (2007). Energy gap–refractive index relations in semiconductors–An overview. *Infrared physics & technology*, *50*(1), 21-29.

Réti, B., Kiss, G. I., Gyulavári, T., Baan, K., Magyari, K., & Hernadi, K. (2017). Carbon sphere templates for TiO2 hollow structures: Preparation, characterization and photocatalytic activity. *Catalysis Today*, *284*, 160-168.

Ribeiro, C., Barrado, C. M., de Camargo, E. R., Longo, E., & Leite, E. R. (2009). Phase transformation in titania nanocrystals by the oriented attachment mechanism: the role of the pH value. *Chemistry–A European Journal*, *15*(9), 2217-2222.

Ribeiro, C., Vila, C., Stroppa, D. B., Mastelaro, V. R., Bettini, J., Longo, E., & Leite, E. R. (2007). Anisotropic growth of oxide nanocrystals: insights into the rutile TiO2 phase. *The Journal of Physical Chemistry C*, *111*(16), 5871-5875.

Roberts, M. W., Thomas, J. M., & Bickley, R. I. (1978). Photo-induced reactivity at oxide surfaces. In *Chemical Physics of Solids and Their Surfaces* (pp. 118-156).

Rothschild, A., Levakov, A., Shapira, Y., Ashkenasy, N., & Komem, Y. (2003). Surface photovoltage spectroscopy study of reduced and oxidized nanocrystalline TiO2 films. *Surface science*, *532*, 456-460.

Saini, K. K., Sharma, S. D., Kar, M., Singh, D., & Sharma, C. P. (2007). Structural and optical properties of TiO2 thin films derived by sol–gel dip coating process. *Journal of non-crystalline solids*, *353*(24-25), 2469-2473.

Salem, A. M., & Selim, M. S. (2001). Structure and optical properties of chemically deposited Sb2S3 thin films. *Journal of Physics D: Applied Physics*, *34*(1), 12.

Sangeeth, C. S., Jaiswal, M., & Menon, R. (2009). Correlation of morphology and charge transport in poly (3, 4-ethylenedioxythiophene)–polystyrenesulfonic acid (PEDOT–PSS) films. *Journal of Physics: Condensed Matter*, ***21***(7), 072101.

Sayama, K., Sugihara, H., & Arakawa, H. (1998). Photoelectrochemical properties of a porous Nb2O5 electrode sensitized by a ruthenium dye. *Chemistry of Materials*, *10*(12), 3825-3832.

Schlichthörl, G., Huang, S. Y., Sprague, J., & Frank, A. J. (1997). Band edge movement and recombination kinetics in dye-sensitized nanocrystalline TiO2 solar cells: a study by intensity modulated photovoltage spectroscopy. *The Journal of Physical Chemistry B*, *101*(41), 8141-8155.

Sebastian, M. T. (2010). *Dielectric materials for wireless communication*. Elsevier.

Sedghi A. and Miankushki H. N. (2015). The effect of drying and thickness of TiO_2 electrodes on the photovoltaic performance of dye-sensitized solar cells. *International journal of Electrochemical Science,* **10:** 3354-3362.

Sharma, P., & Katyal, S. C. (2007). Determination of optical parameters of a-(As2Se3) 90Ge10 thin film. *Journal of Physics D: Applied Physics*, *40*(7), 2115.

Shei, S. C. (2013). Optical and Structural Properties of Titanium Dioxide Films from and Starting Materials Annealed at Various Temperatures. *Advances in Materials Science and Engineering*, *2013*.

Shi, Y., Zhu, C., Wang, L., Li, W., Fung, K. K., & Wang, N. (2013). Asymmetric ZnO Panel-Like Hierarchical Architectures with Highly Interconnected Pathways for Free-Electron Transport and Photovoltaic Improvements. *Chemistry–A European Journal*, *19*(1), 282-287.

Shin, H., Lee, B., Kim, C., Park, H., Min, D. K., Jung, J., ... & Kim, S. (2005). Measurement and visualization of doping profile in silicon using Kelvin probe force microscopy (KPFM). *Electronic Materials Letters*, *1*(2), 127-133.

Shinen, M. H., AlSaati, S. A. A., & Razooqi, F. Z. (2018, May). Preparation of high transmittance TiO2 thin films by sol-gel technique as antireflection coating. In *Journal of Physics: Conference Series* (Vol. 1032, No. 1, p. 012018). IOP Publishing.

Sigma Aldrich (2013). *Indium Tin Oxide (ITO) Coated Substrates*. Retrieved from: http://www.sigmaaldrich.com/materials---science/material---science products. html.

da Silva, C. S. C. G. (2008). *Synthesis, spectroscopy and characterization of titanium dioxide based photocatalysts for the degradative oxidation of organic pollutants* (Doctoral dissertation, Universidade do Porto (Portugal)).

Singh, E., & Nalwa, H. S. (2015). Stability of graphene-based heterojunction solar cells. *RSC Advances*, ***5***(90), 73575-73600

Sinton, R. A., & Cuevas, A. (1996). Contactless determination of current–voltage characteristics and minority-carrier lifetimes in semiconductors from quasi-steady-state photoconductance data. *Applied Physics Letters*, *69*(17), 2510-2512.

Smoluchowski, R. (1941). Anisotropy of the electronic work function of metals. *Physical Review*, *60*(9), 661.

Solanki, C. S. (2015). *Solar photovoltaics: fundamentals, technologies and applications*. Delhi: PHI Learning Pvt. Ltd.

Sönmezoğlu, S., Çankaya, G., & Serin, N. (2012). Influence of annealing temperature on structural, morphological and optical properties of nanostructured TiO_2 thin films. *Materials Technology*, *27*(3), 251-256.

Sorantin, P. I., & Schwarz, K. (1992). Chemical bonding in rutile-type compounds. *Inorganic Chemistry*, *31*(4), 567-576.

Sung, Y. M., & Kim, H. J. (2007). Sputter deposition and surface treatment of TiO_2 films for dye-sensitized solar cells using reactive RF plasma. *Thin Solid Films*, *515*(12), 4996-4999.

Sunkara, B. K., & Misra, R. D. K. (2008). Enhanced antibactericidal function of W4+-doped titania-coated nickel ferrite composite nanoparticles: a biomaterial system. *Acta Biomaterialia*, *4*(2), 273-283.

Swanepoel, R. (1983). Determination of the thickness and optical constants of amorphous silicon. *Journal of Physics E: Scientific Instruments*, *16*(12), 1214.

Szczepankiewicz, S. H., Colussi, A. J., & Hoffmann, M. R. (2000). Infrared spectra of photoinduced species on hydroxylated titania surfaces. *The Journal of Physical Chemistry B*, *104*(42), 9842-9850.

Testino, A., Bellobono, I. R., Buscaglia, V., Canevali, C., D'Arienzo, M., Polizzi, S., ... & Morazzoni, F. (2007). Optimizing the photocatalytic properties of hydrothermal TiO2 by the control of phase composition and particle morphology. A systematic approach. *Journal of the American Chemical Society*, *129*(12), 3564-3575.

Tian, G., Dong, L., Wei, C., Huang, J., He, H., & Shao, J. (2006). Investigation on microstructure and optical properties of titanium dioxide coatings annealed at various temperature. *Optical Materials*, *28*(8-9), 1058-1063.

Tian, G., Dong, L., Wei, C., Huang, J., He, H., & Shao, J. (2006). Investigation on microstructure and optical properties of titanium dioxide coatings annealed at various temperature. *Optical Materials*, *28*(8-9), 1058-1063.

Trasatti, S., & Doubova, L. M. (1995). Crystal-face specificity of electrical double-layer parameters at metal/solution interfaces. *Journal of the Chemical Society, Faraday Transactions*, *91*(19), 3311-3325.

Tu, W., Zhou, Y., Liu, Q., Yan, S., Bao, S., Wang, X., ... & Zou, Z. (2013). An in situ simultaneous reduction-hydrolysis technique for fabrication of TiO2-graphene 2D sandwich-like hybrid nanosheets: graphene-promoted selectivity of photocatalytic-driven hydrogenation and coupling of CO_2 into methane and ethane. *Advanced functional materials*, *23*(14), 1743-1749.

Ullah, Z., Atiq, S., & Naseem, S. (2013). Indexing the diffraction patterns and investigating the crystal structure of Pb-doped strontium ferrites. *Journal of Scientific Research*, *5*(2), 235-244.

Vallejo, W., Quinones, C., & Hernandez, J. A. (2011). *The chemistry and physics of dye-sensitized solar cells*. Colombia: Universidad Nacional de Colombia.

Voss, B., Knobloch, T., & Goetzberger, A. (1998). *Crystalline silicon solar cells*. Chichester: John Wiley & Sons Ltd.

Wan, X., Long, G., Huang, L., & Chen, Y. (2011). Graphene – a promising material for organic photovoltaic cells. *Advanced Materials*, **23**(45), 5342-5358.

Wang, D. H., Goh, W. C., Ning, M., & Ong, C. K. (2006). Effect of Ba doping on magnetic, ferroelectric, and magnetoelectric properties in mutiferroic Bi FeO_3 at room temperature. *Applied physics letters*, *88*(21), 212907.

Wang, J. T. W., Ball, J. M., Barea, E. M., Abate, A., Alexander-Webber, J. A., Huang, J., ... & Nicholas, R. J. (2014). Low-temperature processed electron collection layers of graphene/TiO_2 nanocomposites in thin film perovskite solar cells. *Nano letters*, *14*(2), 724-730.

Wang, X., Xu, Q., Li, M., Shen, S., Wang, X., Wang, Y., ... & Li, C. (2012). Photocatalytic overall water splitting promoted by an α–β phase junction on Ga2O3. *Angewandte Chemie*, *124*(52), 13266-13269.

Wang, Y., Wu, D., Fu, L. M., Ai, X. C., Xu, D., & Zhang, J. P. (2015). Correlation between Energy and Spatial Distribution of Intragap Trap States in the TiO2 Photoanode of Dye-Sensitized Solar Cells. *ChemPhysChem*, *16*(10), 2253-2259.

Wasfi, M. (2011). Solar Energy and Photovoltaic Systems. *Cyber Journals, Journal of Selected Areas in Renewable and Sustainable Energy (JRSE), 1(2),* 1-8.

Watson, S., Beydoun, D., Scott, J., & Amal, R. (2004). Preparation of nanosized crystalline TiO_2 particles at low temperature for photocatalysis. *Journal of Nanoparticle Research*, *6*(2), 193-207.

Wei, D. (2010). Dye sensitized solar cells. *International journal of molecular sciences*, *11*(3), 1103-1113.

Wibowo, K. M., Sahdan, M. Z., Asmah, M. T., Saim, H., Adriyanto, F., & Hadi, S. (2017, August). Influence of Annealing Temperature on Surface Morphological and Electrical Properties of Aluminum Thin Film on Glass Substrate by Vacuum Thermal Evaporator. In *IOP Conference Series: Materials Science and Engineering* (Vol. 226, No. 1, p. 012180). IOP Publishing.

Wolfe, P. (2013). *Solar photovoltaic projects in the mainstream power market*. London: Routledge.

Wu, C., Yue, Y., Deng, X., Hua, W., & Gao, Z. (2004). Investigation on the synergetic effect between anatase and rutile nanoparticles in gas-phase photocatalytic oxidations. *Catalysis Today*, *93*, 863-869.

Würfel, U., Peters, M., & Hinsch, A. (2008). Detailed experimental and theoretical investigation of the electron transport in a dye solar cell by means of a three-electrode configuration. *The Journal of Physical Chemistry C*, *112*(5), 1711-1720.

Wypych, A., Bobowska, I., Tracz, M., Opasinska, A., Kadlubowski, S., Krzywania-Kaliszewska, A., ... & Wojciechowski, P. (2014). Dielectric properties and characterisation of titanium dioxide obtained by different chemistry methods. *Journal of Nanomaterials*, *2014(9)*, 1-9.

Yan L., Y., Li, Z., Green, M., Just, M., Li, Y. Y., & Chen, X. (2017). Titanium dioxide nanomaterials for photocatalysis. *Journal of Physics D: Applied Physics*, *50*(19), 193003.

Yan, W., Huo, M. M., Hu, R., & Wang, Y. (2019). Working area effects on the energetic distribution of trap states and charge dynamics of dye-sensitized solar cells. *RSC advances*, *9*(3), 1734-1740.

Yan, X., & Chen, X. (2015). Titanium dioxide nanomaterials. *Encyclopedia of inorganic and bioinorganic chemistry*, 1-38.

Yang, R. Y., Chen, H. Y., & Lai, F. D. (2012). Performance degradation of dye-sensitized solar cells induced by electrolytes. *Advances in Materials Science and Engineering*, *2012(20)*, 215-257.

Yang, W., & Wolden, C. A. (2006). Plasma-enhanced chemical vapor deposition of TiO_2 thin films for dielectric applications. *Thin Solid Films*, *515*(4), 1708-1713.

Yao, T., Sui, Z., & Janaswamy, S. (2018). *Annealing. In Physical modifications of starch*. Gateway East Singapore: Springer.

Yarmand, B., & Sadrnezhaad, S. K. (2010). Influence of annealing temperature on structural and optical properties of mesoporous TiO_2 thin films prepared by sol-gel templating technique. *Journal of Optoelectronics and Advanced Materials*, *12*(7), 1490.

Ye, M., Wen, X., Wang, M., Iocozzia, J., Zhang, N., Lin, C., & Lin, Z. (2015). Recent advances in dye-sensitized solar cells: from photoanodes, sensitizers and electrolytes to counter electrodes. *Materials Today*, *18*(3), 155-162.

Ye, M., Zheng, D., Lv, M., Chen, C., Lin, C., & Lin, Z. (2013). Hierarchically structured nanotubes for highly efficient dye-sensitized solar cells. *Advanced Materials*, *25*(22), 3039-3044.

Ye, Q., Liu, P. Y., Tang, Z. F., & Zhai, L. (2007). Hydrophilic properties of nano-TiO2 thin films deposited by RF magnetron sputtering. *Vacuum*, *81*(5), 627-631.

Ying Y. W., Ren, X. G., Zhen, H. N., Hui, H., Shu, G., Huan, P. Y., Chun, X. C. & Ting, Y. (2012). Thickness identification of two-dimensional materials by optical imaging. *Nanotechnology*, *23 (49),* 495713.

Yoon, J. H., Song, J., & Lee, S. J. (2011). Practical application of building integrated photovoltaic (BIPV) system using transparent amorphous silicon thin-film PV module. *Solar Energy*, *85*(5), 723-733.

Yu, H., Roh, J., Yun, J., & Jang, J. (2016). Synergistic effects of three-dimensional orchid-like TiO_2 nanowire networks and plasmonic nanoparticles for highly efficient mesoscopic perovskite solar cells. *Journal of Materials Chemistry A*, *4*(19), 7322-7329.

Zakeeruddin, S. M., Nazeeruddin, M. K., Humphry-Baker, R., Grätzel, M., & Shklover, V. (1998). Stepwise assembly of tris-heteroleptic polypyridyl complexes of ruthenium (II). *Inorganic Chemistry*, *37*(20), 5251-5259.

Zerweck, U., Loppacher, C., Otto, T., Grafström, S., & Eng, L. M. (2005). Accuracy and resolution limits of Kelvin probe force microscopy. *Physical Review B*, *71*(12), 125424.

Zhang, F., Inganäs, O., Zhou, Y., & Vandewal, K. (2016). Development of polymer–fullerene solar cells. *National Science Review*, *3*(2), 222-239.

Zhao, B., Zhou, J., Chen, Y., & Peng, Y. (2011). Effect of annealing temperature on the structure and optical properties of sputtered TiO2 films. *Journal of Alloys and Compounds*, *509(9),* 4060-4064.

Zhou, Y., Zhang, L., & Tao, S. (2018). Porous TiO_2 with large surface area is an efficient catalyst carrier for the recovery of wastewater containing an ultrahigh concentration of dye. *RSC advances*, *8*(7), 3433-3442.

APPENDICES

Appendix I: A photograph of main chemical components used in the fabrication of DSSCs. (a) From left: Titanium Nanoxide, N719 ruthenium dye, electrolyte and Platisol T/SP (b) from left: Acetone and Ethanol.

Appendix II: A photograph of Benjamin Mbaluka coating the WEs using Doctor-blading process

Appendix III: A photograph of: (a) WEs being placed in the KL 420 muffle furnace (b) DSSM fabricated from six DSSCs connected in Series